

2013-07-16

Cascade Effects on Circular Arc Airfoils for Windmill Analysis

Fagbenro, Kabir Ayodeji

Fagbenro, K. A. (2013). Cascade Effects on Circular Arc Airfoils for Windmill Analysis (Master's thesis, University of Calgary, Calgary, Canada). Retrieved from <https://prism.ucalgary.ca>. doi:10.11575/PRISM/25220
<http://hdl.handle.net/11023/831>

Downloaded from PRISM Repository, University of Calgary

UNIVERSITY OF CALGARY

Cascade Effects on Circular Arc Airfoils for Windmill Analysis

by

Kabir Ayodeji Fagbenro

A THESIS

SUBMITTED TO THE FACULTY OF GRADUATE STUDIES
IN PARTIAL FULFILMENT OF THE REQUIREMENTS FOR THE
DEGREE OF MASTER OF SCIENCE

DEPARTMENT OF MECHANICAL & MANUFACTURING ENGINEERING

CALGARY, ALBERTA

JULY, 2013

© Kabir Ayodeji Fagbenro 2013

Abstract

Water-pumping is one of the oldest uses of wind energy with the multi-bladed, high-solidity windmill still in widespread use. For the present, solidity can be taken as the projected area of the blades as a fraction of the circular swept area of the rotor. Windmills rotate slowly and have very high solidity, making their aerodynamic analysis fundamentally different to that for modern wind turbines. The main difference addressed in this thesis is solidity effects on blade lift and drag in the expectation that windmills can be analysed by a modification of standard blade element theory which assumes that the blades behave as airfoils. Circular arc airfoils were computationally modelled by using the well-known shear stress transport - transition (SST-transition) model in FLUENT to study the solidity effect on lift and drag at Reynolds number of 100,000. The transition model constants were adjusted in order to match measured pressure distributions on isolated circular arc airfoils. The cascade calculations show that the ratio of the lift and drag ratio which measures the performance of the windmill changes significantly with increasing solidity which implies that it should not be neglected in evaluation of windmill performance.

Acknowledgements

I would like to express my sincere gratitude to my supervisor Dr. David Wood for given me the opportunity and guiding me through the completion of the work. I appreciate his patience and support. My sincere appreciation also goes to Mohamed Arif bin Mohammed for his support and help in facilitating a lot of difficulties that was faced in the course of completing the project. I am also indebted to Dr. Robert Martinuzzi, for immeasurable advice, and Dr. David Rival. To my colleagues in the Fluids group I say thank you for showing your love (Mohammed Hamman, John Fernando, Arman Hemmati and others). To my wife Mariam, and my kids Sa'ad, Saaqib, Sobuurah and Saleh. I thank you so much for your understanding. To my dad Salau. I say a big thank you for your encouragement. This research was financially supported by Natural Sciences and Engineering Research of Canada (NSERC) and the ENMAX Corporation under the Industrial Research Chairs program.

Dedication

This work is dedicated to Almighty Allah for His Infinite Mercies and to the memory of my beloved mother Mercy Olufunlola Fagbenro.

Table of Contents

Abstract.....	iii
Acknowledgement.....	iv
Dedication.....	v
Table of Contents.....	vi
List of Tables.....	ix
List of Figures.....	x
List of Symbols, Abbreviations and Nomenclature.....	xvii
Chapter 1: Introduction.....	1
1.1 Overview.....	2
1.2 Water Pumping Systems.....	3
1.3. Windmill and Rotor Solidity.....	5
1.4 Tip Speed Ratio.....	9
1.5 Windmill Blade.....	9
1.5.1 Blade Geometry: Circular Arc Airfoil (CA).....	11
1.5.2 Blade Solidity.....	11
1.6 Numerical Model for the Flow.....	12
Chapter 2: Literature Review.....	14
2.1 Windmill Background.....	14
2.2 Experiments on Windmill Blades.....	15
2.3 Cascade Effects.....	23
2.4 Summary of the Previous Literature.....	34
Chapter 3: Transition, Turbulence and Numerical Modelling.....	36
3.1 Turbulence Modeling.....	36
3.1.1 Modeling the Reynolds Shear Stress.....	37
3.2 The Boundary Layer Calculations.....	39
3.2.1 Turbulence Calculation.....	41
3.2.2 Transition Model.....	42
3.2.3 Laminar Boundary Layer Calculation.....	45

3.2.4 Laminar and Transitional Boundary Layers	45
3.2 Coupling the Transition Model and SST Transport Equations	46
Chapter 4: The Calculation of Circular Arc Airfoil Performance.....	47
4.1 Introduction.....	47
4.1.1 Calculating C_L and C_D	47
4.2 Calculation Procedure	49
4.2.1 Circular Arc Airfoil CA1.....	49
4.2.2 Circular Arc Airfoil CA2.....	60
Chapter 5: Aerodynamics of Circular Arc Cascades for Windmill Applications....	66
5.1 Introduction.....	66
5.2 Cascade Theory.....	66
5.3 Calculation Procedure.....	71
5.3.1 Computational Mesh and Boundary Conditions	71
5.3.1.1 Single Blade Domain	72
5.3.1.2 Two-Blade Domain.....	73
5.3.1.3 Domain and Mesh Independence Studies	74
5.3.2 Solidity $1.5 \geq \sigma \geq 0.75$	75
5.3.3 Solidity $\sigma < 0.75$	76
5.3.4 Calculation of F_x and F_y	77
5.3.5 Single and Double Domain Results.....	80
5.4 Lift and drag Coefficients of Blades in the Cascade	83
5.5 Comparing Velocity and Turbulent Kinetic Energy Distribution at Nominal $\alpha=6^\circ$	86
Chapter 6: Conclusion & Recommendations.....	91
6.1 Conclusion.....	91
6.2 Recommendation.....	94
References.....	95
Appendix A.....	102
A.0 Review of Numerical Methods.....	102
A.1 Introduction.....	102

A.2 The Conservation of Mass and Navier-Stokes Equations.....	102
A.3 Computational Fluid Dynamics	103
A.3.1 Discretization Errors.....	103
A.3.2 Finite Volume Method.....	103
A.3.3 Upwind Differencing Scheme	105
A.3.4 Gradient Calculation in ANSYS FLUENT	106
A.3.5 Properties of Discretization Schemes	108
A.3.5.1 Conservativeness.....	108
A.3.5.2 Boundedness	109
A.3.5.3 Transportiveness.....	110

List of Tables

Table 1.1: Comparison of the Advantages and Disadvantages of Windmill and Photovoltaic Water Pumping systems adapted from Mecke et al. 2007	4
Table 4.1: Comparing the default and changed values for $\sigma_{\theta t}$ and $c_{\theta t}$	52
Table 4.2: Table 4.2 Comparing L and D directly from FLUENT and post-processed using Matlab for of CA1 of Tezuka et al. (2008).....	54
Table 4.3: Computed C_L and C_D at $\alpha = 2^\circ, 3^\circ, 7^\circ$ and 10° of CA1 of Tezuka et al. (2008).....	54
Table 5.1: Notation and properties of the computational domain.....	78
Table 5.2: Comparing F_y and F_x for domains A, B and C in (Pa) at $\alpha=4^\circ, \sigma = 1.5$	78
Table 5.3: Comparing F_y (Pa) for cases A and B using Matlab and calculated by the three methods explained in the text, for $\alpha = 4^\circ, \sigma = 1.5$ and $U_\infty = 11.39$ m/s.....	79
Table 5.4: Comparing the F_x (Pa) for A and B using Matlab and calculated in FLUENT, at $\alpha = 4^\circ, \sigma = 1.5$ and $U_\infty = 11.39$ m/s.....	79
Table 5.5: Comparing σ with α_m , C_L and C_D at nominal $\alpha = 6^\circ$	86

List of Figures

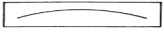
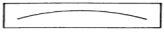
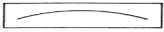
Figure 1.1: Windmill at Eau Claire Market Mall Downtown Calgary, Alberta.....	7
Figure 1.2: Wind turbines generating electricity at Horse Hollow Wind Farm Nolan, West Texas, and the world's largest wind power project. (Solidity 0.1 - 0.2). Photograph: Alamy. http://www.guardian.co.uk/environment/2012/apr/29/wind-farms-night-temperatures-study , accessed in March 013.....	8
Figure 1.3: Windmill blade with spar.....	10
Figure 1.4: Circular arc airfoil.....	11
Figure 1.5: Two components of cascade	12
Figure 2.1: Arrangement of windmill blade under construction (from http://waterfromyk.wordpress.com/) accessed in March 2013.....	15
Figure 2.2: Section characteristics of circular arc airfoils at $Re = 60,000$  Bruining (1979).....	16
Figure 2.3: Section characteristics of circular arc airfoils at $Re = 100,000$  Bruining (1979).....	17
Figure 2.4: Section characteristics of circular arc airfoils at $Re = 200,000$  Bruining (1979).....	17
Figure 2.5(a-c): Surface pressure measurements on 4% circular arc airfoil at low Re Tezuka et al. (2008). Data provided by Prof. K. Inoue.....	19-20



Figure 2.6(a-b): Effects of camber on the aerodynamic characteristics of rectangular model wing from aluminium foil, with a thickness of 0.3 mm and a chord length of 30mm. Each symbol refers to different camber as shown in the panel on the right hand side of the figure (a) C_L and C_D vs α (b) Polar curve. From Okamoto et al. (1996) with permission.....	20-21
Figure 2.7: Effects of thickness on the aerodynamic characteristics of a curved - section model wing (camber 9%). Each symbol refer to a different airfoil shape as shown in the panel on the right hand side; c , chord length; t , thickness; Re , all dimensions are given in millimeters (a) C_L and C_D vs α (b) polar curve. From Okamoto et al. (1996) with permission.....	22
Figure 2.8: Weinig's results for lift ratio of cascade of thin flat plates, showing dependence on stagger angle and solidity (from Dixon 2005).....	25
Figure 2.9: Turbulent intensity contours (top) and computed C_f -distribution against experimental data for the Zierke et al. (1989).....	27
Figure 2.10: Pressure coefficient results for the Zierke et al. (1989) compressor cascade..	28
Figure 2.11: Variation of pressure coefficient at solidity of 1.2  Eftekhari et al. (2012).....	29
Figure 2.12: Variation of pressure coefficient at solidity of 0.8  Eftekhari et al. (2012).....	29

Figure 2.13: Static pressure distribution on the blades with $\sigma = 1.5$ Köktürk (2005)



30

Figure 2.14: Static pressure distribution on the blades with $\sigma = 0.1$ Köktürk (2005)



31

Figure 2.15: C_L vs. α at different σ , at velocities of 70m/s Köktürk, (2005)



31

Figure 2.16: C_D coefficient vs. α at different σ solidities Köktürk, (2005)



32

Figure 2.17: C_L and C_D against α_m for isolated CA and the cascade from Ikui et al. (1972).

34

Figure 2.18: Maximum C_L / C_D and α_m , data was read from Figure 2.17

34

Figure 4.1: Pressure and viscous forces acting on CA and the resultant and lift forces...

48

Figure 4.2: A view of part of the computational mesh for the circular arc airfoil

50

Figure 4.3: Mesh-independence test

51

Figure 4.4: Streamlines and Turbulence Kinetic Energy (k) (m^2/s^2) contours of the current simulation for CA1, for $\alpha = 7^\circ$, $U_\infty = 9.06\text{m/s}$, Tezuka et al. (2008).

53

Figure 4.5a: Computed and measured pressures distribution of a 4% cambered CA1 airfoil Tezuka et al. (2008) at $\alpha = 2^\circ$

55

Figure 4.5b: Computed and measured pressures distribution of a 4% cambered CA1 airfoil Tezuka et al. (2008) at $\alpha = 3^\circ$	56
Figure 4.5c: Computed and measured pressures distribution of a 4% cambered CA1 airfoil Tezuka et al. (2008) at $\alpha = 7^\circ$	56
Figure 4.5d: Computed and measured pressures distribution of a 4% cambered CA1 airfoil Tezuka et al. (2008) at $\alpha = 10^\circ$	57
Figure 4.6a: Computed streamline for 4% cambered CA airfoil, $\alpha = 3^\circ$, Tezuka et al. (2008).....	58
Figure 4.6b: Computed wall shear stress for a 4% cambered CA1 airfoil, $\alpha = 3^\circ$, Tezuka et al. (2008).....	58
Figure 4.7a: Computed streamline for a 4% cambered CA1 airfoil, $\alpha = 7^\circ$, Tezuka et al. (2008).....	59
Figure 4.7b: Wall shear stress for a 4% cambered CA1 airfoil, $\alpha = 7^\circ$, Tezuka et al. (2008).....	59
Figure 4.7c: Wall shear stress for a 4% cambered CA1 airfoil, $\alpha = 10^\circ$ Tezuka et al. (2008).....	60
Figure 4.8: CA2 airfoil, dimensions in mm adapted from Bruining (1979).....	61
Figure 4.9: Part of unstructured mesh generated in ICEM for Bruining (1979) model...	61
Figure 4.10: Mesh independence test for CA2 of Bruining (1979).....	62
Figure 4.11: Computed and measured C_L for the experiment of Bruining (1979).....	63
Figure 4.12: Computed and measured C_D for the experiment of Bruining (1979).....	64

Figure 4.13: Computed pressure, $\alpha = 0^\circ$ for the 10% CA airfoil of Bruining (1979).....	64
Figure 4.14: Computed velocity magnitude contours at $\alpha = 0^\circ$, $U_\infty = 9.738$ m/s for the experiment of Bruining (1979).....	65
Figure 5.1: Control volume for a cascade of equi- spaced identical bodies.....	68
Figure 5.2: Velocity and force diagram of cascade.....	70
Figure 5.3: Boundary conditions for solidity calculation.....	73
Figure 5.4: Boundary conditions for solidity calculation of double blade.....	74
Figure 5.5: Boundary conditions and computational domain for $\sigma < 0.75$	77
Figure 5.6: Computed velocity magnitude contours in m/s for double blade CA2 of case C at $\alpha = 4^\circ$, $\sigma = 1.5$ and $U_\infty = 11.39$ m/s. Only part of the computational domain is shown.	80
Figure 5.7: Computed velocity magnitude contours in m/s for single blade CA2 of case A at $\alpha = 4^\circ$, $\sigma = 1.5$ and $U_\infty = 11.39$ m/s with periodic repeat. Only part of the computational domain is shown.....	81
Figure 5.8: Computed C_P for case A and C at $\alpha = 4^\circ$ and $U_\infty = 11.39$ m/s.....	81
Figure 5.9a: Computed C_P for case A at $\alpha = 4^\circ$ and $U_\infty = 11.39$ m/s.....	82
Figure 5.9a: Computed C_P for case C at $\alpha = 4^\circ$ and $U_\infty = 11.39$ m/s.....	82
Figure 5.10: Computed C_L against α and α_m for CA2	83
Figure 5.11: Computed C_D against α and α_m for CA2.....	84
Figure 5.12: Computed C_L/C_D against α and α_m for CA2.....	85
Figure 5.13: Contours of Turbulent kinetic Energy (k) (m^2/s^2), $\sigma = 1.5$, part of the computational domain.....	87

Figure 5.14: Contours of velocity magnitude (m/s), $\sigma = 1.5$, part of the computational domain.....	88
Figure 5.15: Contours of Turbulent Kinetic Energy (k) (m^2/s^2), $\sigma = 1.5$, part of the computational domain.....	88
Figure 5.16: Contours of velocity magnitude (m/s), $\sigma = 1.2$, part of the computational domain.....	88
Figure 5.17: Contours of Turbulent Kinetic Energy (k) (m^2/s^2), $\sigma = 1.5$, part of the computational domain.....	88
Figure 5.18: Contours of velocity magnitude (m/s), $\sigma = 0.75$, part of the computational domain.....	89
Figure 5.19: Contours of Turbulent Kinetic Energy (k) (m^2/s^2), $\sigma = 0.75$, part of the computational domain.....	89
Figure 5.20: Contours of velocity magnitude (m/s), $\sigma = 0.5$, part of the computational domain.....	89
Figure 5.21: Contours of Turbulent Kinetic Energy (k) (m^2/s^2), $\sigma = 0.5$, part of the computational domain.....	89
Figure 5.22: Contours of velocity magnitude (m/s), $\sigma = 0.1$, part of the computational domain.....	90
Figure 5.23: Contours of Turbulent Kinetic Energy (k) (m^2/s^2), $\sigma = 0.1$, part of the computational domain.....	90
Figure 5.24: Velocity magnitude (m/s), legend for Figures 5.14, 5.16, 5.18, 5.20 & 5.22.....	90

Figure 5.25: Turbulent Kinetic Energy (k) (m^2/s^2), legend for Figures 5.15, 5.17, 5.19, 5.21 & 5.23.....	90
Figure A.1: A control around node P , adapted from Versteeg and Malalasekera (2007).....	104
Figure A.2: Evaluation of gradient at the cell centroid. Adapted from ANSYS (2011)...	107
Figure A.3: Discretization of diffusive fluxes Versteeg and Malalasekera (2007).....	109
Figure A.4: Distribution of a property in a vicinity of a source at different Peclet numbers from Versteeg and Malalasekera (2007).....	111

List of Symbols, Abbreviations and Nomenclature

Symbols	Definition	Units	First Appearance
A'	Force tangential to the direction of the chord	(Pa)	Eq. (4.1)
a_{nb}	Coefficient of neighbouring nodes except the diagonal elements	(--)	Eq. (A.14)
a'_p	Net coefficient of central node P	(--)	Eq. (A.14)
c	Chord	(m)	--
$c_{a1}, c_{a2},$ $c_{e1}, c_{e2}, c_{e3}, \sigma_f$	Constants in intermittency equation	(--)	Eq. (3.26)
C_D	Coefficient of Drag	(--)	--
C_f	Skin friction	(--)	--
C_{ijk}	Turbulence transport tensor	(m/s ³)	Eq. (3.8)
C_L	Coefficient of lift	(--)	--
C_p	Power coefficient	(--)	--
C_P	Coefficient of pressure	(--)	--
$c_{\theta t}$	Model constant for Reynolds number momentum thickness	(--)	Eq. (3.33)
D	Drag	(N/m)	--

\bar{D}	Diffusion conductance at cell faces	(Kg/m ²)	Eq. (7.7)
D_m	Mean drag	(Pa)	Eq. (5.7)
E, Q, W	Nodes	(--)	--
E_γ	Destruction term for intermittency	(--)	Eq. (3.20)
F	Convective mass flux per unit area at cell faces	(Kg/m ²)	Eq. (A.7)
F_{length}	Empirical correlation that controls the length of transition region	(--)	Eq. (3.14)
F_{onset}	Determines when the production of intermittency is activated	(--)	Eq. (3.21)
$F_x, F_y,$	x and y direction forces	(N/m)	Eq. (5.3), Eq. (5.1)
F_{wake}	Ensures that the blending function are not active in the wake regions	(--)	Eq. (3.32)
$F_{\theta t}$	Blending function	(--)	Eq. (3.28)
G_k	Generation of k	(--)	Eq. (3.15),
G_ω	Generation of ω	(--)	Eq. (3.16)
h	Camber	(mm)	--
$[J]$	Jacobian matrix	(--)	Eq. (A.12)
k	Turbulence kinetic energy	(m ² /s ²)	--
k_i	Interference factor	(--)	Eq. (2.1)

L	Lift	(N/m)	--
L_m	Mean lift	(N/m)	Eq. (5.7)
n	Number of blades	(--)	--
N'	Force normal to the direction of the chord	(N/m)	Eq. (4.1)
P	Pressure	(Pa)	Eq. (3.3)
Pe	Peclet number	(--)	Eq. (A.15)
P_γ	Transition source term	(Kg/m ³ s)	Eq. (3.15)
$P_{\theta t}$	Source term for $\widehat{Re}_{\theta t}$	(Kg/m ³ s)	Eq. (3.28)
P_0	Reference pressure	(Pa)	Eq. (4.5)
R	Rotor radius	(m)	Eq. (1.1)
R'	Resultant force in the direction of φ	(N/m)	--
Re	Reynolds number	(--)	--
Re_θ	Reynolds number momentum thickness	(--)	Eq. (3.13)
$Re_{\theta c}$	Reynolds number momentum thickness critical value	(--)	Eq. (3.22)
$Re_{\theta t}$	Local momentum thickness Reynolds number	(--)	--
$\widehat{Re}_{\theta t}$	Local transition onset momentum thickness Reynolds number	(--)	--
Re_v	Strain rate (vorticity) Reynolds number	(--)	Eq. (3.12)

r_i	Displacement vector	(m)	--
s	Spacing	(m)	(--)
S	Strain rate	(s ⁻¹)	Eq. (3. 12)
S_{ij}	Mean Strain-rate tensor	(s ⁻¹)	Eq. (3.3)
S_k and S_ω	User defined source term due to k and ω	(Kg/m-s ³) (Kg/m3-s ²)	Eq. (3.15), Eq. (3.16)
t	Time	(s)	Eq. (3.1)
t_{ij}	Stress tensor	N/m ²	Eq. (3.4)
Tu	Turbulence intensity	(%)	--
U_j, U_m	Mean velocity	(m/s)	Eq. (3.1)
U_∞	Freestream velocity	(m/s)	--
u_j	Velocity vector	(m/s)	Eq. (3.1)
$\bar{U}_j(x)$	Time average of mean velocity	(m/s)	Eq. (3.2)
$u_j(x, t)$	Time average of instantaneous velocity	(m/s)	Eq. (3.1)
$u'_j(x, t)$	Time average fluctuating velocity	(m/s)	Eq. (3.1)
u^+	Non dimensional velocity	(--)	Eq. (3.34)
u_τ	Friction velocity	(m/s)	Eq. (3.34)
u_1, u_3	Average axial velocity at inlet and outlet of control volume	(m/s)	Eq. (5.1)
v_m	Mean vertical velocity at inlet	(m/s)	Eq. (5.4)
v_1, v_3	Vertical velocity at inlet and outlet of	(m/s)	Eq. (5.1)

	control volume		
x_j	Position vector	(--)	Eq. (3.3)
y	Distance from the nearest wall	(m)	Eq. (3.12)
Y_k	Effective diffusivity of k due to turbulence	(m ² /s)	Eq. (3.15)
Y_k^*, Y_ω	Effective diffusivity of ω and k due to turbulence	(m ² /s)	Eq. (3.15), Eq. (3.16),
y^+	Non-dimensional normal distance from wall	(--)	--

Greek Symbols	Definition	Units	First appearance
α	Angle of attack	(degree)	--
α_m	Mean angle of attack	(degree)	Eq. (2.1)
α^*	Coefficient that is used to damp the turbulent viscosity in $k - \omega$ model	(--)	Eq. (3.19)
α_∞^*	Constant used to control the effect of Reynolds number in $k - \omega$ model (0-1)	(--)	--
ε	Dissipation rate	(s ⁻¹)	--
ε_{ij}	Dissipation tensor	(m ² /s ³)	Eq. (3.8)
γ	Intermittency	(--)	(--)
Γ	Diffusion constant	(m ² /s)	Eq. (A.3)
Γ_k, Γ_ω	Effective diffusivity of k and ω	(m ² /s)	Eq. (3.16)
δ_{BL}	Boundary layer thickness	(m)	Eq. (3.31)
δ_{ij}	Kronecker delta function, function of two variables (i, j)	(--)	Eq. (3.11)
λ	Tip speed ratio	(--)	Eq. (1.1)
$\lambda_{optimal}$	Optimal tip speed ratio	(--)	--
λ_θ	Thwaites' pressure gradient parameter	(--)	Eq. (3.14)
μ	Dynamic viscosity	(Pa-s)	--
μ_t	Eddy viscosity	(Pa-s)	Eq. (3.10)

ν	Kinematic viscosity	(m ² s ⁻¹)	--
ω	Specific dissipation rate, ε/k	(m ² s ⁻¹)	Eq. (3.16)
Ω	Vorticity magnitude	(s ⁻¹)	Eq.(3.30)
Ω_a	Angular velocity	(Rad/s)	Eq. (1.1)
ϕ	Property ϕ	(--)	Eq. (A.3)
π	Pi	(--)	--
Π_{ij}	Pressure strain-correlation tensor	(m ² /s ³)	Eq. (3.8)
ρ	Density	(Kg/m ³)	--
$\rho \overline{u'_i u'_j}$, τ_{ij}	Reynolds-stress tensor	(N/m ²)	Eq. (3.3), Eq. (3.6)
σ	Local Solidity	(--)	--
σ_k and σ_ω	Turbulent Prandtl numbers for k and ω	(--)	Eq. (3.17)
$\sigma_{\theta t}$	Model constant for Reynolds number momentum thickness	(--)	Eq. (3.33)
Σ	Overall solidity	(--)	--
τ , t	Time	(s)	Eq. (3.1)
τ_{wall}	Wall shear stress	(N/m ²)	Eq. (3.34)
θ	Momentum thickness	(mm)	--
θ_{BL}	Momentum thickness boundary layer	(mm)	Eq. (3.31)
θ_c	Camber angle	(degree)	--
θ_P	Pitch angle	(degree)	Eq. (5.1)

Δ	deviation	(%)	--
$\Delta\phi$	Difference vector	(--)	Eq. (A.12)
Δt	Thickness	(mm)	(mm)
$\nabla\phi_{c0}$	Gradient at $c0$	(m^{-1})	--

Abbreviations

BC	Boundary Condition
BET	Blade Element Theory
CA	Circular arc airfoil
CFD	Computational Fluid Dynamics
CV	Control volume
LE	Leading edge
LSB	Laminar separation bubble
LSCB	Least Squares Cell-Based
NACA	National Advisory Committee for Aeronautics
N-S	Navier-Stokes
PV	Photovoltaic
QUICK	Quadratic Upwind Interpolation for Convective Kinetics

SOU	Second-Order Upwind
SST	Shear Stress Transport
TE	Trailing edge
1-D	1-Dimensional
2-D	2- Dimensional
3-D	3- Dimensional

Chapter 1: Introduction

The challenge posed by environmental degradation via air and water pollution partially resulting from the high energy demand and high cost of the conventional energy has motivated the recent rapid development of alternative energy. Notwithstanding, alternative energy has a long history. It is believed that various forms of windmill have been used for at least 3000 years for pumping water and grinding grains. For sailing ships, wind has been an essential source of power for even longer, Burton et al. (2011). In developing countries, a large percentage of people do not have access to the electricity supplied via the national grid for basic activities like milling of grains, pumping of water and irrigation of farm lands. However, many of these people have access to abundant wind energy resources. The energy supplied by wind has been used for small and large scale electricity generation, offering environmental sustainability, low capital costs, and excellent adaptability to diverse environmental and cultural situations.

The underlying problem with wind power for water pumping, despite its use for thousands of years, is that the basic principles are not well understood and the efficiency of water pumping is poor, Pinilla et al. (1984). A well designed water pumping windmill has an overall efficiency of about 30% in low wind speeds. The limited information on this equipment prevents the full exploitation of its potential. The most challenging part is that there is little information on the lift, L , and drag, D , of blades in terms of the camber, thickness, shape and solidity which measures the proximity of the blades to each other. The blades considered in this report are thin, with less than 10% maximum camber which occurs at 50% of the section. These characteristics

are typical of windmill blade and information is available for the important aerodynamics properties L and D of blades from two separate experiments. Neither of these experiments considered the very important effects of solidity.

1.1 Overview

The focus of this thesis is to investigate the unmeasured solidity effects on blade L and D on circular arc airfoils typical in water pumping windmills using the computational fluid dynamics, (CFD) software FLUENT. In simple terms, the solidity is the parameter that characterizes the closeness of the blades. The initial work was to compare the surface pressure distribution measurement of Tezuka et al. (2008) on a circular arc (CA) airfoil of 4% camber to numerical predictions using the SST-transition model available in ANSYS (2011). In order to match the measured locations of laminar separation and turbulent reattachment, the constants of the turbulence model were adjusted. The adjusted constants were used in the calculation of lift and drag coefficient, (C_L and C_D) of the experiment performed by Bruining, (1979) on a zero solidity CA of 10% camber. Subsequently, the effect of varying the solidity over the range typical of windmill applications was studied for CA airfoils with 10% camber. This work was motivated by the fact that water pumping windmills have high solidity and the detailed blade element theory (BET) studies by Rijs & Smulders (1990), Rijs et al. (1992), and Islam and Islam (1994) ignored the effects of solidity.

1.2 Water Pumping Systems

The use of water in our daily lives cannot be overemphasized. According to the United Nations, water scarcity already affects every continent UN (2013): “Around 1.2 billion people, or almost one-fifth of the world's population, live in areas of physical scarcity of water. Another 1.6 billion people, or almost one quarter of the world's population, face economic water shortage (a lot of countries lack the necessary infrastructure to take water from rivers and aquifers)” UN (2013). Therefore, there is need to intensify efforts in improving the sources of energy to power the equipment used in pumping water in order to make water readily available. Often electric power is not readily available from the national grid in the remote areas where many farms are located. Installation of transformers and new lines may not be economical especially for remote locations.

Alternative sources of energy are necessary for off-grid small-scale water pumping. Photovoltaics (PV) and wind turbines are main alternative source of energy being explored. In this thesis, the distinction is made between a wind turbine which produces electricity that may be used to power a water pump, e.g. Muljadi et al. (1996), and a windmill where the turbine rotor directly drives a mechanical pump, usually a single acting piston pump, Pinilla et al. (1984). PV has witnessed a lot of improvement compared to the windmill, Mecke et al. (2004), and is falling rapidly in price. However, the windmill has been the most readily available because most of its parts can be sourced locally. Table 1.1 shows comparisons between the PV and the windmill as a stand-alone type water pumper.

Table 2.1: Comparison of the Advantages and Disadvantages of Windmill and Photovoltaic Water Pumping Systems adapted from Mecke et al. (2004).

Type	Advantages	Disadvantages
Windmill	<ul style="list-style-type: none"> • Cost less and low maintenance • create more job per dollar invested than any energy sources • Long-lasting can exceed 50 years , except for piston , which requires maintenance • Does not cause greenhouse gases or other pollutants. • It can be captured efficiently- steady wind are most productive • Can be manufactured in developing countries 	<ul style="list-style-type: none"> • The strength of the wind is not constant and it varies from zero to storm force • Wind turbines and possibly windmills are noisy • Wear more rapidly in high winds • Destructive wind can ruin the system
PV Powered System	<ul style="list-style-type: none"> • It is easy to install • low recurrent expenditure • It is in modular and handy • easy to increment the power supply by a small amount by adding more modules 	<ul style="list-style-type: none"> • High initial cost • low output in cloudy weather • Needs complex power electronics • Need specialised knowledge for trouble shooting • Panels can be damaged by hail • Usually imported

The windmill is an old technology and it is surprising that only limited information is available about the detailed aerodynamic performance. Pinilla et al. (1984) showed that a typical windmill has its maximum overall efficiency of just over 20% at about 70% of the cut-in wind speed. The

efficiency then drops rapidly with increasing wind speed. This is poor performance, it is therefore necessary to study the aerodynamics properties in order to be able to improve it and to ensure that windmills can make use of higher wind speeds. There is need for more experimental and numerical works to study the performance of airfoil sections of the windmills. This information is essential for performance analysis since the L and D on the blade elements determines the total torque and thrust produced by the rotor.

1.3. Windmill and Rotor Solidity

The major aerodynamic difference between the windmill and wind turbine is the arrangement of the blades and the area which the blade covers relative to the swept area. In a windmill the blades cover a larger fraction of the rotor swept area. This fraction is called the overall solidity, Σ . A typical electricity producing wind turbine has $\Sigma = 0.1-0.2$ while that of the windmill is in the range of 0.8 and above. The other measure of solidity is the local solidity, σ , is defined as the ratio of the product of number of blade elements and chord at a particular radius to the circumference of the rotor at a radius, and so can vary along a blade.

Solidity effects have to be taken into consideration when analysing windmills. The reason is that the fundamental method of analyzing wind turbine and windmill performance, blade element theory (BET), divides the blades into a number of sections (elements) and determines the thrust and power by assuming the elements behave as isolated airfoils (with zero solidity). The angle of attack, α , of each of the local section of the blade is found and this is used to estimate the C_L and C_D , which determine the torque contribution of the blade element. The sum of the torque

contribution over all the blade elements is then used to find the torque on one blade. This torque is multiplied by the number of blades to give the rotor torque.

If the effects of the solidity are not considered in windmill calculations, vital information may be missing. As far as the author is aware there are only very limited data available on solidity effects. This project aims at calculating the effect of solidity on the blade element in form of cascade and evaluating the changes in the C_L and C_D . C_L and C_D are defined as the ratio of the L and D to the dynamic pressure times the chord respectively. The results will later be used as input to the blade element momentum program, Wood (2011a).

The windmill is a slow running turbine, operating at low Reynolds number, Re . Re defined as $\rho U_\infty c / \mu$, where ρ is the density of air, U_∞ is the wind speed, c is the chord and μ is the dynamic viscosity of air. It is generally accepted that low Reynolds number effects occur at $Re < 500,000$, c.f. Wood (2011a), and can severely influence the airfoil L and D . The calculations described in Chapter 5 that match the Re of the experiments of Wegereef (1984) which will be reviewed later, show that the blade boundary layers are nearly always laminar, but often with separation with turbulence generated only in the separated flow. The Re of the wind tunnel experiment of Wegereef (1984) was 2.5×10^5 for a typical chord of 0.4m.

There are different types of blade depending on the sophistication. The simplest blades are usually rolled from sheet steel to approximate thin, CA airfoils with a central circular spar near the midpoint of the pressure surface. Figure 1.1 is a picture of typical windmill, at Eau Claire Market Mall Calgary, Alberta. As shown, the windmill has a high solidity compared with the

more common wind turbines shown in Figure 1.2. A high solidity machine generates much higher starting torque than low-solidity machines but is inherently less efficient than low-solidity machines, Singh et al. (2012). Low-solidity machines used to generate electricity and have to be made with more precision.



Figure 1.1: Windmill at Eau Claire Market Mall Downtown Calgary, Alberta.



Figure 1.2: Wind turbines generating electricity at Horse Hollow Wind Farm Nolan, West Texas, and the world's largest wind power project (Solidity 0.1 - 0.2). Photograph: Alamy
<http://www.guardian.co.uk/environment/2012/apr/29/wind-farms-night-temperatures-study>,
 accessed in March 013

Elementary BET makes use of isolated airfoil data in the form of C_L and C_D versus α and in doing so assumes that there is no interference between the blades of the windmill. Such an approximation is valid if the windmill σ does not exceed approximately 0.1. For higher solidity, the effect of the interaction between the blades cannot be neglected. The maximum C_L decreases in some cases significantly. Indeed, for $\sigma = 0.4$, the C_L can decrease by as much as forty-five percent from the isolated airfoil, Weick (1930). An important outcome of BET is that optimum turbine performance occurs when the ratio of L to D is maximized, so that windmill design and operation may well alter if full account was taken of solidity effects on L and D . The decrease in L might be compensated by a larger decrease in D .

1.4 Tip Speed Ratio

Tip speed ratio (TSR or λ) is an important parameter in the design of a wind turbine or a windmill. It is defined as the ratio of the rotational speed of the tip of a blade to the velocity of the wind:

$$\lambda = \Omega_a R / U_\infty \quad (1.1)$$

where Ω_a , is the angular velocity and R , is the rotor radius, $\Omega_a R$ is the circumferential speed of rotor tip. The optimisation of the TSR is important to get optimum power extraction. The maximum achievable power coefficient cannot be more than the Betz limit (59.26%) Magdi (2011). The optimal TSR depends on the number of blades. The fewer the number the faster the wind turbine must rotate to extract maximum power from the wind. The relationship between the number of blades and optimal TSR is $\lambda_{optimal} \propto 4\pi/n$ where n the number of blades, Magdi (2011). Therefore, as n increase, $\lambda_{optimal}$ will decrease. The water pumping windmill in Figure 1.1 has 24 blades.

1.5 Windmill Blade

The windmill blade section is usually a circular arc; as described earlier they are made from rolled metal sheet. A spar consisting of a circular tube extends along the blade, is used to reinforce it and hold it to the hub. Figure 1.3 shows a windmill blade with spar. Surface smoothness, airfoil thickness and airfoil camber all play an important role in the choice of airfoil for windmill. Many papers have been written on the effect of these properties of the airfoils generally at low Re . Okamo et al. (2005) considered the effect of camber at Re less than 10^5 , and

found that low camber airfoil have high C_D . Okamo et al. (1996) also found that increased airfoil thickness, decreased the aerodynamic performance.

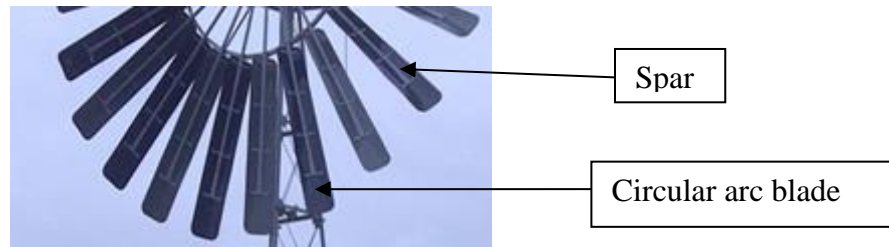


Figure 1.3 Windmill blades with spar

Two airfoil sections were considered in this project, those used in the experiments performed by Tezuka et al. (2008) and Bruining, (1979). Tezuka et al. (2008) used a 4% CA airfoil section, with a chord of 100mm, span of 300mm and thickness ratio (the ratio of the airfoil thickness to chord) of 1% at $Re = 62,000$. The model was constructed from rows of hypodermic tubes which allowed the surface pressure to be measured. Bruining used a two dimensional model of a curved plate with 3mm thickness and 10% camber. The model has a span and chord of 0.75m and 0.15m respectively and was tested at Re in range from 60,000 to 350,000. The Bruining model was made from the conventional rolling of metal sheet into approximate thin, CA airfoils and only the L and D were measured.

The characteristics of the blade were determined with and without spar. The spars were placed at different positions along the blade chord, and on the pressure and suction sides. All windmills that the author is aware of, have the spar on the pressure side as shown in Figure 1.3. Blades are

twisted with pitch varying along the length. The pitch is the angle between the chord line of the blade and the plane of rotation. Its variation along a blade allows the maintenance of optimal angles of attack as the velocity vector changes direction due to the rotational component.

1.5.1 Blade Geometry: Circular Arc Airfoil (CA)

The circular arc airfoil is defined in Figure 1.4. The camber is h , while the leading edge, LE, is the most forward and the trailing edge, TE, is the most rearward point of the airfoil. Δt is the thickness and c is the chord, α is the angle of attack which is the angle between the relative wind U_∞ or the effective flow direction and the airfoil chord line shown as dashed line. Relative wind velocity is used in order to relate the moving airfoil to the stationary test.

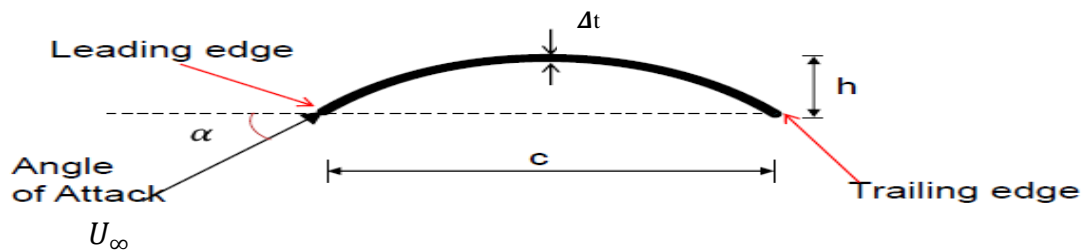


Figure 1.4: Circular Arc Airfoil

1.5.2 Blade Solidity

Since the airfoil is the two-dimensional representation of a blade element at zero solidity, a finite solidity blade can be represented as a cascade of airfoils. A cascade of airfoils is defined as an infinite row of equally spaced airfoils. The effect of solidity on C_L and C_D is calculated using numerical simulation or found from experiments. Figure 1.5 shows two elements of a cascade,

which extends infinitely up and down the page. The local solidity, σ is the ratio of chord to spacing, c/s .

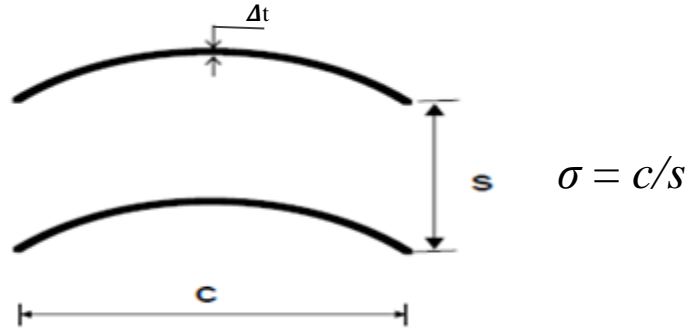


Figure 1.5: Two components of a cascade

1.6 Numerical Model for the Flow

The wind tunnel test for the CA is in the range of 6×10^4 - 3.5×10^5 for Bruining (1979) and Tezuka et al. (2008). ANSYS FLUENT was used in this project to simulate the flow over an isolated airfoil and cascades. The steady averaged Navier-Stokes, N-S, equations were solved by the four-equation Shear Stress Transport-transition (SST-transition) model which solves the initial laminar boundary layer, detects the onset of transition, and uses a detailed model for the transition to turbulence, Menter (2012). The modeled equations of transition are based on two transport equations, the first one for the intermittency, γ and the second for the momentum thickness Re , Re_θ , Suluksna et al. (2008). γ is the proportion of time that the flow is not laminar while the important correlations for Re_θ were obtained from experiment.

Solving low Re problems requires good transition prediction because the laminar boundary layer formed at the LE may well extend over a large fraction of the airfoil's upper and lower surfaces.

If the transition region and the onset of turbulence are not well predicted, C_L and C_D will not be predicted accurately. Using a full turbulence model from a user specified transition point near the LE is thus unlikely to provide good results.

The SST-transition model has been used in low Re numerical calculations and validated with experiment. More information will be provided in the literature review. In this thesis, the SST-transition model was used initially to calculate the pressure distribution for the experiment performed by Tezuka et al. (2008), on a CA airfoil with 4% camber and subsequently used to determine the C_L and C_D on a 10% camber circular arc airfoil for the experiment of Bruining (1979). Then the cascade effects on C_L and C_D were calculated for range of σ between 0.1 and 1.5. The lower solidity was considered in order to compare the result with the isolated airfoil experiments mentioned above. Since the ultimate aim of this work is to provide information for a BET model of windmills which will be compared to experiments, the range of σ was obtained from the wind tunnel tests of windmills by Wegereef (1984).

The literature review for the thesis is given in chapter 2. Chapter 3 describes the transition, turbulence model and numerical modelling. The approach will be to describe the transition modes and the numerical techniques used in the thesis. Chapter 4 provides the results of the zero solidity calculation of the two experiments considered in the thesis. Chapter 5 describes the effect of L and D and the study of the flow patterns on the cascade calculations. The main body of the thesis closes with chapter 6, conclusions and recommendations for future work.

Chapter 2: Literature Review

2.1 Windmill Background

Wind energy is one of the oldest forms of energy used to supplement human muscle. The windmill is a low Re machine designed to deliver high torque for pumping water in low winds. In the late 1300's the Dutch developed new sails designs that increased its efficiency. The windmill applications were brought to Canada by the French in the 17th century used for grinding grain, Kentfield (2013).

Initially, wooden blades were used on windmills and later development witnessed the introduction of steel blades, as some wooden blades could fracture in a very high wind. As the windmill witnessed limited development over the years, most of its applications have not changed from the fundamental use for grinding grains or pumping water for irrigation and domestic use. Pinilla et al. (1984) reviewed the existing field test data for water pumping windmills. These measured the performance of single acting lift pumps and high solidity windmills to determine the maximum possible system conversion efficiency in terms of the wind speed. Pinilla et al. (1984) found that lower solidity, faster running wind turbine designs when coupled to a reciprocating lift pumps yield poorer wind to water conversion efficiencies than the traditional high solidity multiblade design.

2.2 Experiments on Windmill Blades

The construction of a windmill blade is simple as explained earlier, the cross section is in form of CA with varying cambers, thickness and chord depending on the application. There is no specific design for windmill blades and limited study has been done on the circular arc airfoils. Perhaps this is the reason why the development in windmill design has been very slow. Figure 2.1 shows typical curved windmill blades prior to assembly of the rotor.



Figure 2.1: Arrangement of windmill blade under construction (from <http://waterfromyk.wordpress.com/>) accessed in March 2013

Sunada et al. (2002) compared the performance of a range of airfoils at Re less than 10^5 . Kunz and Kroo (2000) undertook computational modelling of airfoils at in the range $10^3 < Re < 10^4$. The results indicated that thin airfoils of about 5% camber have high lift to drag. There is considerable data on the lift and drag of circular arc airfoils e.g. Wallis, (1946), Ikui et al. (1972), Bruining, (1979), Pandey et al. (1988), Okamoto et al. (2005) and Tezuka et al. (2008). Bruining's is the most useful for the present work because the experiment was performed at a high quality wind tunnel, with a very low turbulence intensity, turbulence intensity is the ratio of

the root-mean-square of the turbulent velocity fluctuations to the mean wind speed and it is the only experiment that determined L and D with and without a spar over the range of Re necessary for the experiments of Wegereef (1984) and, therefore the present calculations.

Bruining (1979) performed extensive experiments on circular arc airfoils which was motivated by windmill applications. He determined the C_L and C_D on the CAs of 10% camber. He placed a spar at different positions on the airfoil in order to determine the influence on the C_L and C_D . The experiments were performed at $-10^\circ < \alpha < 90^\circ$ and at Re between 60,000 and 200,000. As shown in Figures 2.2 to 2.4, the profile shows similar pattern with the maximum $C_L=1.6$ obtained at Re of 200,000, while for Re of 60,000 and 100,000, C_L peaked at 1.5.

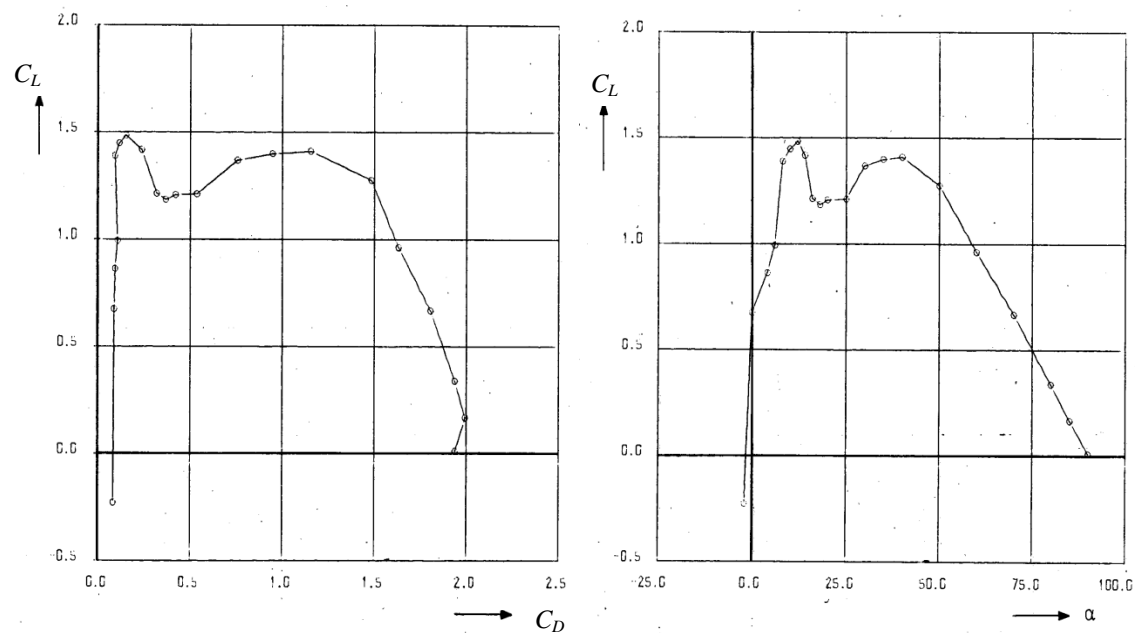


Figure 2.2: Section characteristics of circular arc airfoils at $Re = 60,000$ Bruining (1979).



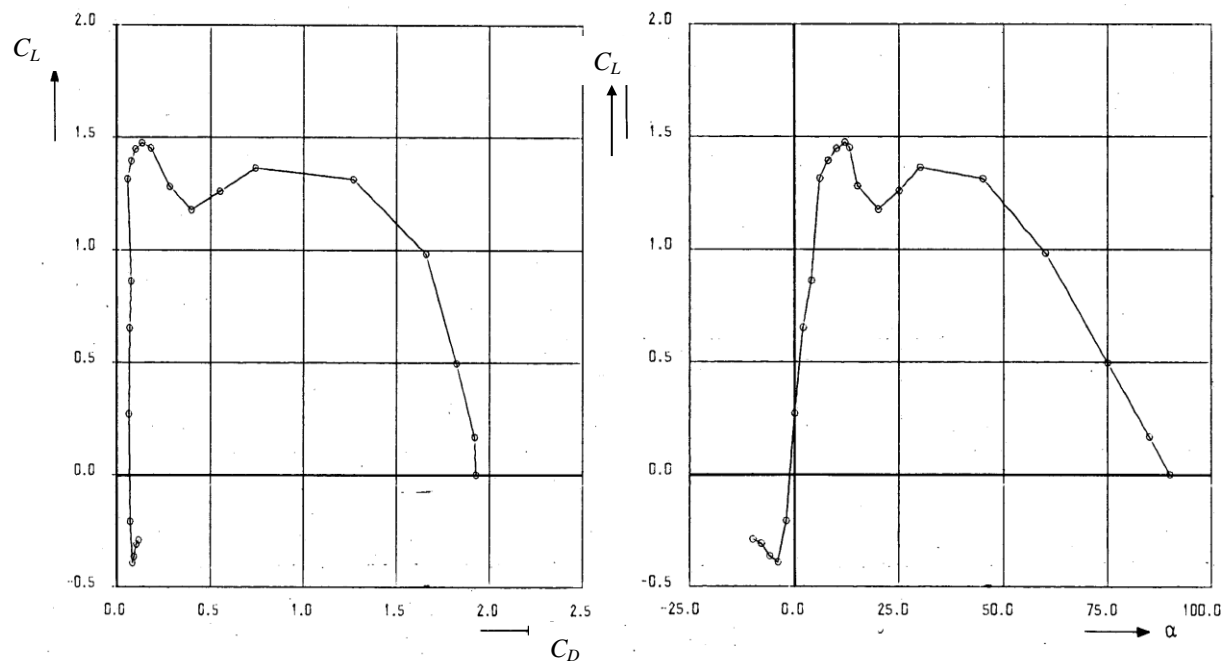


Figure 2.3: Section characteristics of circular arc airfoils at $Re = 100,000$
Bruining (1979).

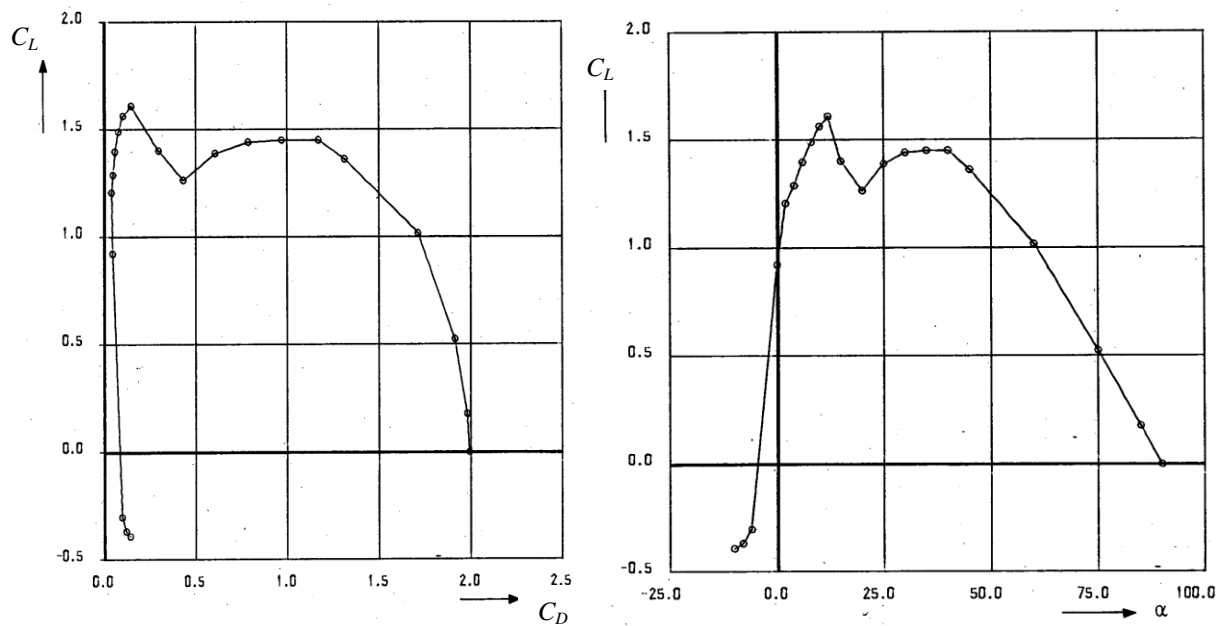
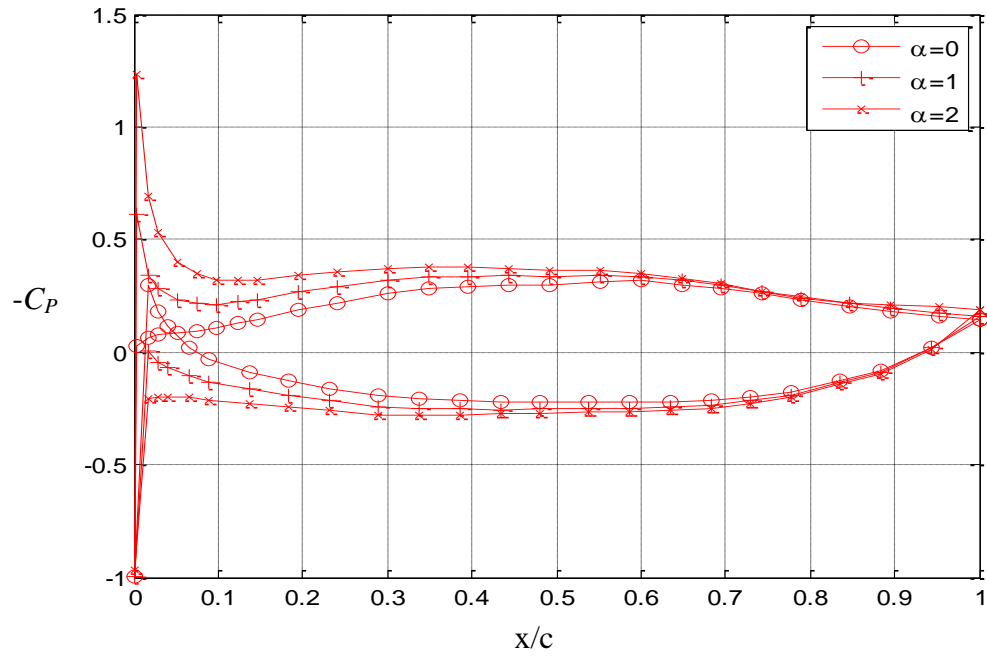
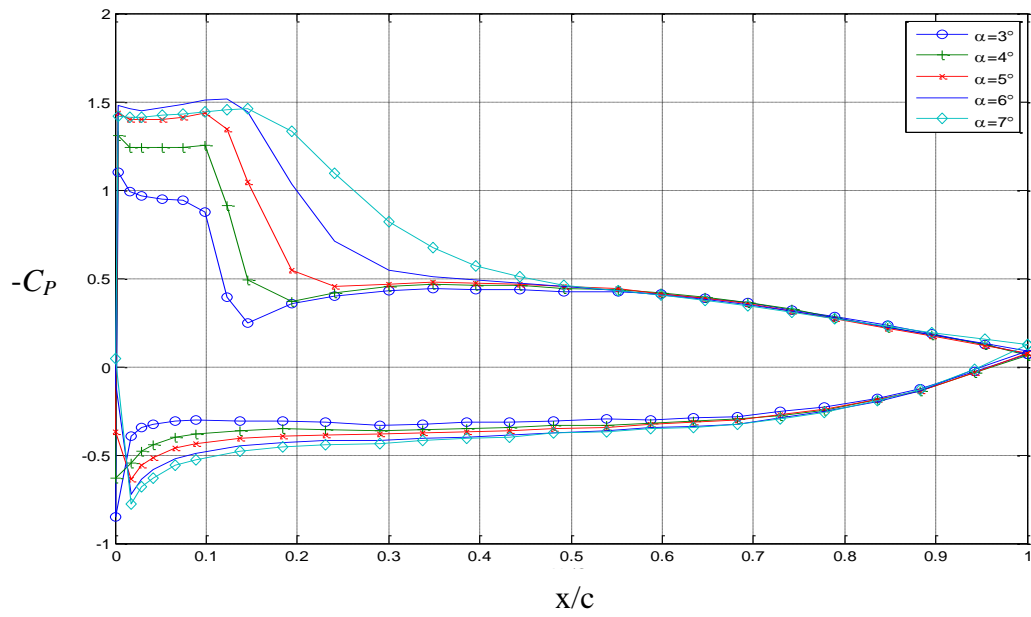


Figure 2.4: Section characteristics of circular arc airfoils at $Re = 200,000$
Bruining (1979).

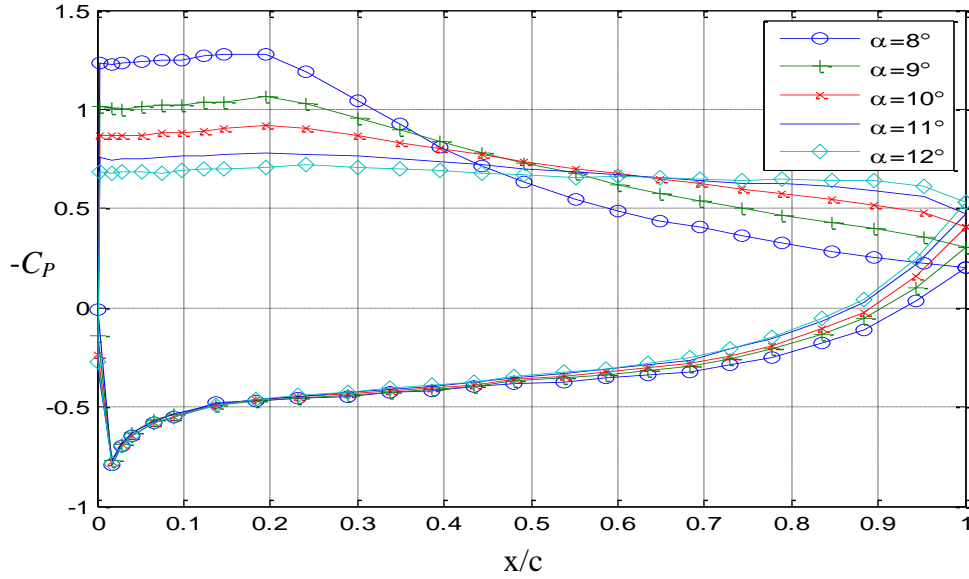
Although, L and D are required for BET analysis, they do not give detailed information on the state of the airfoil boundary layer or make it easy to adjust the constants in the transition or turbulence model to predict the separation of the laminar boundary layer, the almost immediate transition to turbulence in the resulting separation bubble, and its possible reattachment further downstream. For this, at least the pressure distribution is required. Tezuka et al. (2008) measured the surface pressure distribution on 4% circular arc airfoil $Re = 62,000$, for α between 0° and 12° . They classified the flow into three parts corresponding to the angle of attack as shown in Figure 2.5a-c, $0^\circ \leq \alpha \leq 2^\circ$, $3^\circ \leq \alpha \leq 7^\circ$ and $8^\circ \leq \alpha \leq 12^\circ$. For $\alpha=0$, the coefficient of pressure, C_p curves shows that less than 5% of the chord the suction on the lower surface was greater than on the upper surface thereby generating a negative L with in this region. However, for the remainder of the lower surface for $\alpha=0$, the contribution to L is positive. This is an indication that the aerodynamics of circular arc airfoils are different from conventional profiles, where the pressure is always positive on the lower surface for $1^\circ \leq \alpha \leq 12^\circ$.



(a) $0^\circ \leq \alpha \leq 2^\circ$



(b) $3^\circ \leq \alpha \leq 7^\circ$

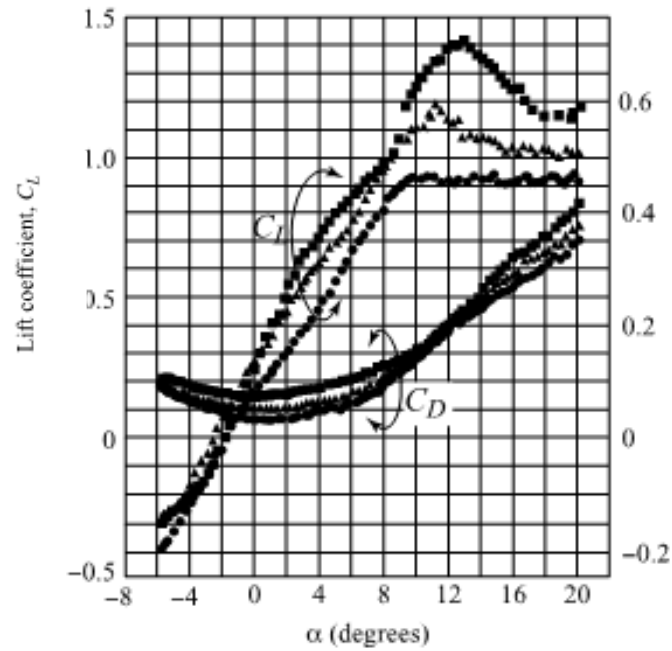


(c) $8^\circ \leq \alpha \leq 12^\circ$

Figure 2.5(a-c): Surface pressure measurements on 4% circular arc airfoil at low Re Tezuka et al. (2008). Data provided by Prof. K. Inoue.

Cambered plates have better aerodynamics characteristic than flat plates, Okamoto et al. (1996). They found that, as the camber increased, the C_L slope and the maximum C_L increased as shown in Figure 2.6. The lower camber of 3%, gave a lower C_L for $-6^\circ \leq \alpha \leq 20^\circ$ at $Re = 10^4$. It was also observed that the C_L for higher camber was higher for the same range. The significance of this is that when designing windmill blades, the optimal camber of the windmill blade should be considered. Since the BET depends on L/D , these results suggest that higher camber would improve windmill performance. Sunada et al. (2002) investigated the impact of camber location and found that both C_L and C_D increases as the position of the maximum camber approaches the TE.

(a)



(b)

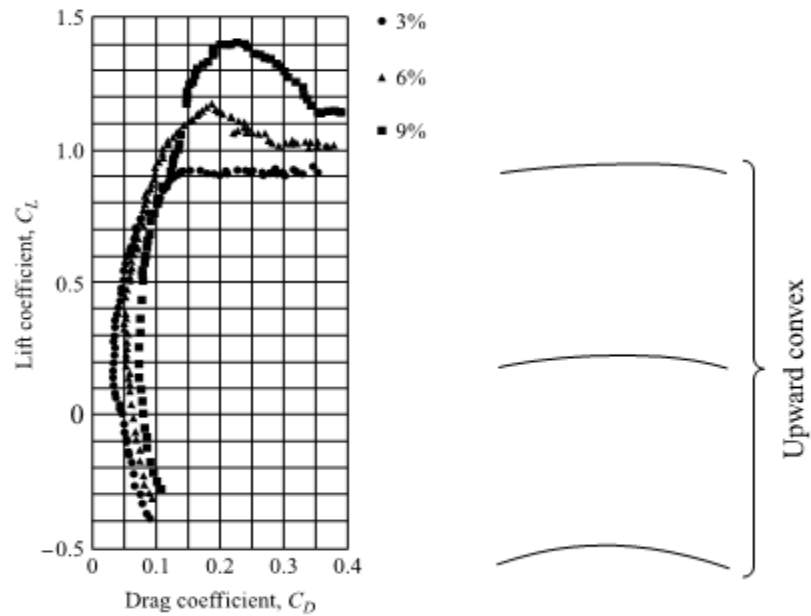


Figure 2.6(a-b): Effects of camber on the aerodynamic characteristics of rectangular model wing from aluminium foil, with a thickness of 0.3 mm and a chord length of 30mm. Each symbol refers to different camber as shown in the panel on the right hand side of the figure (a) C_L and C_D vs α (b) Polar curve. From Okamoto et al. (1996) with permission.

Furthermore, Mueller (2000) showed that the thickness of the CA airfoil influences the aerodynamic characteristics, for turbulence intensity, Tu , up to 1%. Okamoto et al. (1996) showed effects of thickness on the aerodynamics characteristics of CA with camber of 9% and a wedge airfoil as indicated in Figure 2.7. As the thickness of the curved section model increases, its aerodynamic characteristics deteriorate. However, the maximum C_L is obtained for the thin curved plate with camber of 9% (first shape on the right hand side in Figure 2.7). The remaining airfoils are the wedge airfoils.

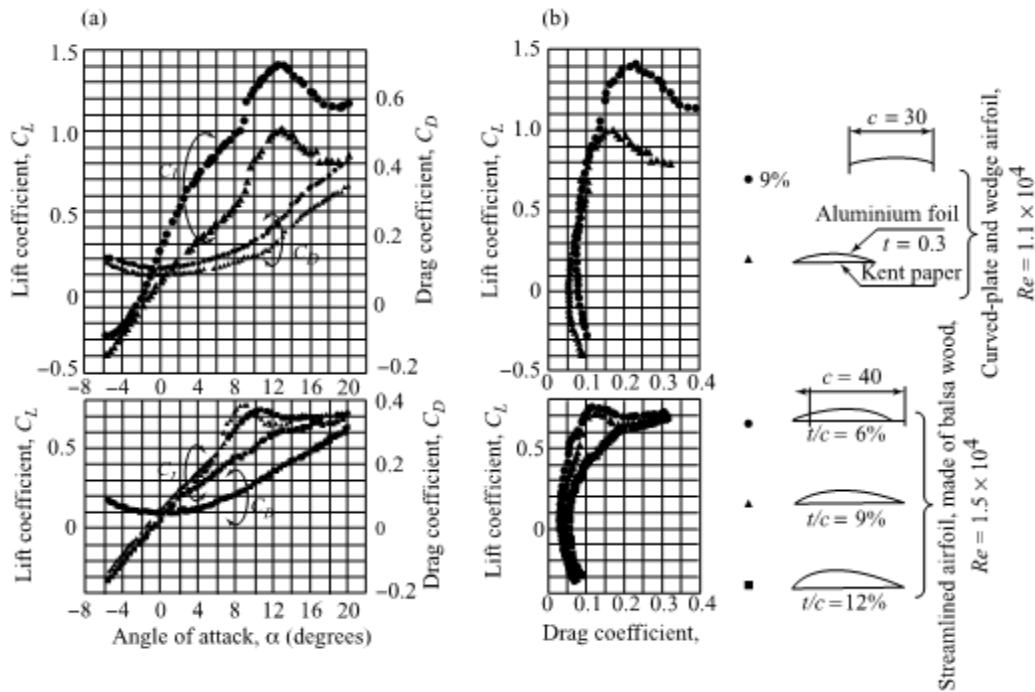


Figure 2.7: Effects of thickness on the aerodynamic characteristics of a curved - section model wing (camber 9%). Each symbol refers to a different airfoil shape as defined in the panel on the right hand side; c , chord length; t , thickness; Re , all dimensions are given in millimeters (a) C_L and C_D vs α (b) polar curve. From Okamoto et al. (1996) with permission

The optimization of windmill performance relies on many factors and variables, including blade number, rotor solidity, blade pitch, and λ . This thesis will consider only the correction to the

blade L and D which are often neglected in performance models. Wegereef (1984) investigated the performance of 24, 12 and 6 bladed rotors which used identical blades, and observed that there is an increase of 9.5% in maximum power and a reduction in the starting torque for 12 bladed rotors compared to 24 blades. If solidity effects were not important, then changing number of blades (n) would not change maximum power coefficient, C_p , so the difference in C_p , max between $n = 12$ and 24 is a clear demonstration of the importance of solidity. It was also established that an increase in stagger angle from 10.5° to 17° at the blade root produced more starting torque, maximum torque and maximum power coefficients at lower TSR. The stagger angle is the angle between the chord line and the turbine axial direction and is 90° -pitch.

2.3 Cascade Effects

The challenges associated with the computational modelling of complex flow field like cascades have decreased over the last few decades. Today CFD can be used to obtain two dimensional (2-D) cascade aerodynamics coefficients at any pitch angle but it is still important to use experimental results to test their accuracy. The experimental study of cascade of airfoils at high pitch angle is difficult or almost impossible in the wind tunnel, Raghunathan et al. (1995). However, cascade effects are crucial to the performance of highly cambered gas turbine and compressor blades so there is a large experimental and computational literature. Only those parts of direct relevance to the present work will be reviewed with emphasis on blades of similar shape to CA airfoils and Re ranges typical of windmill operation.

Before the advent of CFD, experiments were compared with theoretical calculations. Katzoff et al. (1947) compared the theoretical and experimental C_L and pressure distribution on NACA 6 series airfoils in cascade. The experimental C_L were considerably less than the theoretical, for solidity of 1.0 and the differences were greater than the differences between theoretical and experimental value for the isolated airfoils. The solidity decreased the L and increased the D .

An important contribution to cascade studies was by Weinig (1964). His work predicted the interference factor, k_i , the ratio of the coefficient of lift of blade in a cascade and the coefficient of lift of an isolated blade taken at the same incidence for a linear cascade of infinitesimally thin flat plates using potential flow. A linear cascade is the arrangement of identical airfoil spaced with equal distance, with the LE and TE of each airfoil collinear. Weinig determined the conditions under which the flow enters the cascade smoothly without infinite velocities at the LE. He predicted the interference effects for L . His work has been used by several researchers to modify the isolated airfoil's C_L for cascade applications.

Figure 2.8 shows Weinig's results for k_i on $1/\sigma$ for several stagger angles. It is notable that there is asymptotic convergence of k_i as σ approaches unity. Weinig's method is inviscid so that only C_L could be estimated. The estimate of the C_L for an isolated aerofoil prior to stall is given as

$$C_L = 2\pi k_i \sin(\alpha_m) \quad (2.1)$$

where α_m is the mean angle of attack based on the mean velocities downstream and upstream of the cascade.

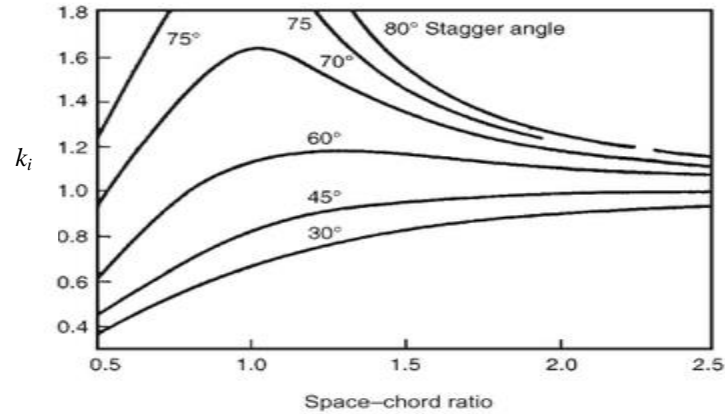


Figure 2.8: Weinig's results for lift ratio of cascade of thin flat plates, showing dependence on stagger angle and solidity (from Dixon 2005).

Zierke et al. (1989) calculated the flow over compressor cascade blades similar to a CA, at three different inlet angle of 5° , -1.5° and -8.5° for $\sigma = 2.14$. The effect of streamwise resolution for the calculation was deemed important near the LE in order for the SST-transition model used to be able to capture the laminar separation and subsequent transition on the suction side. Another important result was that increasing the inlet angle changed the position of the stagnation point from the suction to the pressure surface of the blade. For the subsequent laminar boundary layer, the pressure gradient begins as favourable. Further downstream, an adverse streamwise pressure gradient either causes the laminar boundary layer to separate and/or go through transition. On the surface opposite the stagnation point, the severe adverse pressure gradient results in a laminar separation bubble, (LSB), in which the flow transitions to turbulence, a phenomenon that occurs only at low Re , Zierke et al. (1989). The LSB is associated with reverse flow after the separation of the boundary layer and then the boundary layer reattaches enclosing the bubble. The dynamics of a LSB depends on the value of the Re , the pressure distribution, the geometry, the surface roughness and the free stream turbulence Shyy (2008).

The turbulence kinetic energy contours and the skin friction distribution are shown in Figure 2.9. Turbulence can be defined as the state of fluid in an irregular condition of flow in which the various quantities show random variations with time and space coordinates, so that statistically distinct average values can be discerned, Hinze (1975). The skin friction (C_f) is the normalized tangential force per unit area created on a surface that is exposed to a flowing viscous fluid. From the C_f distribution in Figure 2.9, the points of separation and reattachment can be determined. The region of LSB occurs where the C_f is negative on the pressure side according to the author, the previously attached laminar boundary layer encounters an adverse pressure gradient of sufficient magnitude to cause the flow to separate and form a bubble, Zierke et al. (1989). The pressure coefficient distribution is shown in Figure 2.10. The good agreement between the measured and computed surface pressure is typical of the best that has been achieved and will be used as a benchmark when comparing the current CFD results with measurements in chapter 4. There was no information on the calculated C_L and C_D .

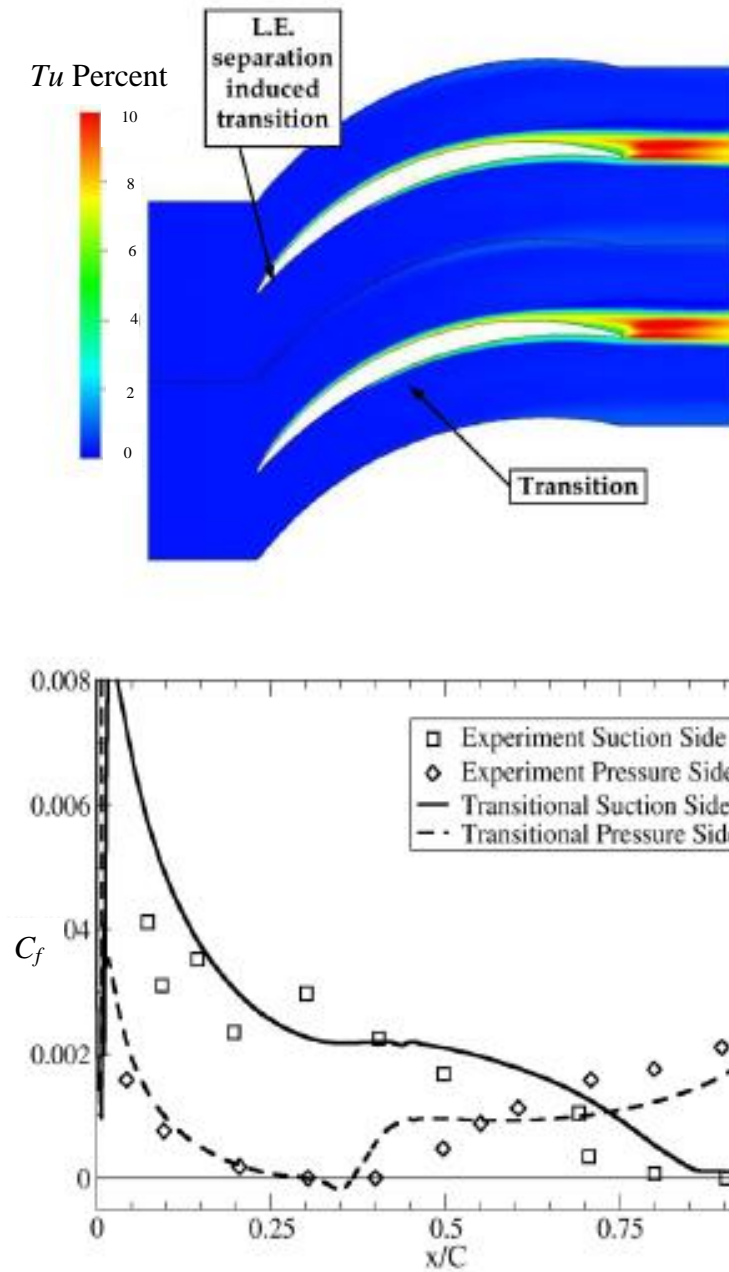


Figure 2.9: Turbulence intensity contours (top) and computed C_f -distribution against experimental data for compressor cascade blades from Zierke et al. (1989).

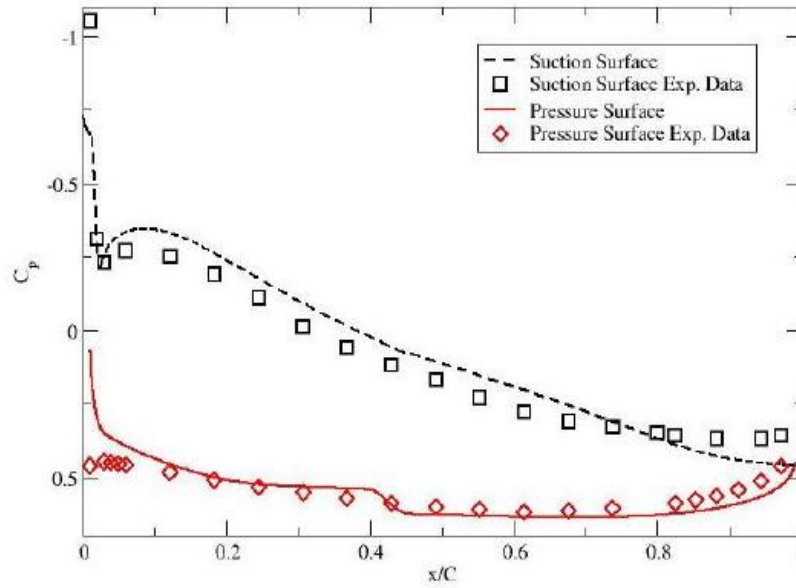


Figure 2.10: Pressure coefficient results for the Zierke et al. (1989) compressor cascade.

Ahmed et al. (1998) numerically studied on the flow field around a cascade of NACA 0012 sections, using the standard, and often used, $k - \varepsilon$ model, ANSYS (2011). The investigations covered the boundary layers on the pressure and suction surfaces of the airfoil, the pressure, C_L and C_D for α between $0^\circ - 24^\circ$, at $Re = 3.24 \times 10^5$, and σ ranging from 0.55 to 0.83. The incoming flow was considered as turbulence free. The inlet and outlet boundaries were placed $4c$ upstream of the LE and $5c$ downstream of the TE, respectively. The upper and lower boundaries of the computational domain were made periodic in order to simulate an infinite cascade. They found that the L and D both increased as α increased, but as the σ increased the α at which maximum L is obtained also increased.

Eftekhari et al. (2012) studied both numerically and experimentally the σ and incidence effects on the performance of a cascade of axial compressor blades with similarities to a CA. The

studies cover σ between 1.2 and 0.8. It was established that increasing the σ reduced the pressure as the velocity increased. They also found that separation of the flow in blades decreased the efficiency, the value which was not mentioned in the paper. The variation of pressure coefficient for solidity of 1.2 and 0.8 are shown in Figures 2.11 and 2.12.

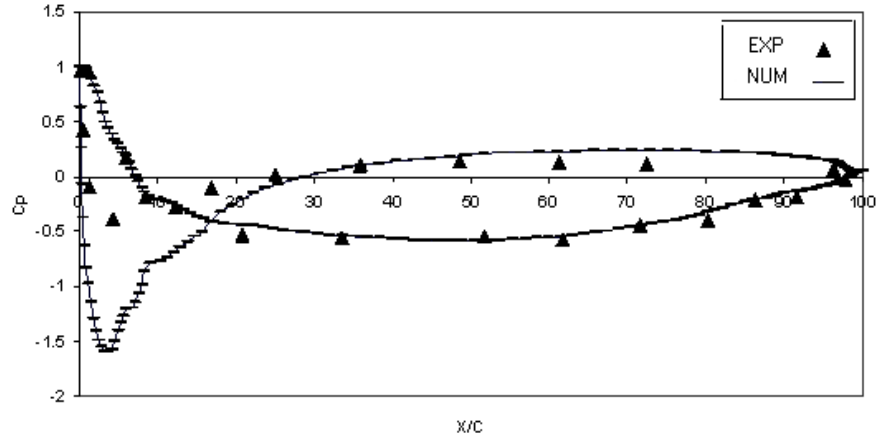
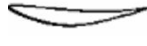


Figure 2.11: Variation of pressure coefficient at solidity of 1.2  Eftekhari et al. (2012)

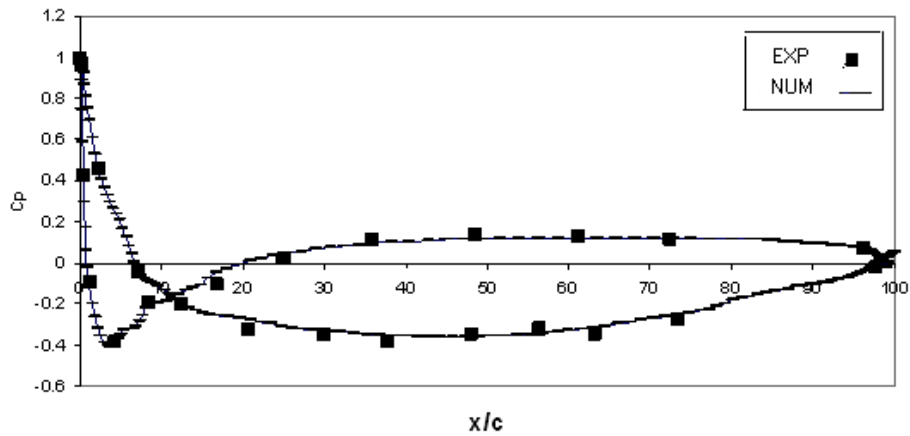



Figure 2.12: Variation of pressure coefficient at solidity of 0.8  Eftekhari et al. (2012)

Köktürk (2005) used the Spalart-Allmaras turbulence model to study the aerodynamic performance of a cascade of elliptical profiles for Re between $0.6 - 1.5 \times 10^6$, $0.1 \leq \sigma \leq 2$ and $0^\circ \leq \alpha \leq 30^\circ$. The unstructured grids for the infinite number of blades were modeled in Gambit 2.0 and the flow solved using FLUENT 6.0. The mesh used was composed of triangular elements. The inlet and outlet were positioned at $4c$ from the LE and TE respectively. The inlet boundary condition was set as velocity inlet, which requires the velocity to be specified. The magnitude of the inlet velocity was 70m/s based on the Re and the c . The outlet boundary condition was set as pressure outlet, which requires specifying static (gauge) pressure at outlet. The pressure at the outlet was defined as atmospheric. The observed static pressure distribution on the blade surfaces for σ of 1.5 and 0.1 are shown in Figures 2.13 and 2.14. In the case of σ of 0.1 there was no reattachment after the flow separated because of its low σ .

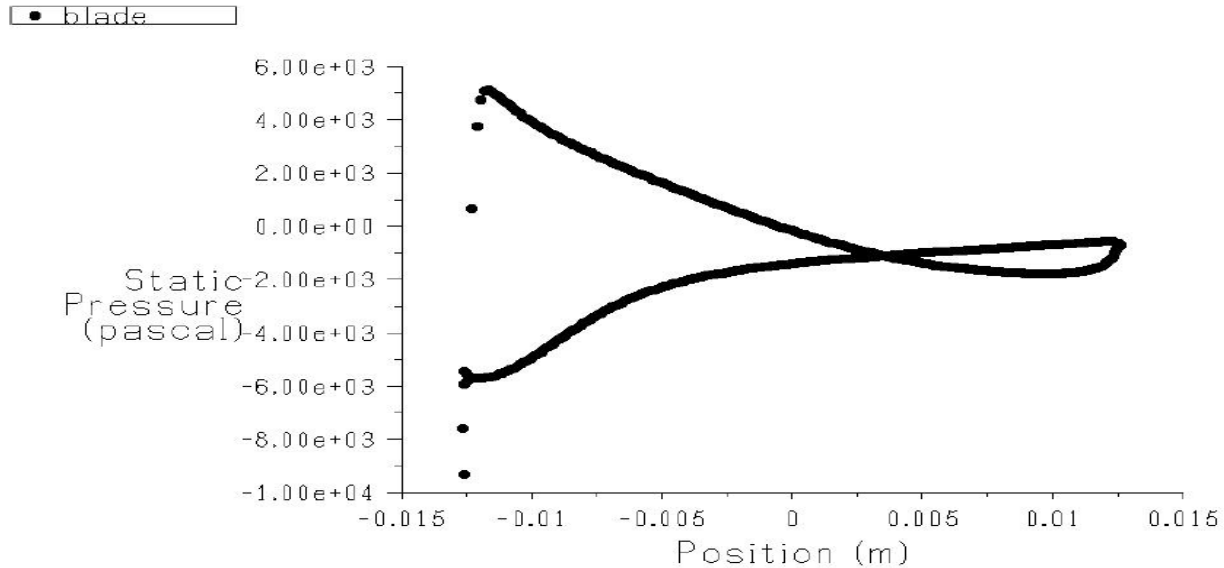


Figure 2.13: Static pressure distribution on the blades with $\sigma = 1.5$ Köktürk (2005)

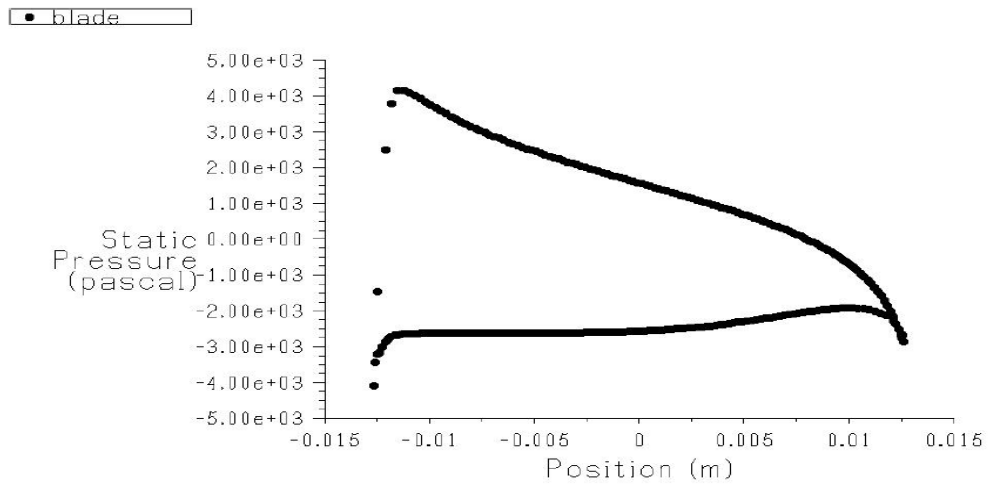


Figure 2.14: Static pressure distribution on the blades with $\sigma = 0.1$ Köktürk (2005)

Figure 2.15 shows that increasing the solidity, adversely affects the C_L . From Figure 2.16 the effect on the C_D is similar that on the C_L . There was no experiment available for the comparison to the calculation.

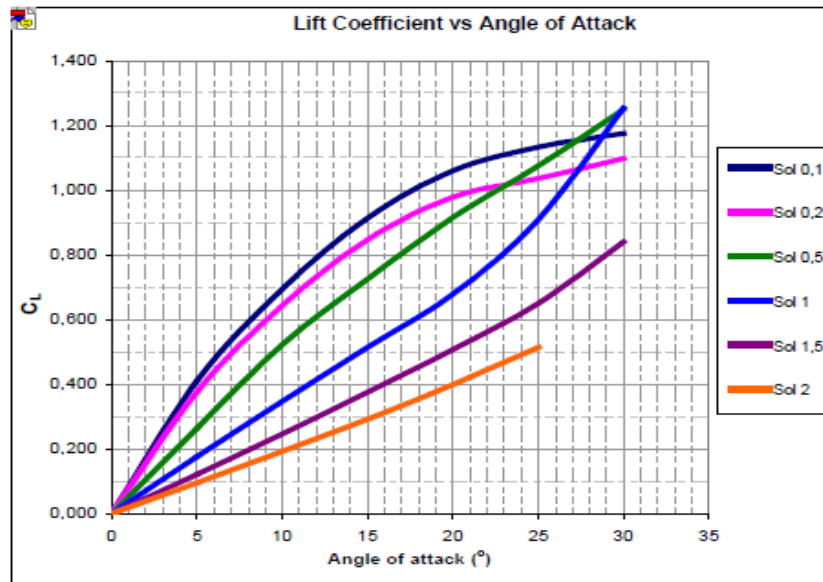


Figure 2.15: C_L vs. α at different σ , at velocities of 70m/s Köktürk (2005)

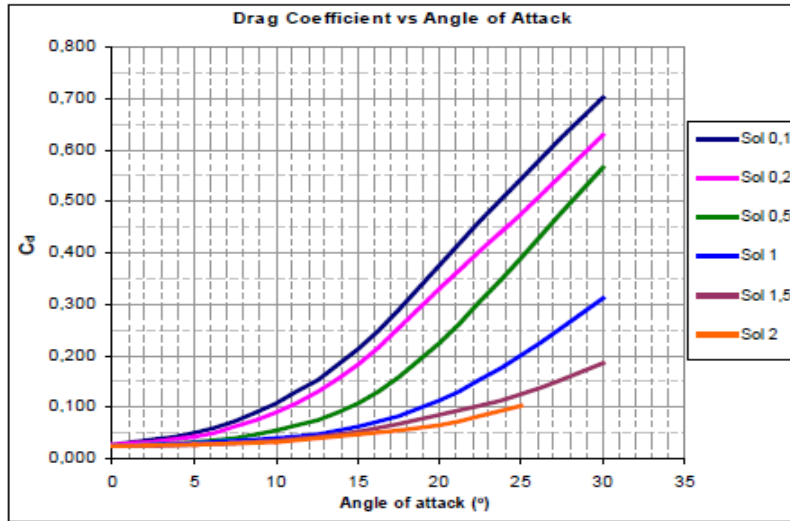


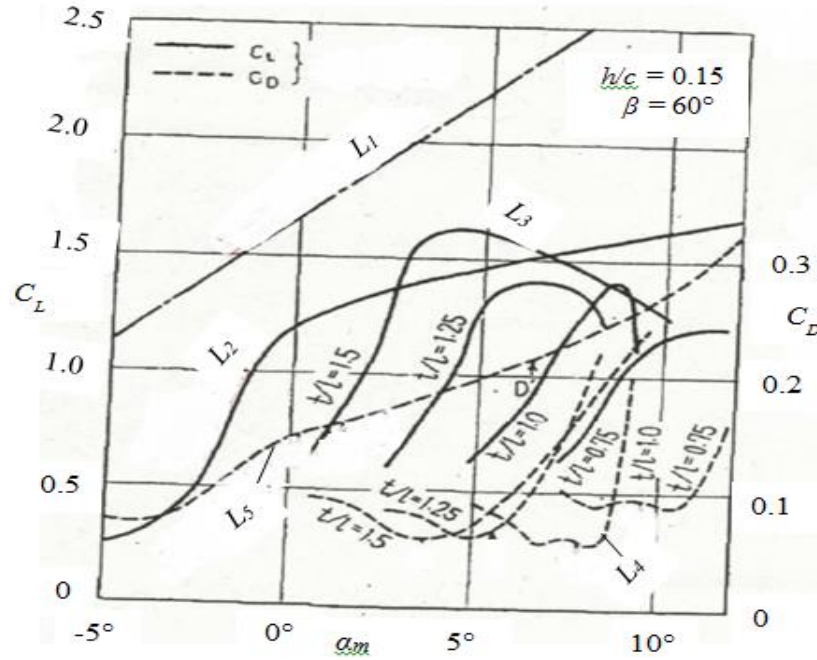
Figure 2.16: C_D coefficient vs. α at different solidities Köktürk, (2005)

Gareev et al. (2009) did a CFD analysis of blades for an oscillating water column turbine, by computing the L and D characteristics of the cascade of blades and relating the result to an isolated airfoil. At $\alpha \leq 10^\circ$, Weinig's inviscid flow analysis provided an accurate prediction of interference factor for lift, k_i but did not account for the finite thickness of practical blades in a cascade. Gareev et al. (2009) demonstrated that the L and D of a single airfoil and an appropriate interference factor may be used effectively to account for σ in blade element analysis.

Suzuki et al. (2011) predicted cascade performance of circular arc blades with CFD, but there was no information on the exact turbulence model. The calculations were performed for camber angles $\theta_c = 13.73^\circ, 31.88^\circ, 49.63^\circ$ and 66.88° , defined as the sum of the angles formed by the chord line and the camber-line tangents at the LE and TE for $\sigma = 0.666, 1.0$ and 1.33 at $Re = 1.9 \times 10^5$ of the experiment performed by Ikui et al. (1972). The CFD analysis over-estimated the

turning angle which is the difference between the inlet and exit flow angles of the cascade. On the other hand, the total pressure loss coefficient was under estimated. The total pressure loss coefficient is the difference in total pressure between the inlet and outlet divided by the dynamic pressure of inlet velocity. They concluded that the deviation from the experiment may be an indication of the inaccuracy of the transition model.

Ikui et al. (1972) did some researches on 2-D cascade, part of which was an experiment on the cascade performance of CA blades with $c = 0.1\text{m}$ and $1.5 \leq 1/\sigma \leq 0.75$. The inverse solidity, $1/\sigma$ is t/l in the graph in Figure 2.18 taken from their paper. $Re = 1.9 \times 10^5$. The C_L and C_D for flow inlet angle $\beta = 60^\circ$ for a cascade from the experiment compared with isolated blade are shown in Figure 2.17. L_1 is the theoretical C_L while L_2 is the experimental C_L for isolated airfoil. The cascade results are L_3 and L_4 respectively, corresponding to C_L and C_D for the experiment. L_5 is the isolated airfoil experimental C_D . This experiment shows that as solidity increased the maximum C_L decreased. Figure 2.18 shows the maximum C_L / C_D and mean angle of attack, α_m , plotted against σ . α_m is the mean of the angle between the inlet and outlet angles in cascade. The result shows that the maximum C_L / C_D occurred at $\sigma = 1$ and α_m increased with increasing σ .



. Figure 2.17: C_L and C_D against α_m for isolated CA and the cascade from Ikui et al. (1972)

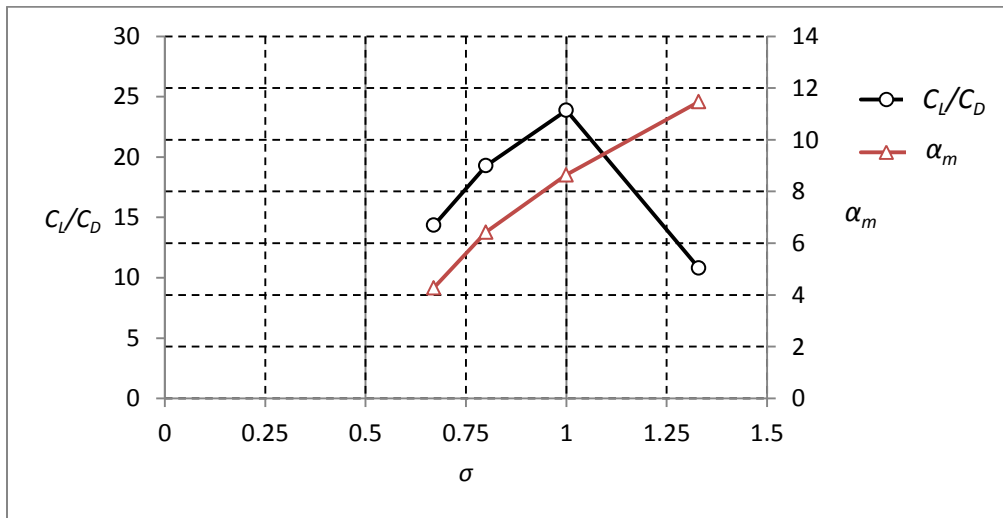


Figure 2.18: Maximum C_L / C_D and α_m , data was read from Figure 2.17

2.4 Summary of the Previous Literature

The literature on solidity is a mix of experimental and numerical analysis. The CFD has shown to be a significant tool in the analysis of cascade for its robustness and accuracy in analysis of

conditions that are difficult to set up experimentally. The most significant conclusion is that an airfoil can be simulated with periodic boundary condition to make it a cascade of airfoils. This saves a lot of computational time. In most of the numerical work done on cascades, the length of the upstream and downstream is limited to between $1c$ and $2c$ upstream of the LE and between $2c$ and $5c$ downstream of the TE. Generally, results have shown that L and D are significantly affected by σ but there is no simple correlation on the effects. Both L and D reduce as the solidity increases. Suzuki et al. (2011) found that accurate prediction of the transition is not easily obtained at low Re .

The choice of turbulence model was motivated by the need to accurately determine transition in order to resolve the flow on the airfoils studied in this thesis. Zierke et al. (1998) used the SST - transition model for compressor cascade calculations for the solidity of 0.47 and similar α used. They compared their results to surface pressure and wall shear stress measurements. The model is a turbulent transition model formulated to ensure that the viscous sublayer was resolved by mesh. Zierke et al. (1998) showed the extent to which the model is able to predict the separation of the laminar boundary layer. However, the limit of the model is that separation was usually over-predicted which caused a minor discrepancy in the numerical results and the experiment. However, Figures 2.9 and 2.10 show an impressive agreement between the measurements of surface pressure and shear stress and the calculations. On these grounds it was decided to use the SST-transition model for the present thesis but it was anticipated that some adjustment of the transition model constants would be required.

Chapter 3: Transition, Turbulence and Numerical Modelling

3.1 Turbulence Modeling

Turbulence is characterized by random fluctuations of various flow properties. Hence, a statistical approach is used to solve turbulent flows. Reynolds introduced the concept of representing the flow properties as the sum of mean and fluctuating parts. All the equations in this section were from Wilcox (2006). For example, the instantaneous velocity $u_j(x, t)$ is decomposed into a mean value $U_j(x)$ and a fluctuating component $u'_j(x, t)$.

$$u_j(x, t) = U_j(x) + u'_j(x, t) \quad (3.1)$$

This is known as Reynolds decomposition. The same concept can be applied to other flow properties, pressure, temperature etc. Essentially, turbulent fluctuations have 3-D spatial character. Turbulent flow is comprised of eddies which can bring close fluid particles that was initially separated. This causes the heat, mass and momentum to be exchanged much more rapidly than by purely molecular (diffusion) means. Time averaging is appropriate for stationary turbulence, the time average is defined by

$$\bar{U}_j(x) = \lim_{\tau \rightarrow \infty} \frac{1}{\tau} \int_t^{t+\tau} U_j(x, t) dt = U_j(x) \quad (3.2)$$

where τ is the integration time, the over bar is the time average. Obviously, time averaging of the mean is the mean. The time average of the fluctuating part of the velocity is zero. It is important to note that infinite τ cannot be realised in any physical flow, therefore very long τ is taken relative to the inverse of the maximum frequency of the velocity fluctuations. Reynolds averaging is applied to N-S equations. Equations (3.1) and (3.2) in appendix A yields Reynolds

Averaged N-S equations of motion known as RANS equations. The RANS mean momentum equation is in Cartesian co-ordinates is

$$\frac{\partial U_j}{\partial t} + U_i \frac{\partial U_j}{\partial x_i} = -\frac{\partial P}{\partial x_j} + \frac{\partial}{\partial x_i} (2\mu S_{ij} - \overline{\rho u'_i u'_j}) \quad (3.3)$$

Wilcox (2006). The stress tensor is defined by

$$t_{ij} = 2\mu S_{ij} - \overline{\rho u'_i u'_j} \quad (3.4)$$

where μ is the molecular viscosity and S_{ij} is the mean strain-rate tensor given by

$$S_{ij} = \frac{\partial u_i}{\partial x_j} + \frac{\partial u_j}{\partial x_i} \quad (3.5)$$

Equations (3.4) and (3.5) forms six additional stresses, three normal stresses and three shear stresses, the extra turbulent stresses are called Reynolds stress it must be solved to close the problem. The quantity $\overline{\rho u'_i u'_j}$ is called the Reynolds-stress tensor denoted by

$$\tau_{ij} = -\overline{\rho u'_i u'_j} \quad (3.6)$$

Wilcox (2006).

3.1.1 Modeling the Reynolds Shear Stress

A common assumption for the form of τ_{ij} is the Boussinesq eddy-viscosity approximation. It assumes that the principal axes of the Reynolds stress tensor, τ_{ij} are aligned with the principal axes of the mean strain tensor, S_{ij} at all points in a turbulent flow Wilcox (2006). Thus

$$-\overline{\rho u'_i u'_j} = \mu_t \left(\frac{\partial U_i}{\partial x_j} + \frac{\partial U_j}{\partial x_i} \right) - \frac{2}{3} k \delta_{ij} \quad (3.7)$$

where μ_t is called the eddy viscosity and k is the turbulent viscosity ratio. This equation is not a good approximation for the determination of Reynolds shear stress. It cannot be applied to flows with sudden changes in mean strain rate, curved surfaces, or separated, and three- dimensional flows. The Boussinesq approximation assumes that the normal Reynolds stresses are equal and flow history effect are negligible, Wilcox (2006). Using the N-S equations to derive transport equations for Reynolds stresses shows that they are transported by the mean velocity as well as diffused molecular and eddy diffusion, the latter is usually negligible. In Cartesian coordinates, the transport equation for Reynolds stress τ_{ij} , is

$$\frac{\partial \tau_{ij}}{\partial t} + U_k \frac{\partial \tau_{ij}}{\partial x_k} = -\tau_{ij} \frac{\partial U_j}{\partial x_k} - \tau_{jk} \frac{\partial U_i}{\partial x_k} + \varepsilon_{ij} - \Pi_{ij} + \frac{\partial}{\partial x_k} \left(\mu_t \frac{\partial \tau_{ij}}{\partial x_k} + C_{ijk} \right) \quad (3.8)$$

Wilcox (2006), where the first term of the Equation (3.8) is the local time derivative, the second term is the convection of Reynolds stress by the mean flow. The first term on the right side is the turbulent diffusion, the second term is the molecular diffusion, ε_{ij} is the dissipation tensor, Π_{ij} is the pressure strain-correlation tensor, C_{ijk} is the turbulence transport tensor given by

$$\varepsilon_{ij} = 2\mu \frac{\partial u'_i}{\partial x_k} \frac{\partial u'_j}{\partial x_k} \quad (3.9)$$

$$\Pi_{ij} = \overline{p' \left(\frac{\partial u'_i}{\partial x_j} + \frac{\partial u'_j}{\partial x_i} \right)} \quad (3.10)$$

$$C_{ijk} = (\overline{\rho u'_i u'_j u'_k}) + (\overline{p' u'_i}) \delta_{jk} + (\overline{p' u'_j}) \delta_{ik} \quad (3.11)$$

where δ_{ij} is the Kronecker delta function Wilcox (2006). Although, Equation (3.8) provides an insight to the nature of the turbulent stress model, there are twenty-two unknown variables in six equations Versteeg and Malalasekera (2007). This is known as the closure problem.

3.2 The Boundary Layer Calculations

The boundary layers may be laminar, transitional, or turbulent. The boundary layer in a steady flow is laminar when the Reynolds stresses and other fluctuating components are zero. The SST-transition turbulence model was developed to capture the behaviour of flow in the boundary layer for all three possible conditions. The details of this model will be discussed in reversed order as the transition model was developed to be consistent with turbulence model. The details of how the laminar boundary layer was calculated before separation or transition will be given later in the section.

The SST-transition model is a four-equation model, based on coupling of the $k-\omega$ turbulence model, where k is the turbulent kinetic energy and ω is the specific dissipation rate defined as ε/k , ε is the dissipation rate. It contains two other transport equations, for intermittency, the proportion of the time the flow is turbulent, and a transition onset criteria in terms of momentum-thickness Reynolds number, Re_θ . The essential quantity to trigger the transition process is the vorticity or alternatively the strain rate Reynolds number, Menter et al. (2012). To the boundary layer approximation the strain rate Re is

$$Re_v = \frac{\rho y^2}{\mu} \left| \frac{\partial u}{\partial y} \right| = \frac{\rho y^2}{\mu} S \quad (3.12)$$

where y is the distance from the nearest wall, S is the shear strain rate. The vorticity Re is a local property and can be computed at each grid point in an unstructured, N-S code, Menter et al. (2012). The model relates the local momentum thickness, Re_{θ_t} , based on Equation (3.13) to the

critical value Re_{θ_c} , and switches on the intermittency production when Re_{θ} is larger than local critical value.

$$Re_{\theta} = (\max(Re_v))/2.193 \quad (3.13)$$

where 2.193 is a constant determined from the Blasius boundary layer for zero pressure gradient flow over a flat plate. Three critical correlations were claimed to be proprietary and hence not specified. They are for Re_{θ_t} , Re_{θ_c} and F_{length} , ANSYS, (2011). Re_{θ_t} is a function of the local Tu , and the Thwaites' pressure gradient parameter, λ_{θ} . λ_{θ} is $(\theta^2/\nu)dU/ds$ where dU/ds is the velocity gradient in the streamwise direction, and ν , is the kinematic viscosity which is the ratio of the dynamic viscosity and the density. θ is the momentum thickness, which represents a thickness of the freestream flow that has a momentum equal to the momentum deficit in the boundary layer. F_{length} is the empirical correlation that controls the length of the transition region.

$$Re_{\theta_t} = f(Tu, \lambda); F_{length} = f(\widehat{Re}_{\theta_t}); Re_{\theta_c} = f(\widehat{Re}_{\theta_t}) \quad (3.14)$$

\widehat{Re}_{θ_t} is the local transition onset momentum thickness Re , and Re_{θ_c} is the critical Re where intermittency begins. Physically this means the first appearance of disturbances that will normally grow and cause transition. Since the introduction of the original model, different groups have made improvements. A naming convention was introduced in Menter (2006) in order to keep track of the various model versions. The fundamental model framework transport equation was called the $\gamma - Re_{\theta}$ transition model, where γ is the intermittency. The four equations for the transition model are for k , ω , γ and Re_{θ} .

3.2.1 Turbulence Calculation

The $k - \omega$ turbulence model defined earlier is part of the SST-transition model. The default model constants were not modified for the present calculations. The advantage of using this model is the automatic wall treatment for low Re computations is more accurate and more robust than other turbulence model, ANSYS (2011). One of the limitations is the sensitivity of the solutions to values of k and ω outside the shear layer i.e. freestream sensitivity ANSYS (2011).

It can have significant effects on the solution of the boundary layer. The two equation model is:

$$\frac{\partial}{\partial t}(\rho k) + \frac{\partial}{\partial x_i}(\rho k U_i) = \frac{\partial}{\partial x_j} \left(\Gamma_k \frac{\partial k}{\partial x_j} \right) + G_k - Y_k + S_k \quad (3.15)$$

and

$$\frac{\partial}{\partial t}(\rho \omega) + \frac{\partial}{\partial x_i}(\rho \omega U_i) = \frac{\partial}{\partial x_j} \left(\Gamma_\omega \frac{\partial \omega}{\partial x_j} \right) + G_\omega - Y_\omega + S_\omega \quad (3.16)$$

G_k in equation (3.30) represents the generation of turbulence kinetic energy due to mean velocity gradients, while G_ω represents the generation of ω . Γ_k and Γ_ω represent the effective diffusivity of k and ω , respectively. Y_k and Y_ω are the effective diffusivity of k and ω respectively, due to turbulence. All of the above terms are calculated as described below. S_k and S_ω are user defined source terms, ANSYS (2011), which were not used in the present calculations. The effective diffusivities for the $k - \omega$ model are given by

$$\Gamma_k = \mu + \frac{\mu_t}{\sigma_k} \quad (3.17)$$

$$\Gamma_\omega = \mu + \frac{\mu_t}{\sigma_\omega} \quad (3.18)$$

where, σ_k and σ_ω are the turbulent Prandtl numbers for k and ω , respectively. The μ_t is computed by combining k and ω as follows.

$$\mu_t = \alpha^* \frac{\rho k}{\omega} \quad (3.19)$$

where α^* is a coefficient that is used to damp the turbulent viscosity i.e damp the dissipation of k and diffusion of ω in the viscous sublayer. This was done for low Re correction. The high Re form of the $k - \omega$ has $\alpha^* = \alpha_\infty^* = 1$, where $\alpha^* = f(\alpha_\infty^*)$, the default value of α_∞^* was changed from 1 to 0.5 to account for the low Re correction, this was achieved by trial and error ANSYS (2011). In order to ensure accuracy in calculating the laminar and turbulent boundary layer, y^+ was set as one. y^+ is a non-dimensional distance from the wall to the first node. The value one was recommended in the FLUENT manual. This condition was set to ensure that the properties of the fluid computed at the first node and the wall conditions were consistent, the details will be discussed in 3.2.4.

3.2.2 Transition Model

The transition on the boundary layer is determined by two transport equations, one for intermittency, which is for the proportion of time that the flow is not laminar and transition onset momentum thickness Reynolds number, $\widehat{Re}_{\theta t}$, as observed in experiments, given by Equations (3.35) and (3.42) respectively. The default constants were retained for intermittency, γ , while those for $\widehat{Re}_{\theta t}$ were modified. The model is used to determine the onset of transition and length of transition.

The transport equation for intermittency, γ is:

$$\frac{\partial(\rho\gamma)}{\partial t} + \frac{\partial(\rho U_j \gamma)}{\partial x_j} = P_\gamma - E_\gamma + \frac{\partial}{\partial x_j} \left[\left(\mu + \frac{\mu_t}{\sigma_f} \right) \frac{\partial \gamma}{\partial x_j} \right] \quad (3.20)$$

The transition sources are defined as:

$$P_\gamma = F_{length} c_{a1} \rho S [\gamma F_{onset}]^{0.5} (1 - c_{e1} \gamma) \quad (3.21)$$

where S is the strain rate magnitude, F_{length} is an empirical correlation that controls the length of the transition region and F_{onset} determines when the production of intermittency is activated.

The boundary condition for γ at a wall is zero normal flux while at inlet the value of γ is equal to

1. The transition onset is controlled by the following functions:

$$F_{onset1} = \frac{Re_v}{2.193 Re_{\theta c}} \quad (3.22)$$

$$F_{onset2} = \min (\max(F_{onset1}, F_{onset1}^4), 2.0) \quad (3.23)$$

$$F_{onset3} = \max \left(1 - \left(\frac{R_T}{2.5} \right)^3, 0 \right) \quad (3.24)$$

$$F_{onset} = \max(F_{onset2} - F_{onset3}, 0) \quad (3.25)$$

$Re_{\theta c}$ is the critical Re where the intermittency first starts to increase in the boundary layer. This occurs upstream of the transition Re number $\widehat{Re}_{\theta t}$, local transition onset momentum thickness Reynolds number obtained from an empirical correlation.

The constants in the intermittency equation are

$$c_{e1} = 1.0; \quad c_{a1} = 2.0; \quad c_{e2} = 50; \quad c_{a2} = 0.06; \quad \sigma_f = 1.0 \quad (3.26)$$

as given in ANSYS (2011). The second equation for transition is the transport equation for

momentum thickness number $\widehat{Re}_{\theta t}$ can be written as

$$\frac{\partial(\rho \widehat{Re}_{\theta t})}{\partial t} + \frac{\partial(\rho U_j \widehat{Re}_{\theta t})}{\partial x_j} = P_{\theta t} + \frac{\partial}{\partial x_j} \left[\sigma_{\theta t} (\mu + \mu_t) \frac{\partial \widehat{Re}_{\theta t}}{\partial x_j} \right] \quad (3.27)$$

The source term $P_{\theta t}$ is designed to force the transported scalar $\widehat{Re}_{\theta t}$ to match the local value of $Re_{\theta t} = f(Tu, \lambda)$. It is defined as

$$P_{\theta t} = c_{\theta t} \frac{\rho}{t} (Re_{\theta t} - \widehat{Re}_{\theta t}) (1.0 - F_{\theta t}) \quad (3.28)$$

where

$$t = \frac{500\mu}{\rho U^2} \quad (3.29)$$

The time scale t was determined using dimensional analysis with main criteria being that it had to scale with convective and diffusive terms in the transport equation. $F_{\theta t}$ is the blending function used to turn off the source term in the boundary layer, its value is 1 in the boundary layer and zero in the freestream. $F_{\theta t}$ is defined in the following equation.

$$F_{\theta t} = \min \left(\max \left(F_{wake} \cdot e^{-\left(\frac{y}{\delta}\right)^4}, 1.0 - \left(\frac{\gamma - 1/c_{e2}}{1.0 - 1/c_{e2}} \right)^2 \right), 1.0 \right) \quad (3.30)$$

$$\delta = \frac{50\Omega y}{U} \cdot \delta_{BL}; \quad \delta_{BL} = \frac{15}{2} \theta_{BL}; \quad \theta_{BL} = \frac{\widehat{Re}_{\theta t} \mu}{\rho U} \quad (3.31)$$

$$F_{wake} = e^{-\left(\frac{Re_{\omega}}{1E+5}\right)^2}; \quad Re_{\omega} = \frac{\rho \omega y^2}{\mu} \quad (3.32)$$

F_{wake} ensures that the blending functions are not active in the wake regions i.e. downstream of an airfoil. The default model constants for the Reynolds number momentum thickness equations are

$$c_{\theta t} = 0.03; \quad \sigma_{\theta t} = 2.0 \quad (3.33)$$

The boundary condition for $\widehat{Re}_{\theta t}$ at the wall is zero flux. However, the boundary conditions for $\widehat{Re}_{\theta t}$ at inlet should be calculated from the empirical correlation based on the inlet Tu .

3.2.3 Laminar Boundary Layer Calculation

The intermittency γ varies between 0 (laminar) and 1 (turbulent), and can vary through the boundary layer. The production term in Equation (3.21) depends on the $Re_{\theta c}$ and F_{length} . $Re_{\theta c}$ determines the transition onset location, where γ first starts to increase in the boundary layer. The F_{onset} function uses $Re_{\theta c}$ and is designed to switch from 0 in a laminar boundary layer to 1 in the turbulent boundary layer. This implies that the turbulence model is turned off by the use of intermittency until the location of onset of transition, thereby producing a laminar region upstream of the transition onset. A sufficient refinement was necessary in order to capture the flow features present in laminar boundary layer. This was achieved by having enough point in the laminar boundary layer, the cell spacing at the first inner cell was fixed at 2.5×10^{-4} m. Geometric stretching option technique was applied for the calculations both in the streamwise direction and for the grid distribution normal to the blade. In the streamwise direction, 1.03 was specified as the geometric growth rate from the wall of the blade. It was discovered that refining the mesh more than necessary affected convergence e.g. more than 300 nodes for the grid distribution normal to the blade.

3.2.4 Laminar and Transitional Boundary Layers

ANSYS (2011) recommends using y^+ of approximately one, where y is the distance of the first node from the wall. This restriction ensures consistency between the velocities computed at the first node and the wall conditions. The reason is that the no-slip condition means that the

streamwise velocity is linear in distance from the wall, but that linearity holds only for vanishingly small distances for these small distances, $u^+ = y^+$ where u^+ is given by

$$u^+ = \frac{U}{u_\tau}, u_\tau = \left(\frac{\tau_{wall}}{\rho} \right)^{1/2} \quad (3.34)$$

u^+ is a non-dimensional velocity, U is mean velocity at a distance y from the wall, u_τ is friction velocity and τ_{wall} is the wall shear stress.

3.3 Coupling the Transition Model and SST Transport Equations

Menter et al. (2012) described the coupling of the transition model with the SST-turbulence model by modification of the k -equation, Equation (3.15) as follows. The transport equation for SST k - ω model is

$$\frac{\partial}{\partial t}(\rho k) + \frac{\partial}{\partial x_i}(\rho k u_i) = \frac{\partial}{\partial x_i} \left(\Gamma_k \frac{\partial k}{\partial x_j} \right) + G_k^* - Y_k^* + S_k \quad (3.35)$$

$$G_k^* = \gamma_{eff} G_k \quad (3.36)$$

$$Y_k^* = \min(\max(\gamma_{eff}, 0.1), 1.0) Y_k$$

where G_k and Y_k are the original production and destruction terms for the SST model. The production term in the ω equation was not modified.

Chapter 4: The Calculation of Circular Arc Airfoil Performance

4.1 Introduction

Blade element theory requires the aerodynamic properties of airfoils comprising the blade sections as input. These properties are C_L and C_D . In this chapter, the aerodynamics properties of two CA airfoils were studied by comparing calculation to the available experiments. The first experiment, performed by Tezuka et al. (2008), was used to set the constants for the transition model. This experiment was used because it gives the separation and reattachment points of the LSB. The same constants were used for the computation of the experiments of Bruining (1979). The numerical solution was able to reasonably match the experiment of the surface pressure distribution of a CA airfoil of 4% camber and the calculation of the L and D coefficient of 10% camber CA2 airfoil at $Re = 62,000$ and $100,000$ respectively.

All calculations used ANSYS FLUENT and the meshes were generated in the ANSYS mesh generator, ICEM. A code was written in Matlab to check the accuracy of the L and D calculated in FLUENT from the force distribution on the blades.

4.1.1 Calculating C_L and C_D

Figure 4.1 shows the forces on the blade. The resultants of the pressure and shear forces can be split into two components; one in the direction normal to the flow which is L and the second in the direction of the flow which is the D .

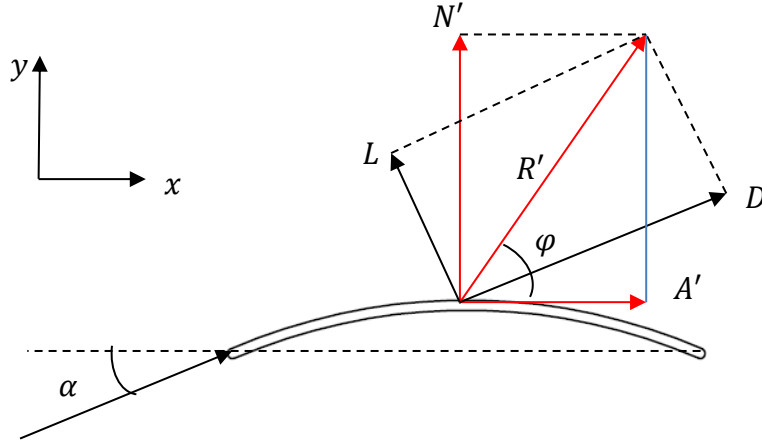


Figure 4.1: Pressure and viscous forces acting on CA and the resultant and lift forces.

where R' is the resultant force, the L , is the lift N' is the force normal to the direction of the chord while A' is the force that is tangential to the direction of the chord. To get the forces N' and A' requires the integration of the static pressure and wall shear stress, τ_{wall} over the aerofoil. The equations are:

$$N' = \int P_{static} dx + \int \tau_{wall} dy \quad (4.1)$$

$$A' = \int P_{static} dy + \int \tau_{wall} dx \quad (4.2)$$

L and D are then determined by

$$L = N' \cos(\alpha) - A' \sin(\alpha) \quad (4.3)$$

$$D = N' \sin(\alpha) + A' \cos(\alpha) \quad (4.4)$$

The first part of equation (4.1) only was solved by numerical integration using the Trapezoidal Rule since there was no information of the τ_{wall} for the experiment of Tezuka et al. (2008). The effect of τ_{wall} in equation (4.1) is usually very small. The reason for using Trapezoidal rule is

because of non-constant spacing between the values for experiment and calculation. A Matlab code was written for the numerical integration.

4.2 Calculation Procedure

4.2.1 Circular Arc Airfoil CA1

The first calculation considered was the surface pressure distribution measurements of Tezuka et al. (2008), the L and D were not measured. The pressure coefficient is defined as

$$C_p = \frac{P - P_0}{\frac{1}{2}\rho U_\infty^2} \quad (4.5)$$

where P_0 is the reference pressure. The airfoil properties are $h/c = 4\%$, $\Delta t = 0.001\text{m}$ and $c = 0.1\text{m}$. The experiment was performed at $0^\circ \leq \alpha \leq 12^\circ$ and $Re = 62,000$.

Figure 4.2 shows the computational grid for the isolated airfoil of Tezuka et al. (2008). The circular arc CA airfoil geometry is significantly different from a conventional airfoil, therefore in order to capture the geometry effectively an O-type grid was used around the CA. The geometry is symmetrical about the mid-chord. The most important factor for using the O-type grid close to the airfoil is to be able to ensure high quality boundary layer calculation. The domain is rectangular in shape. The minimum orthogonal distance from the blade is $2.5 \times 10^{-4}\text{m}$ to the first node along the entire surface of the CA. The stream wise spacing from the LE to TE is 150 nodes along the blade surface with the maximum values at mid-chord. The LE and the TE are divided into 30 points.

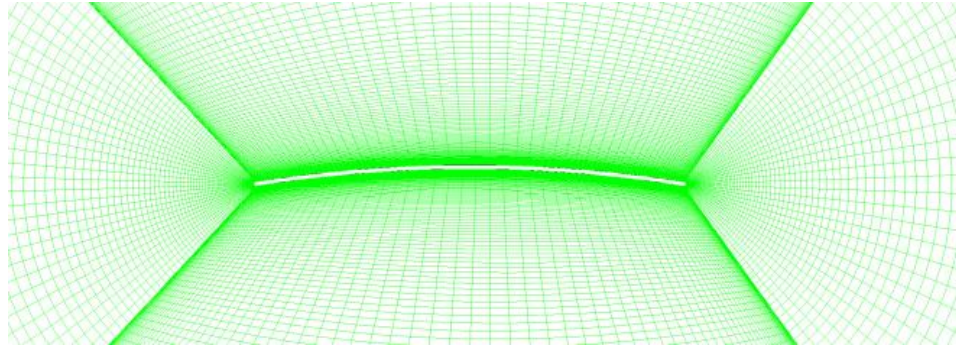


Figure 4.2: A view of part of the computational mesh for the circular arc airfoil

The upstream and downstream lengths of the computational domain were $10c$ from the LE and $20c$ from the TE, respectively. The bottom and top boundaries were set at $\pm 10c$. This computational mesh will be called Mesh 1. The constant velocity at inlet matched the value used in the experiment. The Tu was specified as 0.13% from the experiment. The outlet boundary is set as pressure outlet, and the gauge pressure is set to zero. The upper and lower boundary is set as velocity inlet, as the boundary is far from blade. Figure 4.3 show the grid independence test performed for $\alpha = 4^\circ$, the calculations of C_p on the pressure side were compared to see if there were significant variations. Mesh 2 was used as a reference for the mesh independence test, it has 92,109 elements and 92,524 nodes. In order to establish the mesh independence the grid elements of mesh2 were multiplied with a factor of 3.5 to produce Mesh 3 and then reduced by a factor of about 0.75 to produce mesh1.

The domain test was carried out by extending the upstream length and downstream length to $15c$ and $30c$ respectively with the boundary conditions remaining unchanged. The maximum deviation of the C_L was 0.21 % which was considered insignificant. To establish iterative

convergence, the simulation was allowed to run for twice the converged number of iterations based on scaled residual set as 10^{-5} , the scaled residual is the ratios of the correction to the primitive variables divided by the values of the primitive variables for any given iteration. The difference between the converged solutions for C_L was 0.063% when the computational domain and the boundary conditions remained unchanged. These results show that the solution is independent of the number of mesh points in the grid and that they converged satisfactorily. The mesh 2 was used for the remaining calculations.

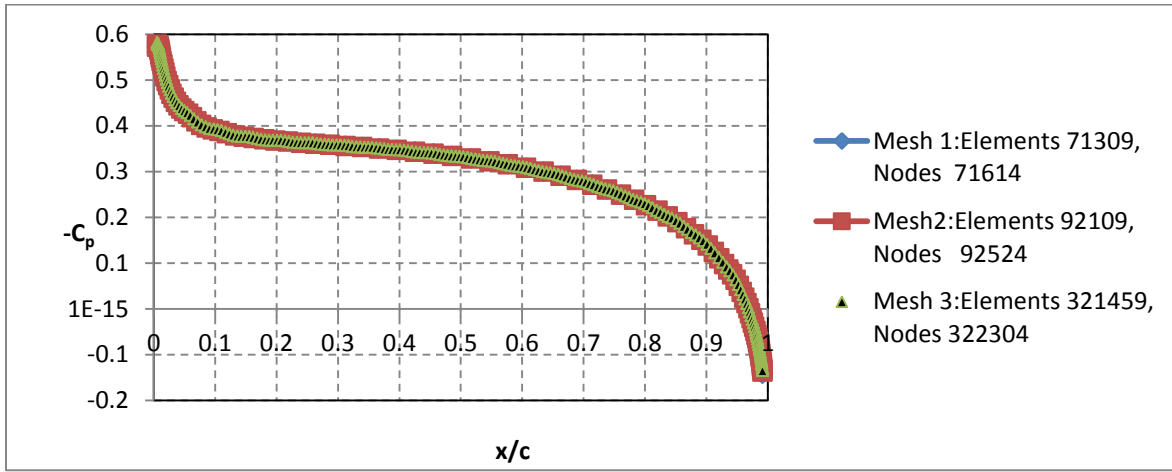


Figure 4.3: Mesh-independence test

The model constants for the transport equation from equation (3.42) and (3.43) are $c_{\theta t}$ and $\sigma_{\theta t}$, where $c_{\theta t}$ controls the magnitude of the source term and $\sigma_{\theta t}$ controls the diffusion coefficient. The default values of $c_{\theta t}$ and $\sigma_{\theta t}$ are 0.03 and 2.0 respectively. The lag between the local value of $\widehat{Re_{\theta t}}$ in the boundary layer and that in the free stream can be controlled by the diffusion coefficient $\sigma_{\theta t}$. The larger the value of $\sigma_{\theta t}$, the less sensitive the transition model to flow history. For example the default value $\sigma_{\theta t}$ was obtained from a flat plate experiment, where the free

stream Tu and pressure gradient were rapidly changing and flow history effects are believed to be significant, Menter (2006). According to Abu-Ghannam and Shaw (1980) this is an important effect since the onset of transition is primarily affected by the history of pressure gradient.

In order to get the good agreement with the measured pressure distribution, the model constants were changed through trial and error. The best overall value of $\sigma_{\theta t}$ was 50% larger than the default value, whereas that for $c_{\theta t}$ was 33% lower, as shown in table 4.1. As mentioned earlier the default constants were obtained from experiments on boundary layer transition on a flat plate.

Table 4.1: Comparing the default and changed values for $\sigma_{\theta t}$ and $c_{\theta t}$

Parameter	$\sigma_{\theta t}$	$c_{\theta t}$
Default	2	0.03
Current value	3	0.02

The calculations in this thesis cover $\alpha = 2^\circ$ and above. The results showed the formation of LSB confirmed by examining the turbulent kinetic energy contours and the streamlines as shown by the example in Figure 4.4. It was verified that after the stagnation point the flow was laminar on the suction part of the airfoil and transition did not occur before the boundary layer separated. The stagnation streamlines show that the stagnation moved to the pressure side from the leading edge, this is shown in Figure 4.4. The separation and reattachment points were observed using the C_f plot. After the separation the flow transitions to turbulence and usually reattaches forming a bubble.

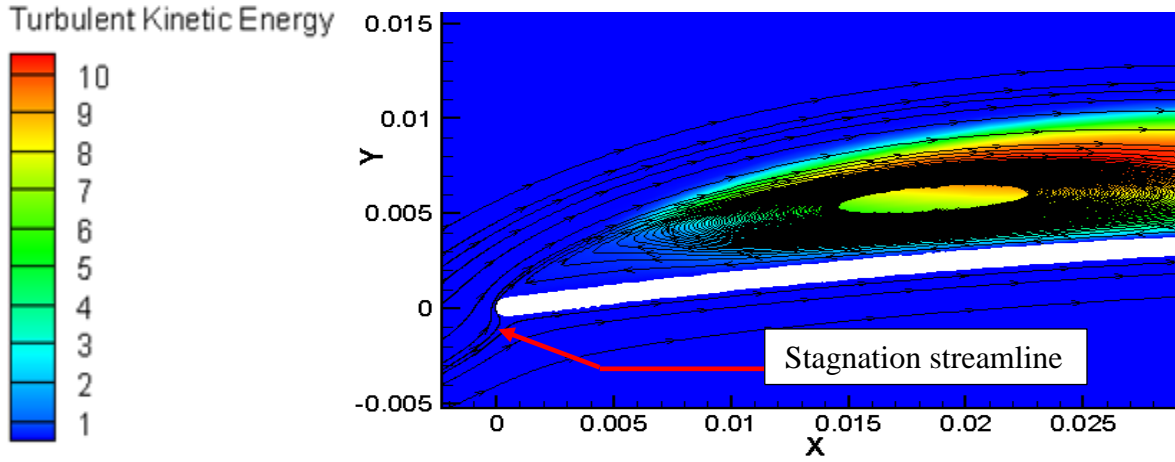


Figure 4.4: Streamlines and Turbulence Kinetic Energy (k) (m^2/s^2) contours of the current simulation for CA1, for $\alpha = 7^\circ$, $U_\infty = 9.06\text{m/s}$, Tezuka et al. (2008)

The separated shear layer which is formed on the suction side of the airfoil curves back to the airfoil surface to form a shallow separation bubble. The details will be examined when considering the wall shear stress plots. Table 4.2 shows the C_P contribution which can be approximated as the C_L , the C_D cannot be calculated because there is no shear stress information available from the experiment. The C_P contribution was calculated for $\alpha = 3^\circ, 7^\circ$ and 10° .

A Matlab code was written to determine the contribution to C_L from C_P calculated by FLUENT and measured in the experiment. The primary purpose of calculating these parameters with Matlab code was to confirm that the output from FLUENT was correctly determined and this was done for all the calculations. Subsequently, the C_L calculated in FLUENT was compared with the output of the Matlab code, as shown the results compare reasonably with the values

determined by the present author from the experiment. Generally the FLUENT output were consistent with the Matlab results.

Table 4.2 Comparing L and D directly from FLUENT and post processed using Matlab for of CA1 of Tezuka et al. (2008)

α (degrees)	C_L (FLUENT calculated)	C_L (FLUENT Pressure contribution, Matlab)	C_L (Experiment Pressure contribution, Matlab)
3	0.712	0.712	0.669
7	1.056	1.055	0.997
10	1.038	1.0471	1.027

The C_L and C_D calculated by FLUENT is shown in table 4.3; as discussed earlier there is no information on C_L and C_D from the experiment. C_L was only compared with the pressure contribution. From the table the C_D increased significantly, almost double from $\alpha = 7^\circ$ to $\alpha = 10^\circ$.

Table 4.3: Computed C_L and C_D at $\alpha = 2^\circ, 3^\circ, 7^\circ$ and 10° of CA1 of Tezuka et al. (2008)

α	C_L	C_D
2	0.547	0.0171
3	0.712	0.0246
7	1.056	0.0788
10	1.038	0.1494

The computed and measured pressure distribution for the CA of 4% camber of Tezuka et al. (2008), are compared at $\alpha = 2^\circ, 3^\circ, 7^\circ$ and 10° respectively in Figure 4.5a-d. The results indicate a reasonable agreement with the experiment. However, at about 10% of the chord the upper part of the CA indicate discrepancy between the experiment and the calculated C_p . This is as a result of under-prediction of the LSB caused by early transition. The LSB prediction are reviewed below by examining the wall shear stress and streamlines for $\alpha = 3^\circ$ and $\alpha = 7^\circ$.

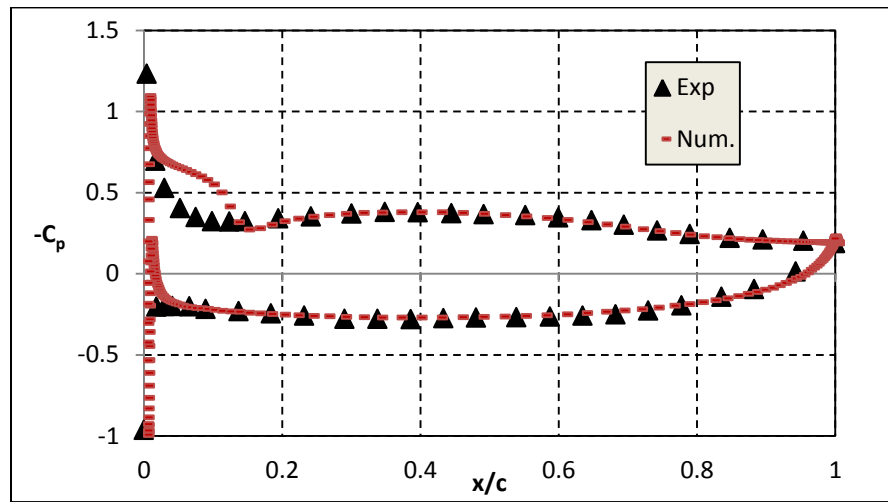


Figure 4.5a: Computed and measured pressures distribution of a 4% cambered CA1 airfoil Tezuka et al. (2008) at $\alpha = 2^\circ$

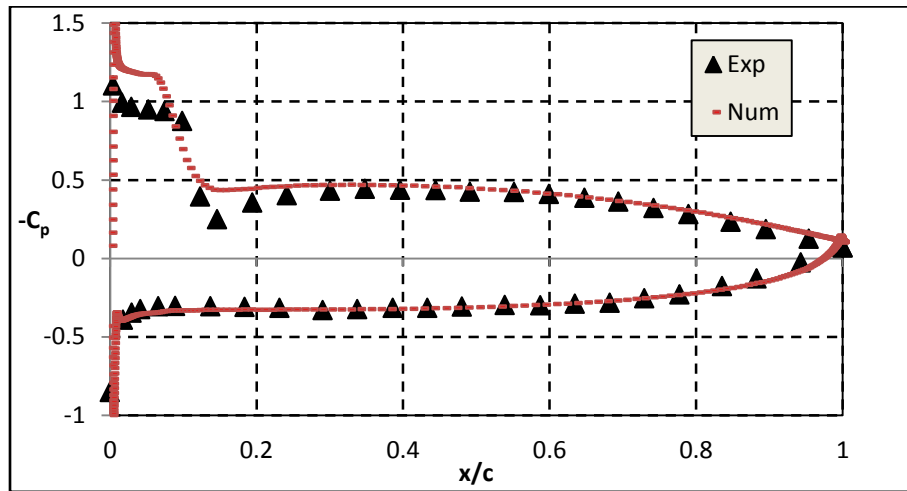


Figure 4.5b: Computed and measured pressures distribution of a 4% cambered CA1 airfoil
Tezuka et al. (2008) at $\alpha = 3^\circ$

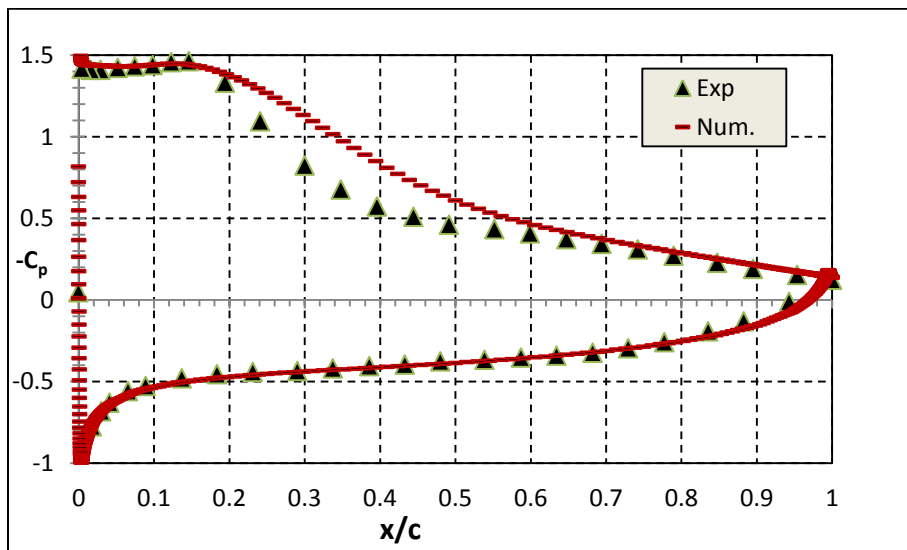


Figure 4.5c: Computed and measured pressures distribution of a 4% cambered CA1 airfoil
Tezuka et al. (2008) at $\alpha = 7^\circ$

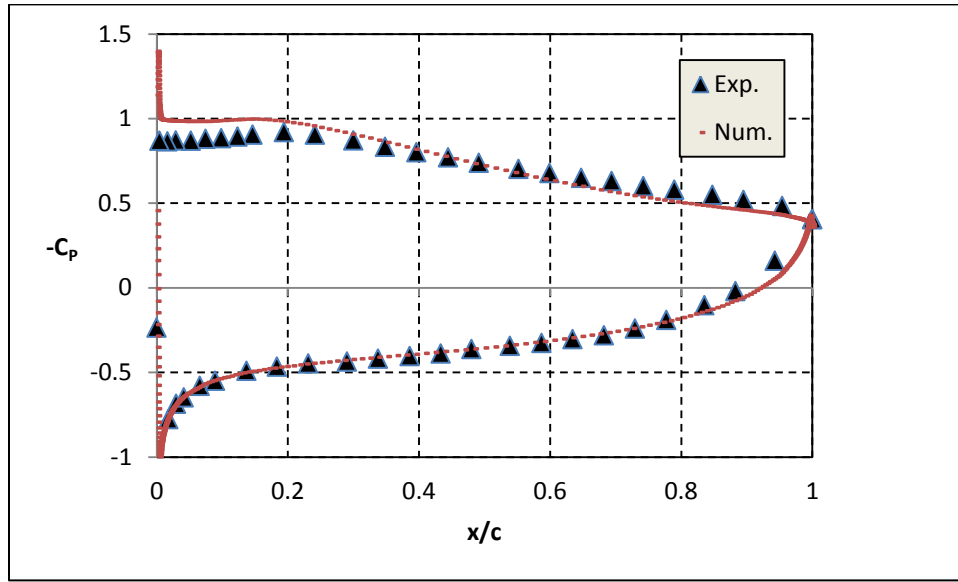


Figure 4.5d: Computed and measured pressures distribution of a 4% cambered CA1 airfoil Tezuka et al. (2008) at $\alpha = 10^\circ$

Compared to Figure 2.9 and 2.10 which are previous investigation of the ability of the SST-transition to predict separation, the results in Figures 4.5a-d can be considered good. In order to study the LSB, the streamlines for $\alpha = 3^\circ$ and $\alpha = 7^\circ$ were studied. Figure 4.6a and 4.6b shows computed streamlines at $\alpha = 3^\circ$ and the wall shear stress. Tezuka et al. (2008) made flow visualizations on the upper surface of the airfoil, and observed that the reattachment point was 15% of the chord. In the computations adverse pressure gradient caused separation very close to the LE, and the flow reattached at 13% of the chord, which is comparable to the oil visualization result of Tezuka et al. (2008).

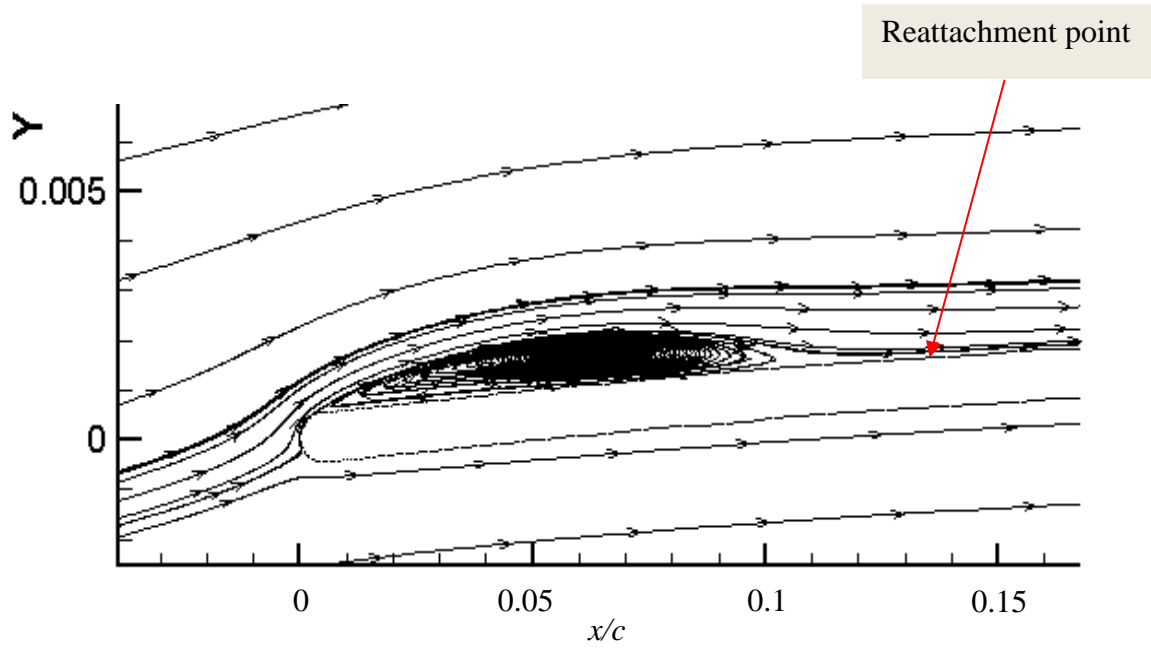


Figure 4.6a: Computed streamline for 4% cambered CA airfoil, $\alpha = 3^\circ$, Tezuka et al. (2008)

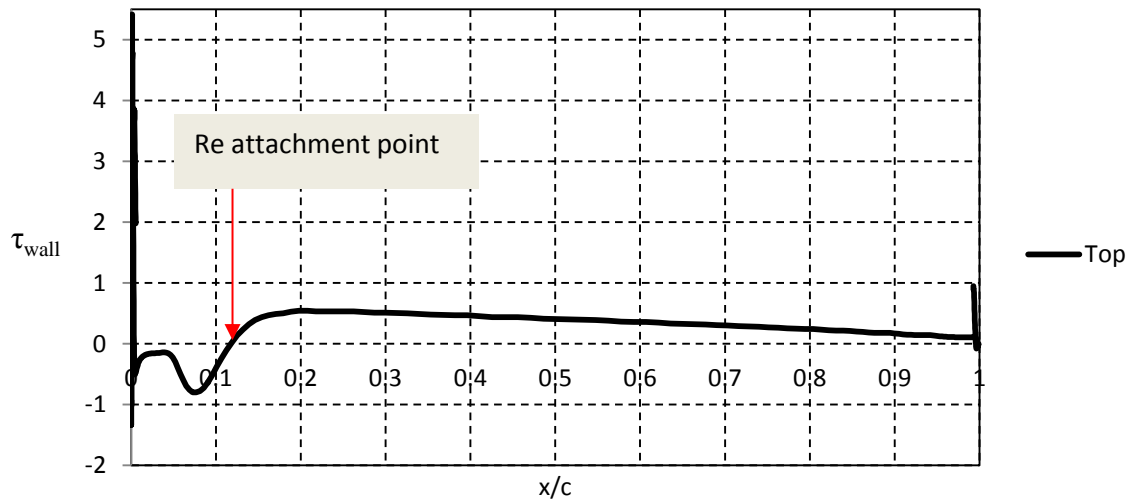


Figure 4.6b: Computed wall shear stress for a 4% cambered CA1 airfoil, $\alpha = 3^\circ$, Tezuka et al. (2008)

Figure 4.7a and 4.7b shows streamline and the wall shear stress for $\alpha = 7^\circ$. The reattachment occurs at 42% of the chord which is comparable to the flow visualisation results of Tezuka et al.

(2008) at 43% of the chord. Figure 4.7c shows the wall shear stress for $\alpha = 10^\circ$ which is an indication of separation with reattachment at 99% of the curve possibly. It is to be noted that in the oil visualization of Tezuka et al. (2008), there is no re-attachment. The results in the calculations show that the SST-transition model with adjusted model constants is able to predict the region of separation and reattachment reasonably well.

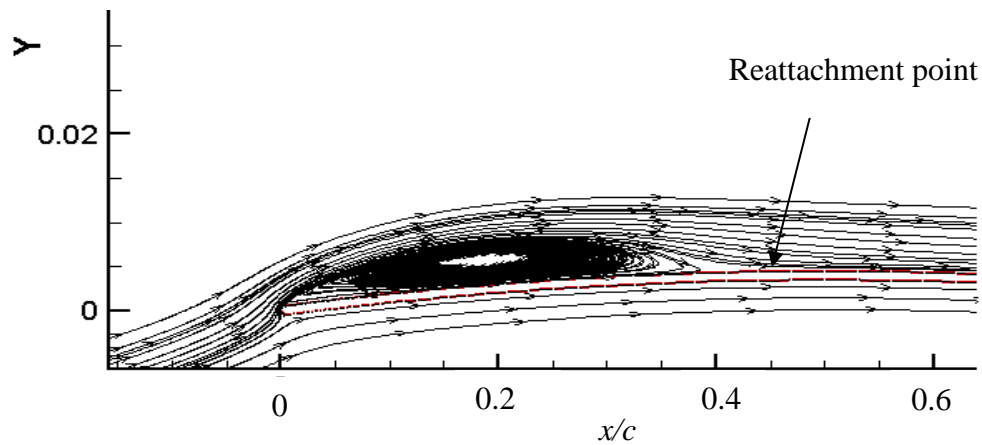


Figure 4.7a: Computed streamline for a 4% cambered CA1 airfoil, $\alpha = 7^\circ$, Tezuka et al. (2008)

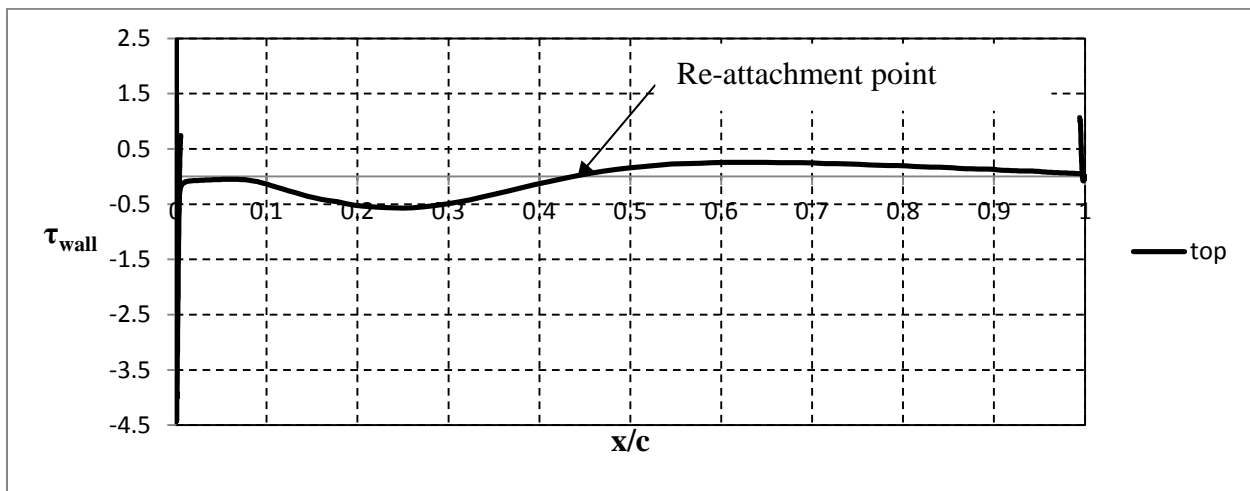


Figure 4.7b: Wall shear stress for a 4% cambered CA1 airfoil, $\alpha = 7^\circ$, Tezuka et al. (2008)

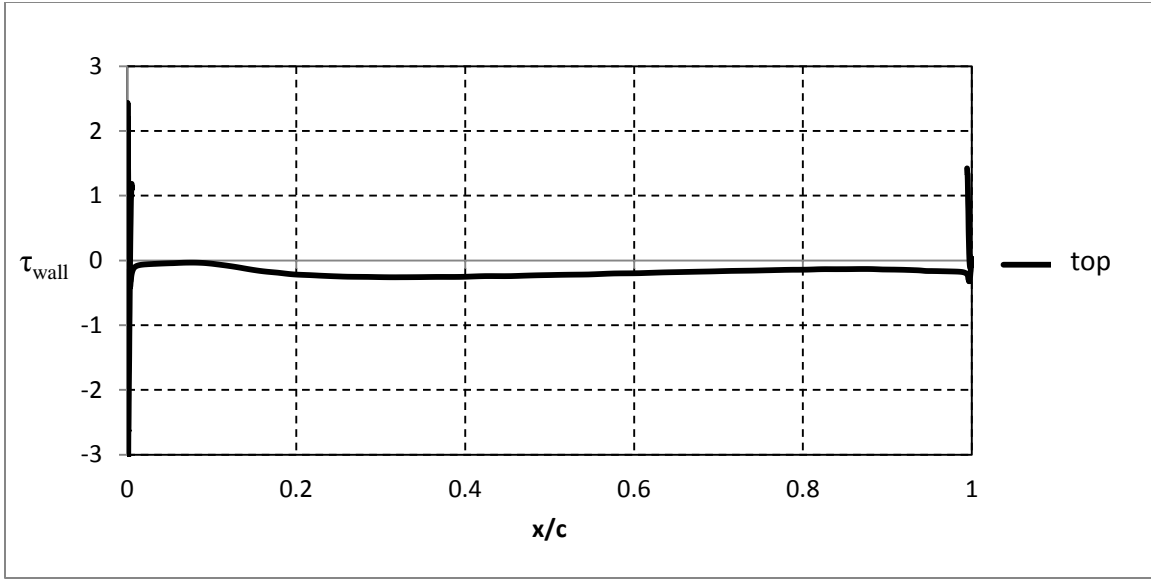


Figure 4.7c: Wall shear stress for a 4% cambered CA1 airfoil, $\alpha = 10^\circ$ Tezuka et al. (2008)

4.2.2 Circular Arc Airfoil CA2

CA2 was used in Bruining (1979) experiment. The model properties are as follows; 10% camber, $c = 0.15\text{m}$ and $\Delta t = 0.003\text{m}$ as shown in Figure 4.8. Bruining (1979) tested CA2 at Re of 60,000, 100,000, 200,000 and 350,000. C_L and C_D were determined in a wind tunnel with a very low free stream Tu of 0.02%. The C_L and C_D were calculated for CA2 with $Re = 100,000$ compared to CA1 which is 62,000. The purpose of this was to apply the SST-transition model to a CA with different properties and compare the calculation with the experimental C_L and C_D . This is necessary to show the consistency of the capability of the model in predicting the flow on CAs.

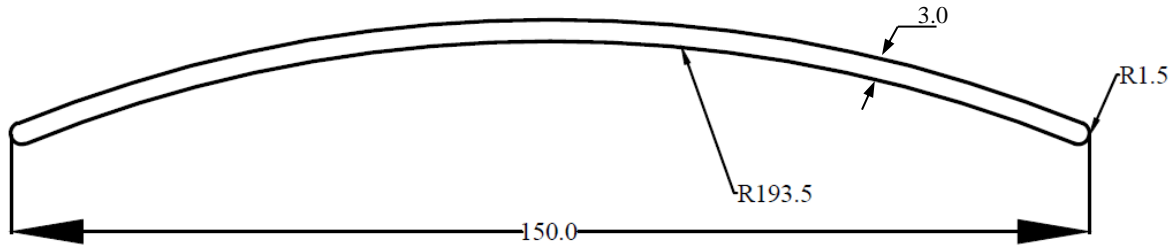


Figure 4.8: CA2 airfoil, dimensions in mm, adapted from Bruining, (1979)

Similar to CA1, an O-type grid was generated for this problem in order to capture the shape of the circular arc airfoil, the domain used in this calculation is $10c$ upstream of the LE and $20c$ downstream of the TE, with the upper and lower boundaries at $\pm 10c$. The mesh was generated in ICEM, Figure 4.9 shows a part of the unstructured mesh.

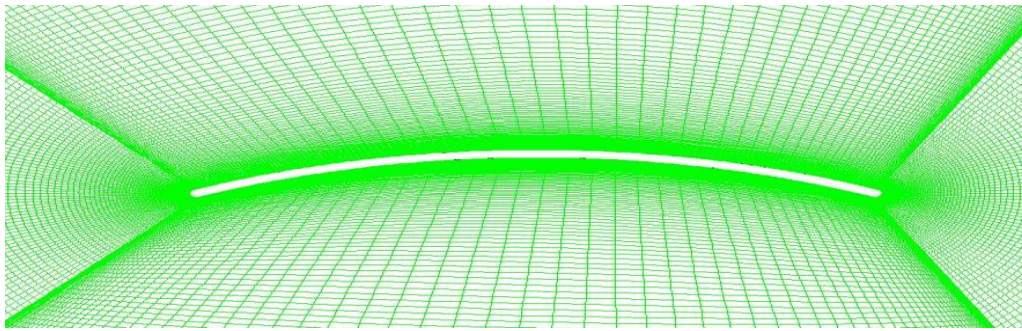


Figure 4.9: Part of unstructured mesh generated in ICEM for Bruining's (1979) experiment

The boundaries are set similar to the calculation for CA1, with the boundary conditions set as velocity at inlet. The upper and lower boundaries were also velocity inlet while the outlet boundary was pressure outlet, this required specification of the gauge pressure at outlet boundary which was set as atmospheric pressure. The calculation was performed with the SST-transition

model using the same modified constants as for the previous calculations. The mesh independence was carried out for the CA2, Mesh1 had total of 90,722 nodes, with equivalent 90,056 elements. Since the mesh was already dense, the number was halved to test whether the solution is dependent on the mesh size. The domain size remained unchanged. However as seen in Figure 4.10 there is no significant difference in the pressure side plot of the C_p for the two sizes of mesh. The deviation between the L of Mesh 1 and Mesh 2 is 0.4%. Mesh 1 was used for the remaining calculations. The convergence criteria were set as a scaled residual of 10^{-5} for all the parameters and this was achieved in the calculation. The iterative convergence was done for the meshes. It was found that the percentage change in the L result was less than 0.5%.

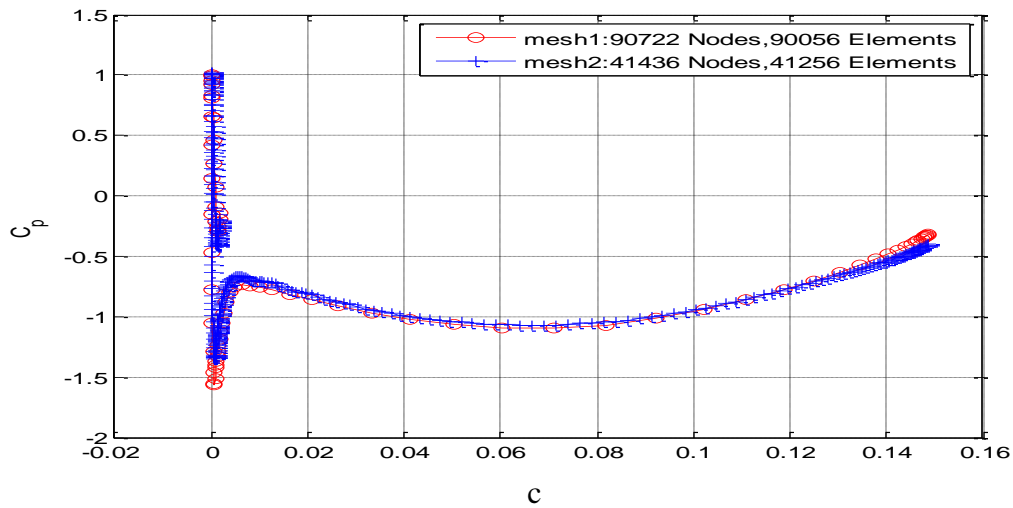


Figure 4.10: Mesh independence test for CA2 of Bruining, (1979).

Bruining (1979) measured only C_L and C_D , the pressure distribution were not measured. Figure 4.11 shows the measured and calculated C_L in the range of $0^\circ < \alpha < 10^\circ$. As clearly shown the measurements are over-predicted at $\alpha = 0^\circ$. However, at higher α the calculation is able to

reproduce the C_L reasonably well. Figure 4.12 shows the computed and measured C_D and α . The calculation over-predicted the drag coefficient. The problem of over-prediction of C_D is most likely caused by early transition and the resulting turbulent wall shear stress which would be higher than the laminar ones.

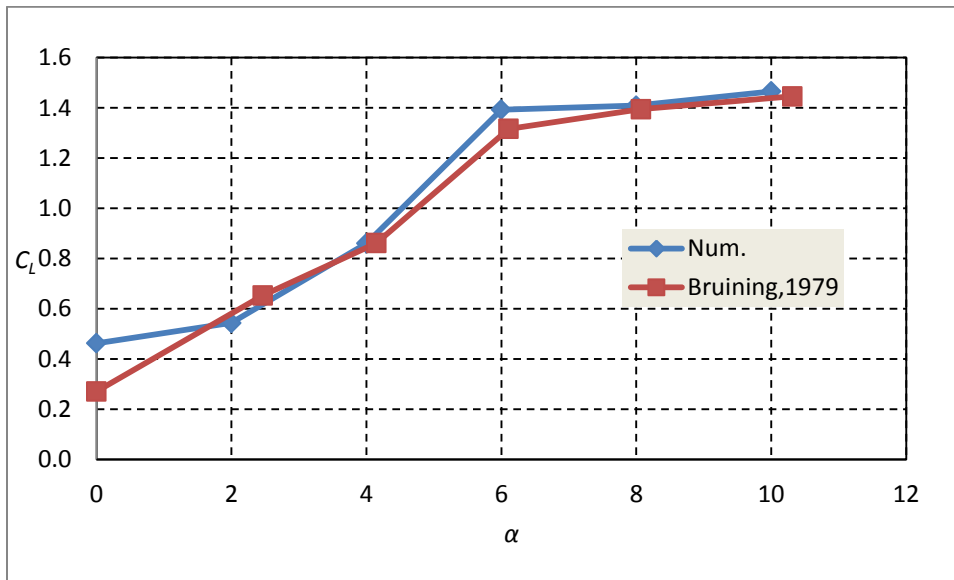


Figure 4.11: Computed and measured C_L for the experiment of Bruining (1979)

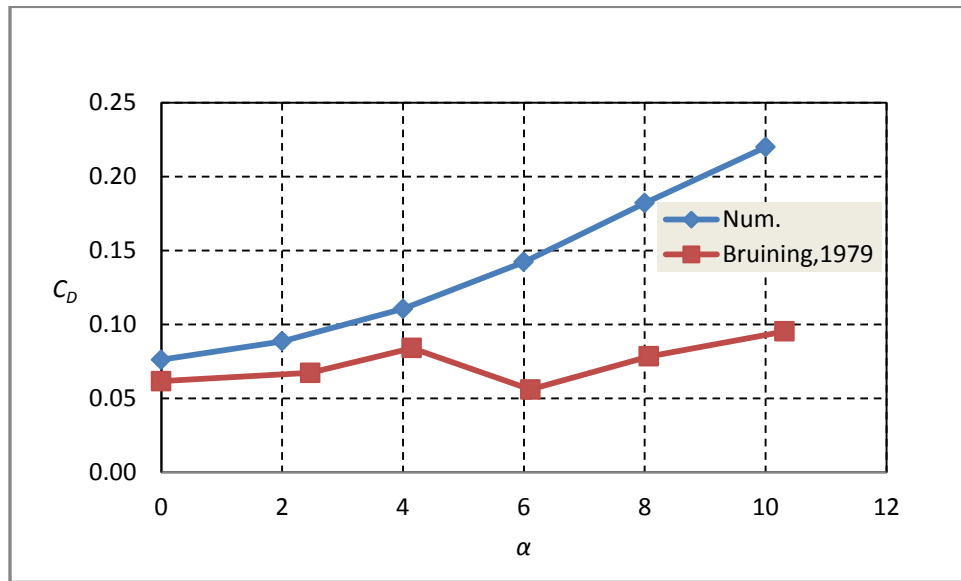


Figure 4.12: Computed and measured C_D for the experiment of Bruining (1979)

The C_p was computed and it is shown in Figure 4.13, for $\alpha = 0^\circ$.

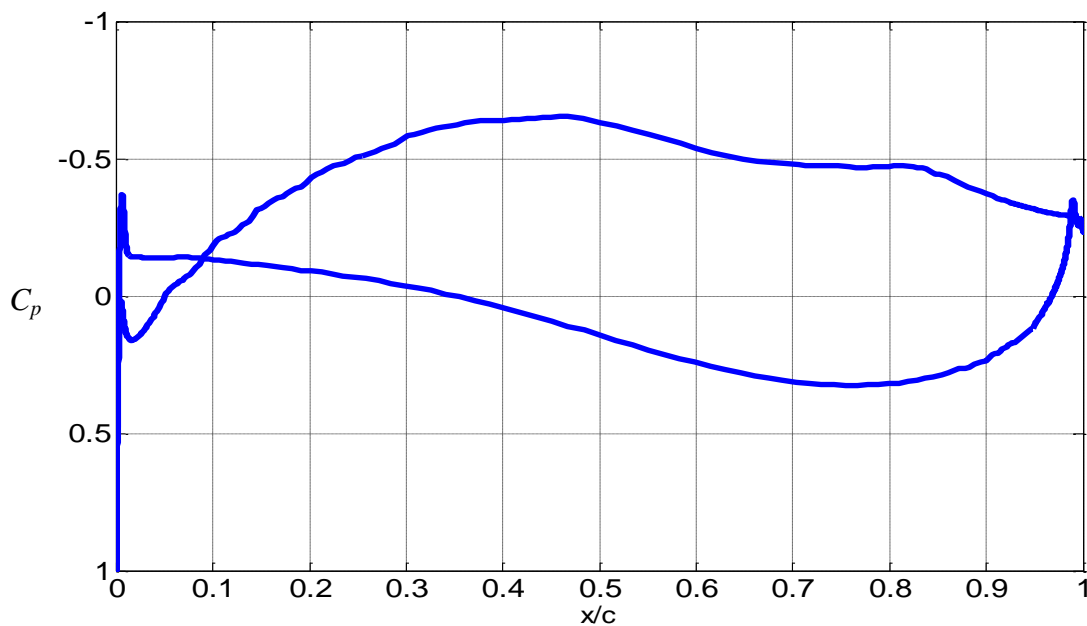


Figure 4.13: Computed pressure, $\alpha = 0^\circ$ for the 10% CA airfoil of Bruining (1979)

Figure 4.14 shows the velocity magnitude contours for $\alpha = 0^\circ$ for $Re = 10^5$, the higher camber of the airfoil has caused significant recirculation on the front of the pressure surface and separation and reattachment on the rear of the suction surface. The upper surface boundary layer was established as laminar prior to separation.

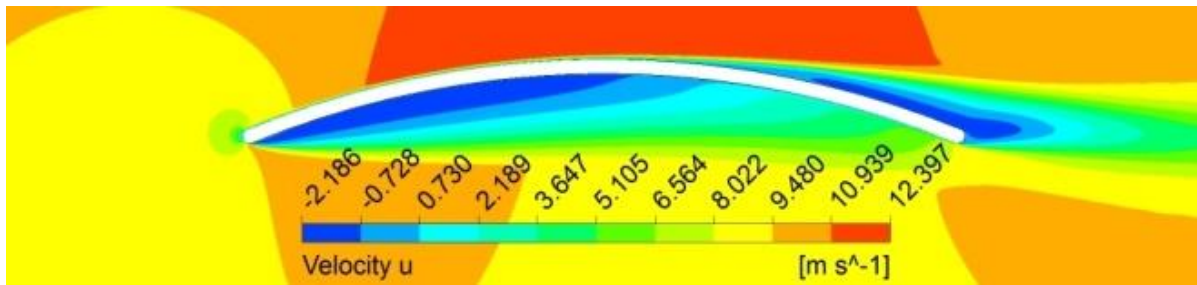


Figure 4.14: Computed velocity magnitude contours at $\alpha = 0^\circ$, $U_\infty = 9.738$ m/s for the experiment of Bruining (1979)

The foregoing calculations are significant to the study of the behavior of cascade. The C_L and C_D were determined by treating the airfoil in isolation using the SST-transition model. After adjusting the model constants as indicated in Table 4.1 the calculation was compared with the experiment and it was found that the model is able to predict the C_L and C_D reasonably. Therefore, it is reasonable to expect that accurate calculations of effect of solidity can be made by changing the upper and lower boundary conditions to periodic to replace the velocity condition used in isolated airfoil calculation.

Chapter 5: Aerodynamics of Circular Arc Cascades for Windmill Applications

5.1 Introduction

In a cascade the geometry and flow pattern repeats periodically along one axis, in this case the y -axis which corresponds to the direction of rotation of the windmill being modeled. Thus, cascade problems are usually analysed by considering one blade or airfoil and imposing periodic boundary conditions on the flow over that element. The airfoil in a cascade operates on a finite mass of air because of the adjacent blades. With the finite mass, the reaction to the L produces a net deflection on the flow in the direction opposite to the lift which does not occur for an airfoil. The aerodynamic performance in terms of L and D was computed for $0.1 \leq \sigma \leq 1.5$, and $-4^\circ \leq \alpha \leq 12^\circ$ at $Re = 10^5$. These values were based on the windmill profile used in the experiment of Wegereef (1984) on a model windmill in a wind tunnel. The blade profile used in this calculation is the Bruining model CA2 airfoil with 10% camber and chord 150mm. The relative velocity at inlet was 11.39m/s. Before discussing the calculations and results, it is necessary to consider the force balance for a cascade as this turned out to be a very good way of assessing the accuracy of the calculations.

5.2 Cascade Theory

Figure 5.1 shows an infinite cascade of identical blades, spaced distance s apart along the y -axis which is the direction of travel of the blade. The free stream velocity for the incompressible fluid is denoted by U_∞ . The body is located at the origin with a typical pitch angle of 45° to the vertical, representing the windmill blade model of Wegereef (1984) who used the same CA

airfoils as Bruining (1979). The LE of the airfoils are collinear in the y - direction. The control volume, CV, shown in Figure 5.1, used to derive equations for L and D by Wood (2011b), has its horizontal faces at $y = \pm S/2$. The faces are labelled in clockwise direction from the upstream.

For faces 2 and 4, the periodic condition implies:

- the pressures are equal at the same x ,
- there is no net efflux of x or y direction momentum, and
- the contribution to the circulation around the contours will cancel.

Circulation Γ is positive in the clockwise direction. The forces exerted on the fluid are given by the rate of change of momentum of the fluid which occurs only in the flow through faces 1 and 3.

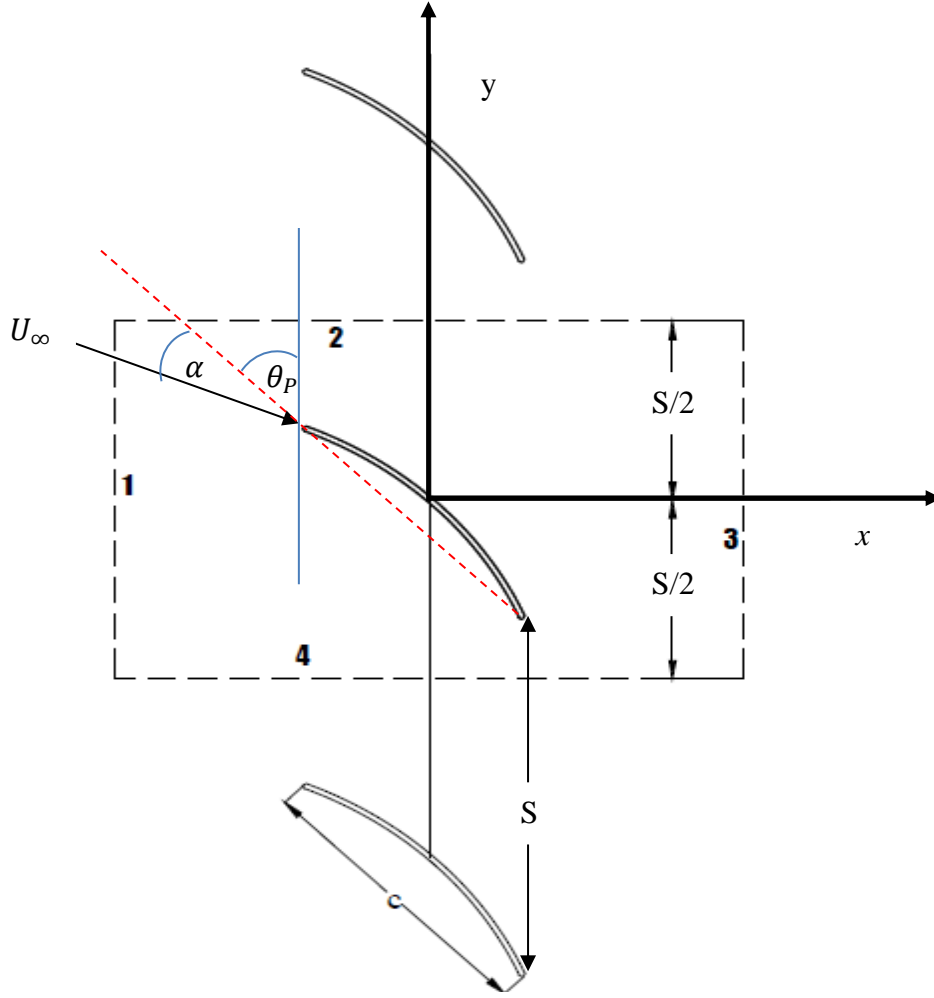


Figure 5.1: Control volume for a cascade of equi- spaced identical bodies

where θ_P is the pitch angle. $U_\infty \sin(\alpha + \theta_P) + u$ is the x -velocity at any point in the flow and the vertical velocity is $U_\infty \cos(\alpha + \theta_P) + v$. Applying the Reynolds transport theorem to the control volume, the y -direction force, F_y , is:

$$\begin{aligned}
 -F_y = & \rho \int_{-S/2}^{S/2} (U_\infty \sin(\alpha + \theta_P) + u_3) v_3 dy \\
 & - \rho \int_{-S/2}^{S/2} (U_\infty \sin(\alpha + \theta_P) + u_1) v_1 dy
 \end{aligned} \tag{5.1}$$

where the subscripts 1 and 3 denote the inlet and outlet faces.

$$F_y = \rho U_\infty \Gamma - \rho \int_{-S/2}^{S/2} (u_1 v_1 + u_3 v_3) v_1 dy \quad (5.2)$$

where Γ is the circulation around the contour. Since the integral on the right of Equation (5.2) is likely to be relatively small, a cascade obeys the same relation between L and bound vorticity - the Kutta Joukowski equation-as does an airfoil. From Equation (5.2), the lifting body can be represented by a vortex of strength Γ . F_x , the x -direction, force is given by

$$\begin{aligned} -F_x + \int_{-S/2}^{S/2} (P_1 - P_3) dy = \\ \rho \int_{-S/2}^{S/2} (U_\infty \sin(\alpha + \theta_p) + u_3)^2 dy - \rho \int_{-S/2}^{S/2} (U_\infty \sin(\alpha + \theta_p) + u_1)^2 dy \end{aligned} \quad (5.3)$$

where P_1 and P_3 are inlet and outlet pressure respectively. Equations (5.1) and (5.3) will be used for consistency checks on the numerical simulation of the CA cascades. The justification for this is that for example in a cascade calculation if there is no change in y -direction velocity there will be no lift force. Therefore, if FLUENT results produce a lift force on the body and there is no force due to momentum, it means that there is a problem with the calculations and it has to be checked.

For an isolated airfoil there is no change in the mean velocity before and after the airfoil. But in cascade there is change in the mean velocity after the airfoil, therefore in order to relate the change it is necessary to take the mean of the change for first order correction for the mean velocity of the blade. Figure 5.2 shows the average velocities entering and leaving a cascade with zero pitch CA. u_1 and u_3 are the average axial velocities at inlet and outlet while v_1 and v_3 are

the corresponding vertical velocities. v_m is the mean velocity in y direction. U_1 and U_3 are the magnitude of the velocity at inlet and outlet respectively , where $U_1 = U_\infty$ in Equation (5.1) to (5.3). The mean velocity has a magnitude U_m and direction α_m .

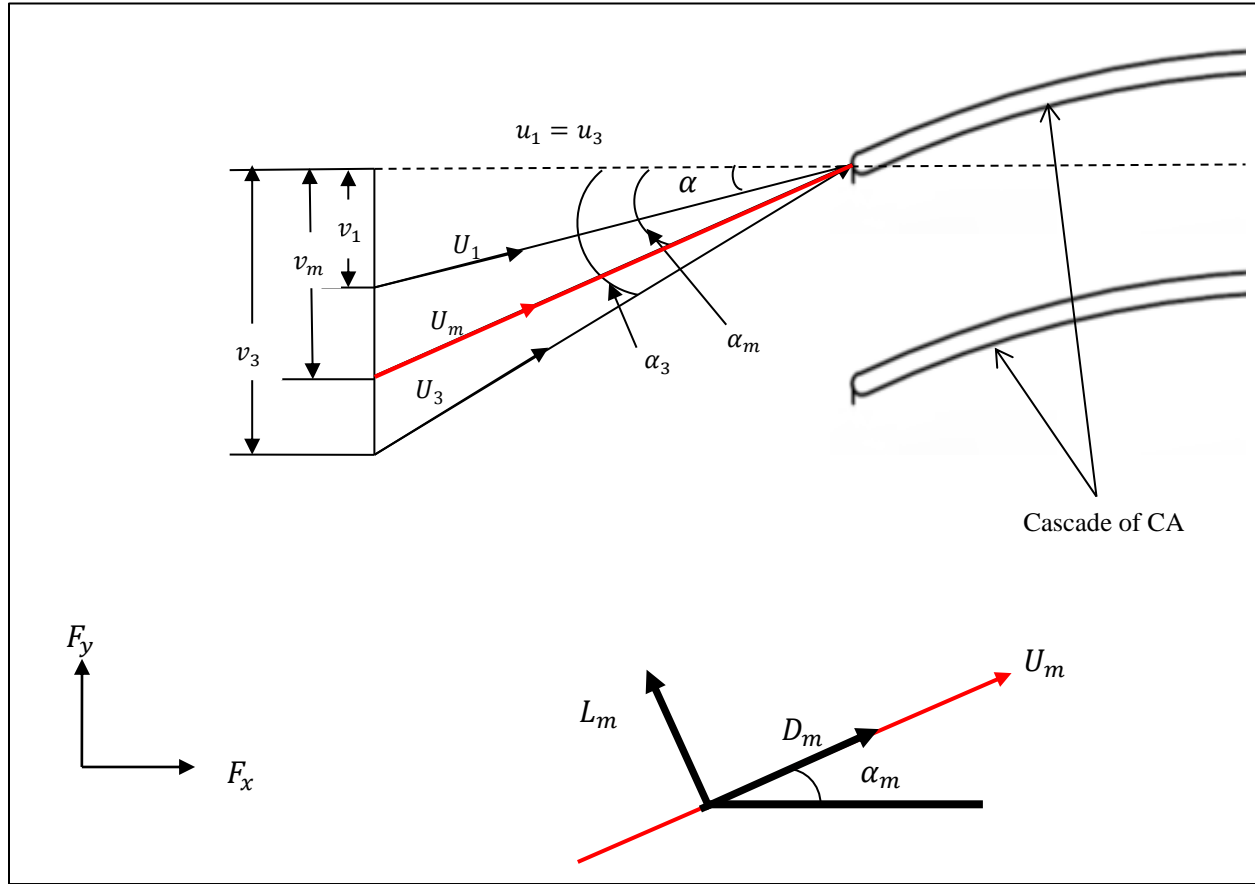


Figure 5.2: Velocity and force diagram of cascade

$$v_m = \frac{v_3 + v_1}{2} \quad (5.4)$$

$$U_m = \sqrt{(u_1^2 + v_m^2)} \quad (5.5)$$

$$\alpha_m = \tan^{-1}\left(\frac{v_m}{u_1}\right) \quad (5.6)$$

C_L and C_D are formulated as follows:

$$C_L = \frac{L_m}{\frac{1}{2}\rho c U_m^2}; C_D = \frac{D_m}{\frac{1}{2}\rho c U_m^2} \quad (5.7)$$

The definition of C_L and C_D in terms of the mean velocity distinguishes a cascade from an airfoil. α_m is used for cascade as defined in Figure 5.2, which is angle of the mean velocity. The cascade results in this thesis are presented as defined in Equations (5.6) and (5.7).

5.3 Calculation Procedure

The calculation procedure was to generate a mesh for the CA2, and then to establish the mesh independence, domain independence and iterative convergence. The periodicity of the domain was also confirmed. The details are explained in the following sub-sections.

5.3.1 Computational Mesh and Boundary Conditions

The unstructured computational mesh was, generated in ICEM. The details of the boundary conditions will be discussed in the next section. The mesh consists of hexahedral elements, the boundaries at high solidities were made by making the boundary follow the curvature of the blade while at low solidity the boundaries were rectangular in shape. For high solidity, two types of mesh were created. The first mesh was created for a single blade and the second was created for two identical blades, called a double blade, in a domain. This was done because the early calculations showed an oscillation in the pressure distribution for the single blade mesh similar to that shown in Suzuki et al. (2011). The double blade mesh was created to check if the oscillations were associated with applying the periodic boundary conditions for a single blade

and also to ascertain periodicity was observed on the single blade. However, once this was established, all the solidity calculations were obtained using a single bladed domain since this is economical.

5.3.1.1 Single Blade Domain

The domain width was determined by the solidity of the cascade. The mesh was imported to the FLUENT where the boundary conditions were set. The inlet boundary condition was velocity inlet with the x - and y - direction velocities determined from the condition that $Re = 10^5$ and the angle of inlet flow. The outlet boundary was defined as outflow, since there is no information of any of the velocities and pressure of the flow. The outflow boundary condition set zero normal gradients for all flow variables except pressure; at boundaries, FLUENT extrapolates required information from the interior nodes.

The periodic BC were defined in FLUENT for the upper and lower boundaries. The periodic zone between the periodic interfaces is repeated infinitely in both directions. The pressure information in the periodic planes is identical and the flow entering the computational model through one periodic boundary is identical to the flow exiting the domain through the other periodic boundary. There are two types of periodic conditions available in FLUENT. The first type does not allow a pressure drop across the periodic planes. The second type allows a pressure gradient to occur across translational periodic boundaries, allowing “fully-developed” periodic flow to be modeled in the flow direction. These calculations used the first form of periodicity.

For a periodic boundary without any pressure drop, there is only one input that the user needs to consider: the flow direction. Rotational periodic boundaries are boundaries that form an included angle about the centreline of a rotationally symmetric geometry. Translational periodic boundaries are boundaries that form periodic planes in a rectilinear geometry, ANSYS (2011). In the thesis, the translational periodic BC was used and no pressure gradient was specified across the periodic boundaries. As will be seen in the section (5.4), the double blade calculations demonstrate that the periodicity was correctly enforced.

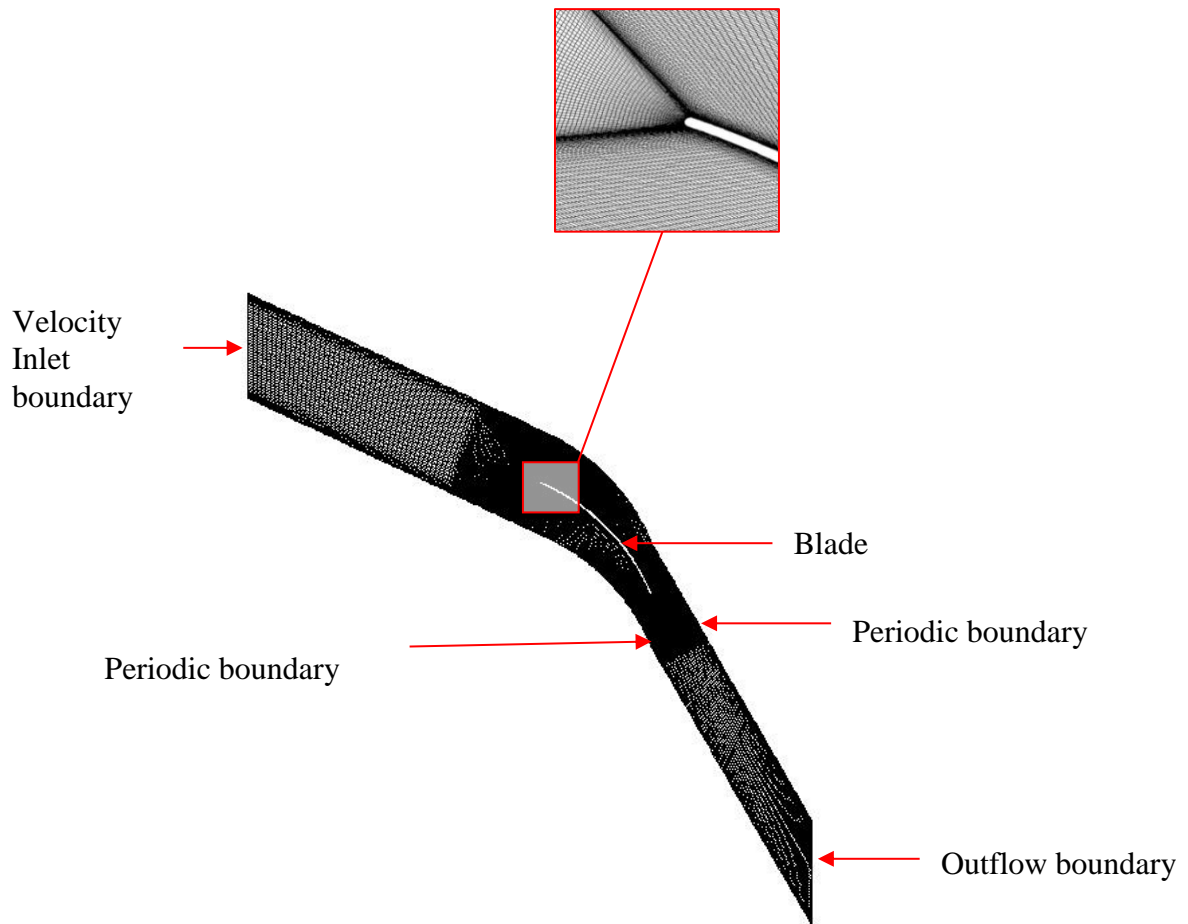


Figure 5.3: Boundary conditions for a high solidity calculation, $\sigma = 1.5$

5.3.1.2 Two-Blade Domain

The domain with two blades is shown in Figure 5.4 for $\sigma = 1.5$. Periodic conditions were imposed on the boundaries containing two identical blades as shown in the Figure 5.4

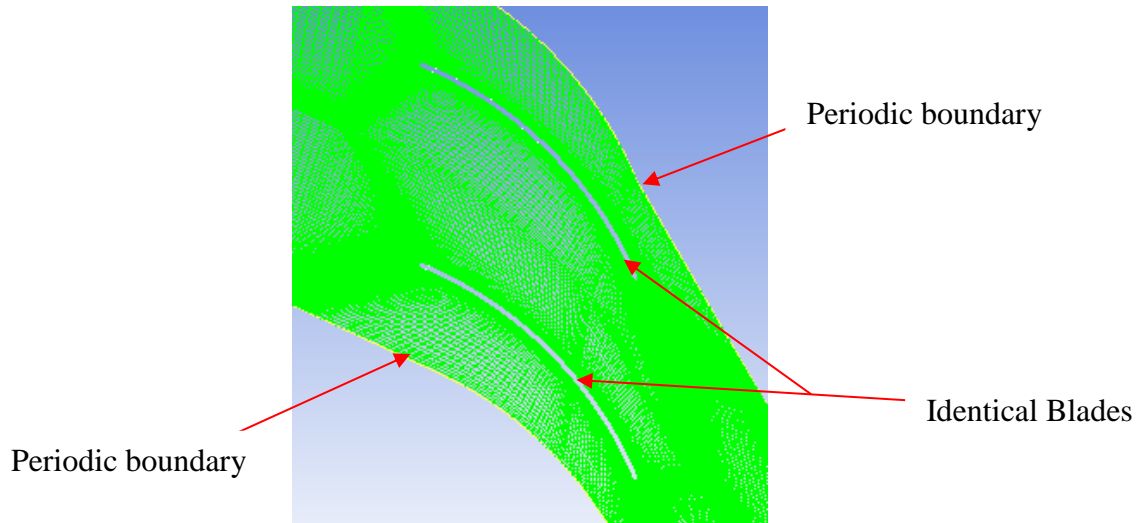


Figure 5.4: Boundary conditions for a high solidity calculation of double blade, $\sigma = 1.5$

5.3.1.3 Domain and Mesh Independence Studies

One of the primary requirements for creating the domain in this thesis for the cascade calculation was to keep the wake within the periodic boundary so that it exited approximately normal to the outlet boundary. This is because the standard for accepting a cascade calculation as “correct” was comparing the momentum balances on the CV defined by the computational domain as determined by Equations (5.1) and (5.3) with the forces on the body to compliment the mesh independence test. It was found that when the wake crossed the periodic boundary the-Equations (5.1) and (5.2) were not obeyed. This is most likely due to the assumed normal BC at the outlet affecting the flow when oblique cutting of the wake should cause significant normal gradients. In order to capture the wake, the upper and lower boundaries corresponding to the periodic

boundaries were made to follow the curvature of the blade. This was highly significant most especially at very high solidity because the spacing were small.

The domains used in these calculations were of two types. The first was used for high solidity and the second used for low solidity calculations as defined by: high solidity, $1.5 \geq \sigma \geq 0.75$, while for low solidity $\sigma < 0.75$. A domain independence test was done for each calculation for all solidities. The test was done for two domains: the first was extended $2c$ upstream of the LE and $2c$ downstream of the TE, and the second extended $4c$ upstream and downstream. At high σ the deviation of the mean pressure at both inlet and outlet were less than 1%, while at low σ , the deviation was found to be more than 1 % this prompted a further test, the details will be discussed in the next section. This is a useful check in order to obtain a result that is domain independent and to consolidate the momentum balance check of Equation (5.1) and (5.3).

5.3.2 Solidity $1.5 \geq \sigma \geq 0.75$

The length of the first computational domain was set at $2c$ upstream of the LE and downstream of the TE. Hereinafter, all references to the upstream and downstream extent of the grid will imply measurement from the LE and TE respectively. This was set after establishing domain independence of the calculation for the range of solidity. Domain independence was determined by comparing the mean of the pressure distribution both at inlet and outlet for two different sizes of domain. It was found out that the deviations were less than 1% as mentioned earlier. For all solidities tested, the second domain extended $4c$ upstream and downstream. In the case of $\sigma = 1.5$ the number of nodes for the $2c$ domains was 48,300 with 1227 iterations required for

convergence criteria were set to scaled residual of 10^{-5} for all parameters, while for the $4c$ domain the number of nodes is 63,240 with 1,290 iterations for the same convergence.

5.3.3 Solidity $\sigma < 0.75$

The procedure used in the high solidity calculations was followed to determine the appropriate domain for the low solidity calculations i.e. initially using the first domain set at $2c$ upstream and downstream and the second domain $4c$ upstream and downstream. The deviations were found to be between 1% and 2%. This prompted further investigation; it was found that comparing the second domain and a new domain set at $8c$ upstream and $10c$ downstream the deviation of the pressure at inlet and outlet are less than 1%. After the domain independence test the domain used for the low solidity calculation was set at $8c$ upstream and $10c$ downstream. These distances are comparable to those used in chapter 5 for the airfoil calculations. However, since at low solidity it was not necessary for the upper and lower boundary to follow the curvature because the blade spacing was high. A rectangular domain was used comparable to the domain used for the airfoil calculations in chapter 5. The spacing for the y -direction spacing was determined by the solidity.

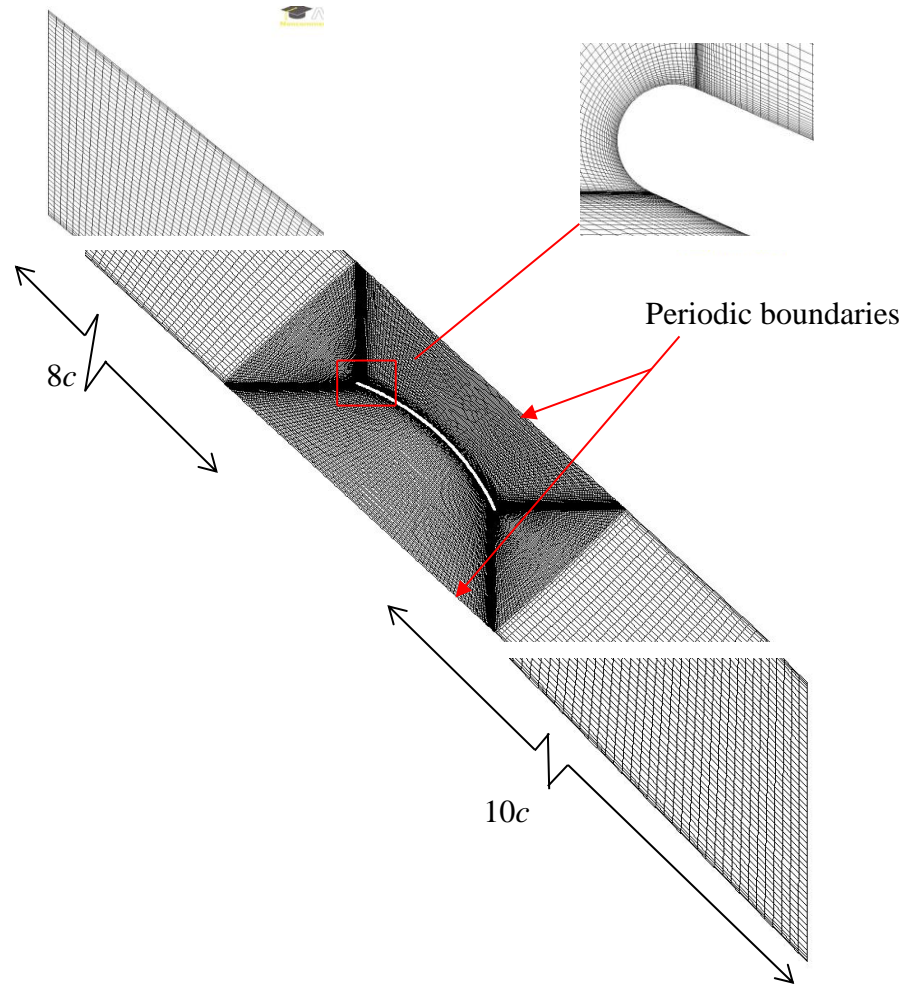


Figure 5.5: Boundary conditions and computational domain for $\sigma < 0.75$

5.3.4 Calculation of F_x and F_y

FLUENT calculates the force on the blade in terms of the horizontal and vertical forces F_x and F_y with the directions defined in Figure 5.2. The total force on the blade is the sum of the pressure and viscous forces as shown in section 5.2. In order to establish that the accuracy of the FLUENT calculation, a comparison of the forces determined in three different ways: (1) directly calculated in FLUENT, (2) by applying Equations (5.1) and (5.3) using output options within FLUENT (Post processing) and (3) by writing a code in Matlab to solve Equations (5.1) and

(5.3) using primitive variable output from FLUENT. It is noted that these calculations were done after the grid independence test. Table 5.2 compares the results for $\alpha_m = 8.5^\circ$ and $\sigma = 1.5$. The following notations were used

Table 5.1: Notation and properties of the computational domain

Domain	Upstream	Down stream
A	2c	2c
B	4c	4c
C (Double blade)	2c	2c

In Table 5.2, the first two columns give the forces directly from FLUENT. The forces are compared based on the single blade domain (A), double blade domain for 2c, (C) domain and 4c domain (B). The Δ indicates % deviation from case A for F_x and F_y .

Table 5.2 Comparing the F_y and F_x for domains A, B and C in (N/m) at $\alpha=4^\circ$, $\sigma = 1.5$.

Case	F_y (N/m)	F_x (N/m)	ΔF_y (%)	ΔF_x (%)
A	4.705	7.032	0	0
B	4.704	7.028	-0.02	-0.05
C Blade 1	4.771	7.101	1.4	0.098
Blade 2	4.660	7.004	-0.96	-0.39

It was found that the maximum deviation from the reference domain (A) is 1.4% in magnitude for F_y and this occurs for the domain with two blades. Table 5.3 shows the comparison between case A and case B, in terms of the methods used in determining the forces on the blades. The difference referenced to force on blade as determined by FLUENT is very small; in all cases, less than 1%. This shows that momentum is conserved in the system and periodicity was observed for all the calculations. It is also important to note that the BC set in Figure 5.3 is observed for case A and B. The Δ is the % deviation from the first column.

Table 5.3: Comparing F_y (N/m) for cases A and B using Matlab and calculated by the three methods explained in the text, for $\alpha = 4^\circ$, $\sigma = 1.5$ and $U_\infty = 11.39$ m/s

Case	F_y (force on blade) (N/m)	F_y (Calculated in FLUENT) (N/m)	F_y (Matlab) (N/m)	ΔF_y (Calculated in FLUENT) %	ΔF_y (Matlab) %
A	4.705	4.708	4.709	0.063	0.085
B	4.704	4.712	4.712	0.17	0.17

Table 5.4: Comparing the F_x (N/m) for A and B using Matlab and calculated in FLUENT, at $\alpha = 4^\circ$, $\sigma = 1.5$ and $U_\infty = 11.39$ m/s

Case	F_x (force on blade) (N/m)	F_x (Calculated in FLUENT) (N/m)	F_x (Matlab) (N/m)	ΔF_x (Calculated in FLUENT)%	ΔF_x (Matlab)%
A	7.032	7.033	7.067	0.014	0.5
B	7.028	7.027	7.047	-0.014	0.27

5.3.5 Single and Double Domain Results

Figure (5.6) and (5.7) show the velocity magnitude for single blade domain and double blade domain, i.e. domains A and C. The velocity is 11.39m/s, and $\alpha = 4^\circ$ in both cases. The contours of velocity magnitude over the two blades are almost identical which shows that periodicity is observed in both calculations

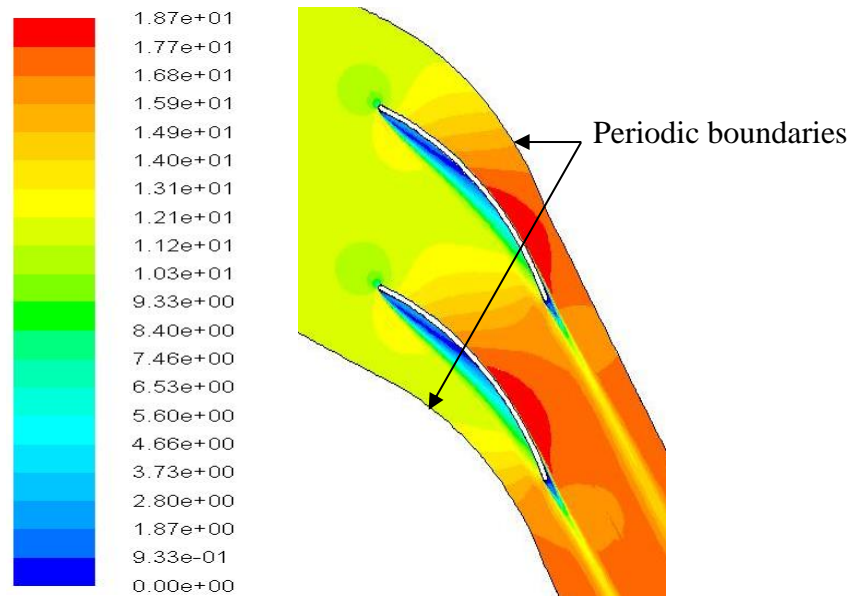


Figure 5.6: Computed velocity magnitude contours in m/s for a double blade CA2 of case C at $\alpha=4^\circ$, $\sigma = 1.5$ and $U_\infty = 11.39$ m/s. Only part of the computational domain is shown.

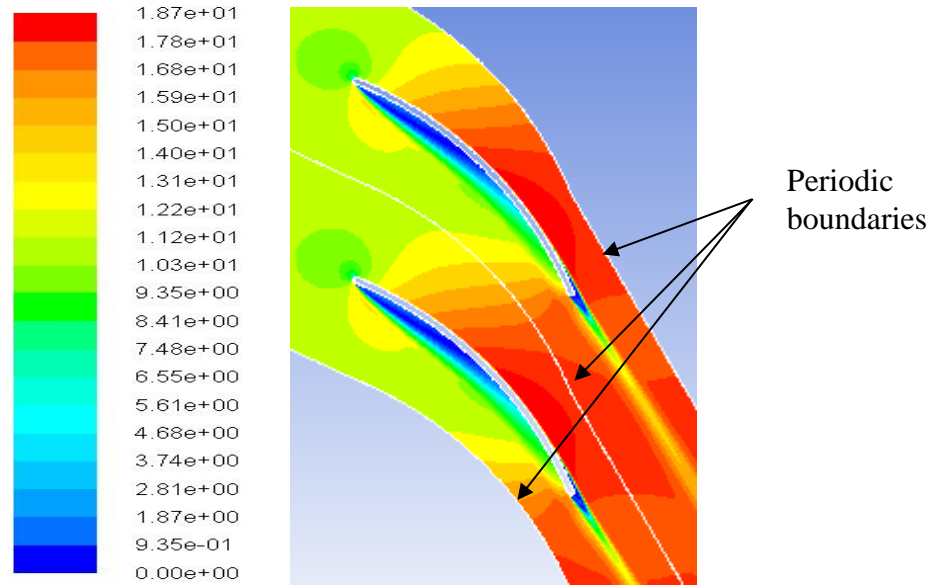


Figure 5.7: Computed velocity magnitude contours in m/s for single blade CA2 of case A at $\alpha=4^\circ$, $\sigma=1.5$ and $U_\infty=11.39$ m/s with periodic repeat. Only part of the computational domain is shown.

. In Figure 5.8 the C_P for the two blades in a domain and a single blade are super imposed. The result shows that they are similar, as mentioned earlier periodicity was observed in both cases.

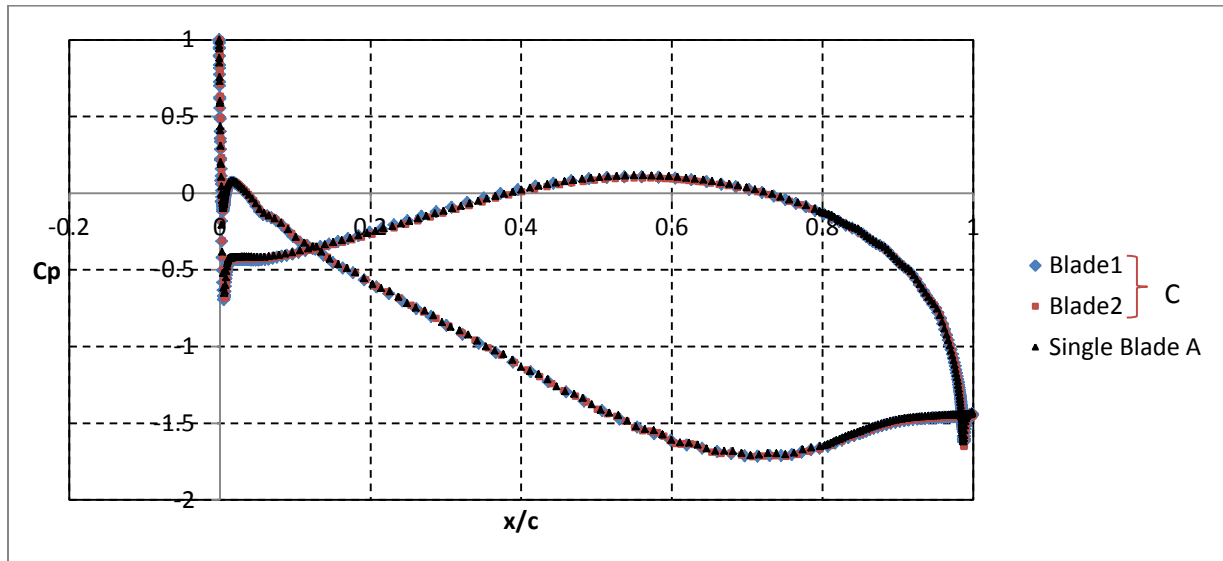


Figure 5.8: Computed C_P for case A and C at $\alpha=4^\circ$ and $U_\infty=11.39$ m/s

Comparing Figures 5.9a and 5.9b the oscillations found in a single blade domain at high σ were absent in the double blade domain. However, as seen in Table 5.2 the deviation of the forces is 2.3% which is relatively small. In view of this, the remaining calculations were done using the single blade domain case (A). The oscillations is indicated in Figure 5.9a, as it can be seen the magnitude of the oscillations which occurred at the bottom of the curve is not significant.

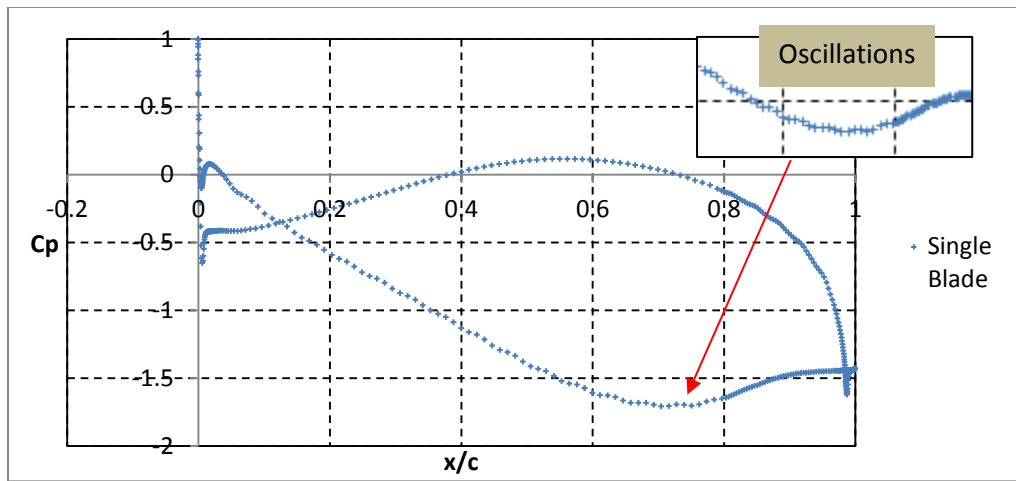


Figure 5.9a: Computed C_P for case A at $\alpha=4^\circ$ and $U_\infty = 11.39$ m/s

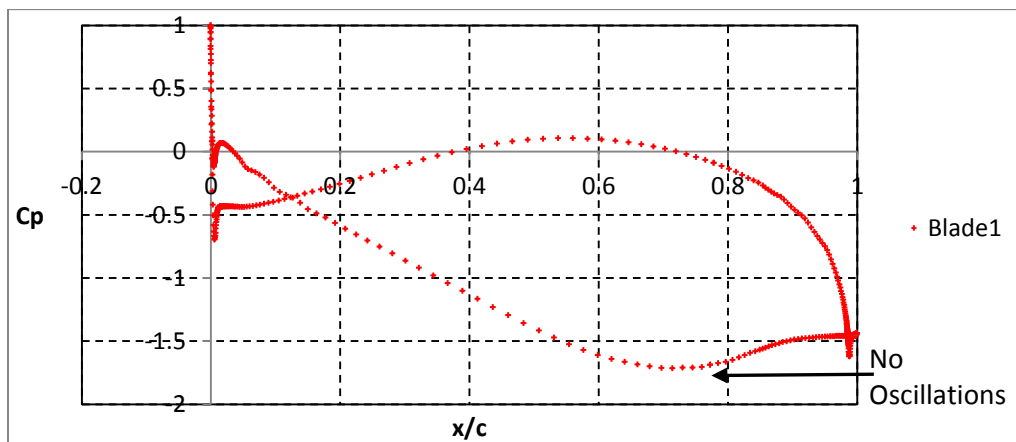


Figure 5.9b: Computed C_P for case C at $\alpha=4^\circ$ and $U_\infty = 11.39$ m/s

5.4 Lift and Drag Coefficients of Blades in the Cascade

The performance of a low solidity windmill can be calculated from the knowledge of forces generated by the airfoil at various sections along the blade, combined with the momentum balance on an annular stream tube passing through the particular blade element. Figure 5.10 shows the computed C_L , α and α_m for CA 2 airfoil over the ranges of σ considered. α is the angle of attack for the isolated airfoil. The C_L for $\sigma = 0.1$ behaves similarly to an isolated airfoil, as the effect of the interaction of the blade is limited. However, this interaction is clearly seen at higher solidity. C_L decreases as the solidity increases. The result is consistent with the result of the experiment of Ikui et al. (1972) discussed in the literature review this suggests that the results are trends meet expectation.

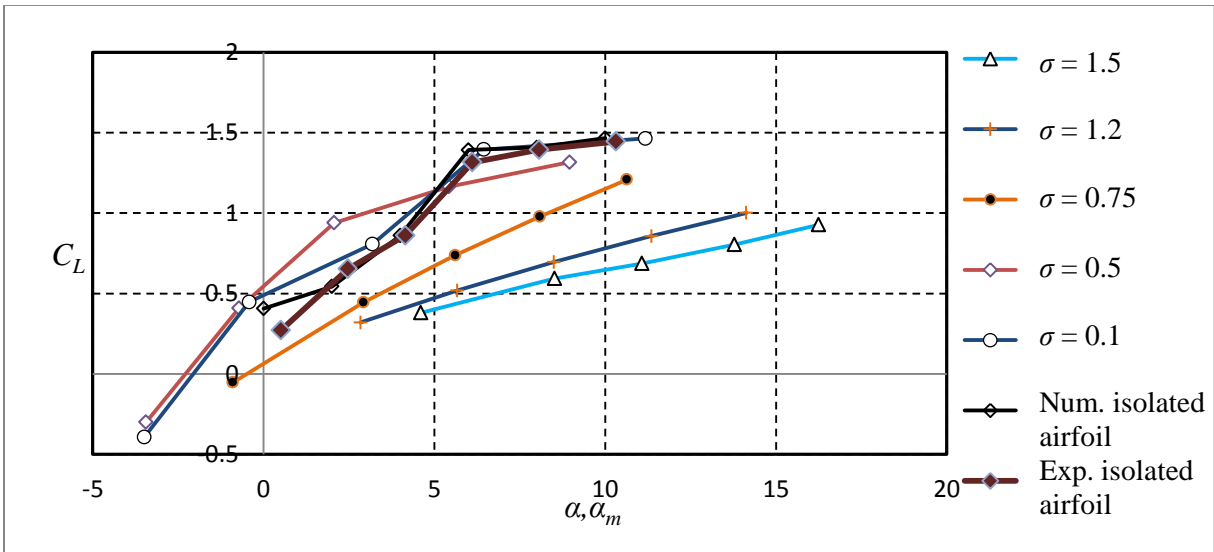


Figure 5.10: Computed C_L against α and α_m for CA2

Figure 5.11 shows the computed C_D against α and α_m for the CA airfoil. For the isolated airfoil the C_D was under-predicted probably due to early transition on the suction side of the airfoil. The

significance of the result is that, even if an incorrect prediction of an isolated airfoil is compared, the changes brought by σ are likely to be correct. The σ correction can then be done on the experimental lift and drag for an isolated airfoil.

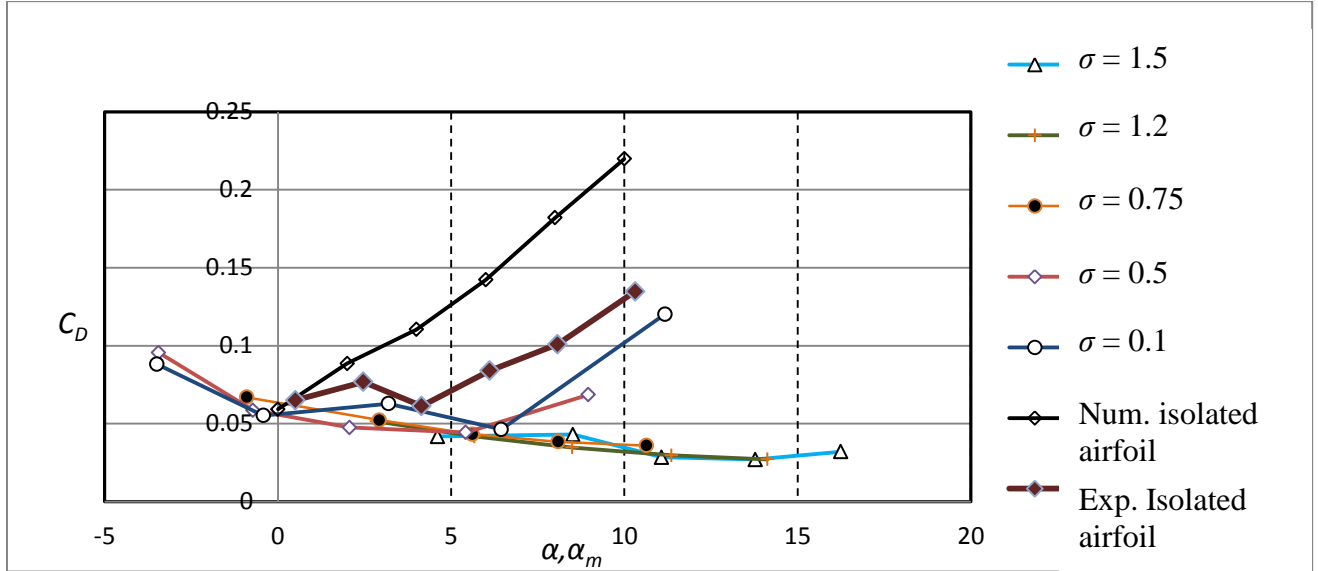


Figure 5.11: Computed C_D against α and α_m for CA2

The C_L/C_D ratio measures the aerodynamic efficiency of the airfoil. As shown in Figure 5.12 the C_L/C_D ratio at low solidity follows the same trends. However, at high solidity the C_L/C_D ratio increases as α increases. Furthermore, for high solidity as α increased there was a corresponding increase in the C_L/C_D of the blade for the range of α considered. The maximum C_L/C_D occurs close to $\alpha \approx 6^\circ$ for low solidity but the optimum angle increases with increasing σ . This is also an important result because it implies that optimum pitch angle depends on solidity. In the next section the flow patterns for nominal $\alpha = 6^\circ$ are presented to show how the increase in σ changes the general features of the flow. The results in Figure 5.12 are comparable to experimental results shown in Figure 2.19 it shows that C_L/C_D increases with σ and at certain σ the C_L/C_D start

to drop. This shows that σ is significant in the study of windmill to know when the maximum C_L/C_D occurred.

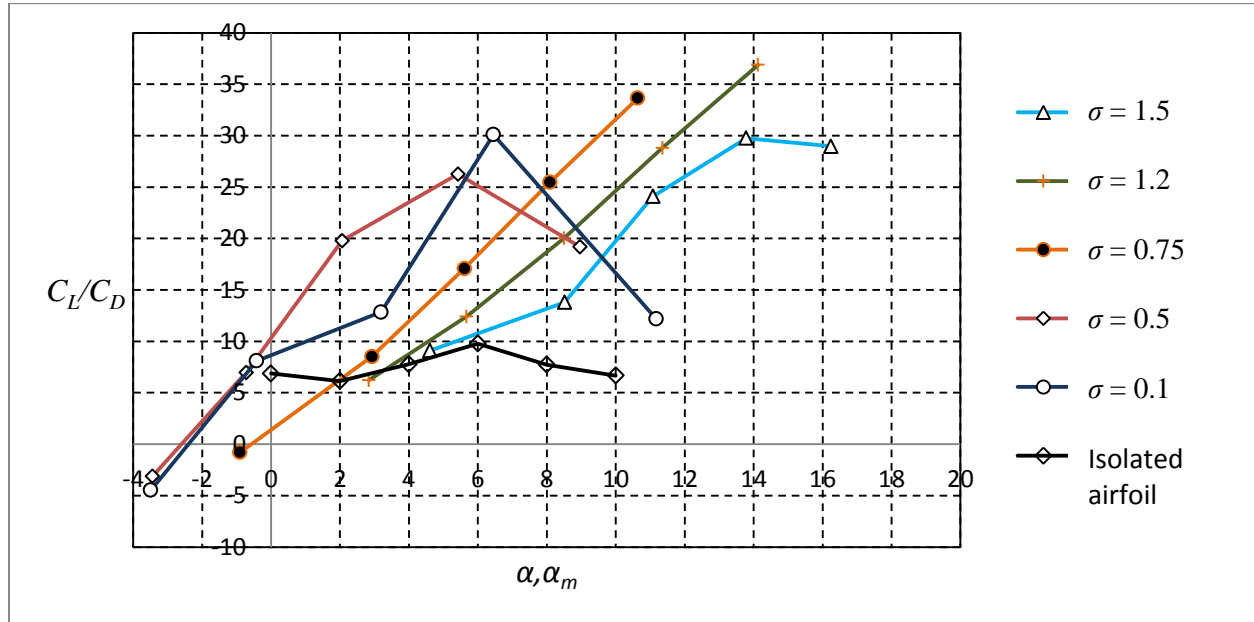


Figure 5.12: Computed C_L/C_D against α and α_m for CA2

The summary of the flow properties is shown in Table 5.5. It shows that at constant α , α_m increases with σ , and as σ increases the C_L and C_D decreases. This implies that if C_L and C_D of an airfoil were estimated at zero σ , the C_L would have been over estimated since at high σ , the C_L and C_D were reduced. The reduction is highly significant, therefore, in order to accurately estimate the power of windmill solidity effect has to be considered. The C_L and C_D in Table 5.5 are as estimated in equation (5.7).

Table 5.5: Comparing σ with α_m , C_L and C_D at nominal $\alpha = 6^\circ$

σ	α_m ($^\circ$)	C_L	C_D
1.5	11.73	0.719	0.0274
1.2	9.54	0.75	0.0329
0.75	7.03	0.883	0.0386
0.5	3.63	1.109	0.0491
0.1	4.56	1.325	0.0346

5.5 Comparing Velocity and Turbulent Kinetic Energy Distribution at Nominal $\alpha = 6^\circ$

In this section the turbulent kinetic energy, k and velocity magnitude distribution for $\sigma = 1.5$, 1.2, 0.75, 0.5 and 0.1 are examined at $\alpha = 6^\circ$. The primary purpose for displaying the plots is to determine the qualitative changes to the flow as σ is reduced. The flow conditions for the calculations of Figure 5.14 to 5.23 are nominal (inlet angle of attack) $\alpha = 6^\circ$ and $U_\infty = 11.39\text{m/s}$.

Figures 5.14 to 5.23 show the contour plots for velocity magnitude and k . The maximum contour values for the k and velocity magnitude was set to be the same for all the σ for easy comparison. The values were set as $15\text{m}^2/\text{s}^2$ for k and 19m/s for velocity magnitude. This causes a white region in Figure 5.17 and Figure 5.20 where some values exceed $15\text{m}^2/\text{s}^2$ and 19m/s respectively. Figure 5.13 shows a close view of the Figure 5.15. k and the streamlines, shown as black lines, are included to show the behaviour of the laminar boundary layer. The flow experienced immediate separation on the pressure side of the CA and a reattachment occurred at about 50% of the chord.

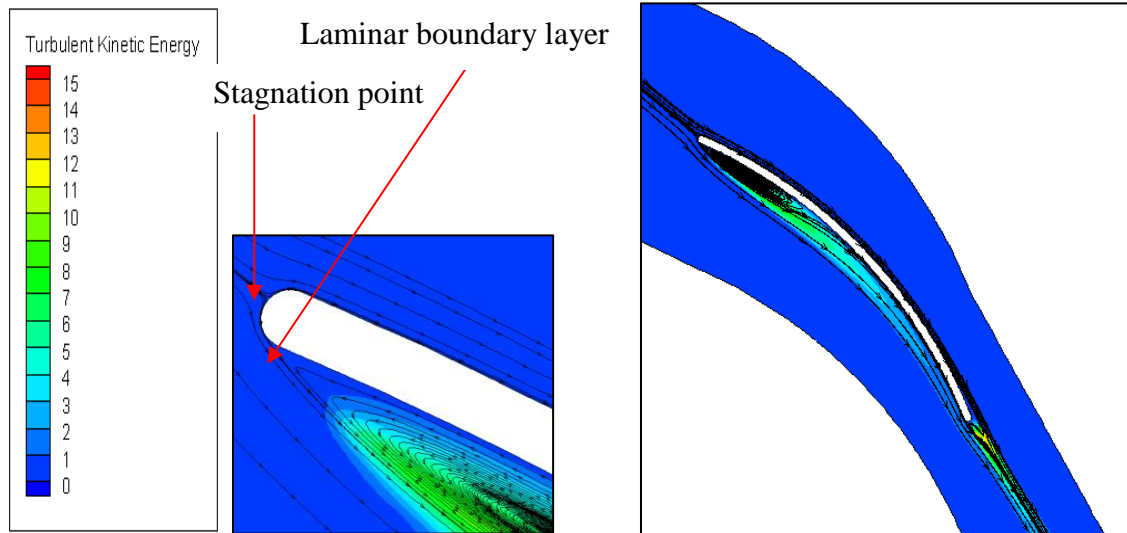


Figure 5.13: Contours of Turbulent Kinetic Energy (k) (m^2/s^2), $\sigma = 1.5$, for part of the computational domain. The left figure shows part of the pressure surface boundary layer and the right shows part of the suction surface layer.

Figures 5.14-5.23 show that, for all solidities, the flow after the stagnation point remained laminar, until separation for all solidities. The separated flow then went through transition and to turbulence. On the pressure side, the flow reattached to form a LSB, whereas it remained separated on the suction side for all solidities. As the solidity decreases the size of the LSB at the pressure side reduced as shown by the dark blue region representing the recirculation zone in the velocity magnitude contours. At $\sigma = 1.5$ the pressure side boundary layer remains attached, but separation occurred on the suction side. There is also an increase in the size of the bubble formed on the suction side of the TE. There are no separation bubbles on the suction side and thus there is no reattachment. From these figures, changing the solidity has a large impact on the flows as it does on the L and D .

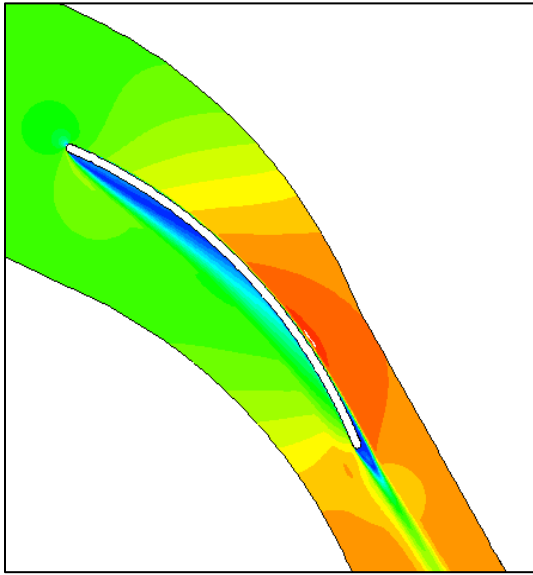


Figure 5.14: Contours of velocity magnitude (m/s), $\sigma = 1.5$, part of the computational domain

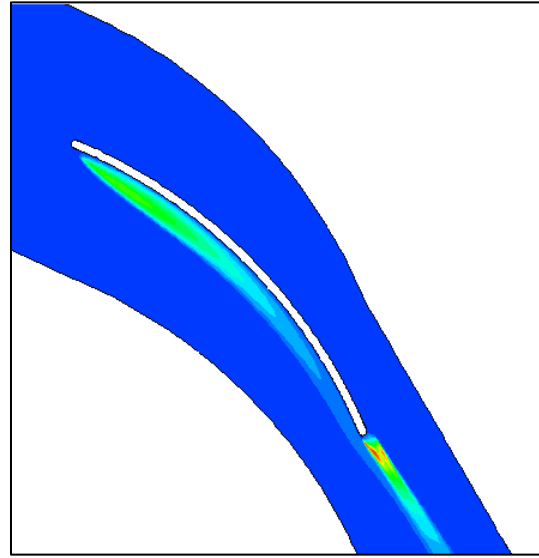


Figure 5.15: Contours of Turbulent Kinetic Energy (k) (m^2/s^2), $\sigma = 1.5$, for part of the computational domain

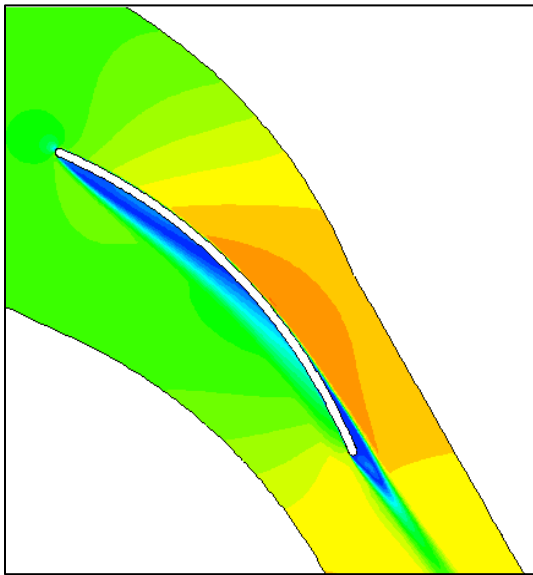


Figure 5.16: Contours of velocity magnitude (m/s) $\sigma = 1.2$, for part of the computational domain.

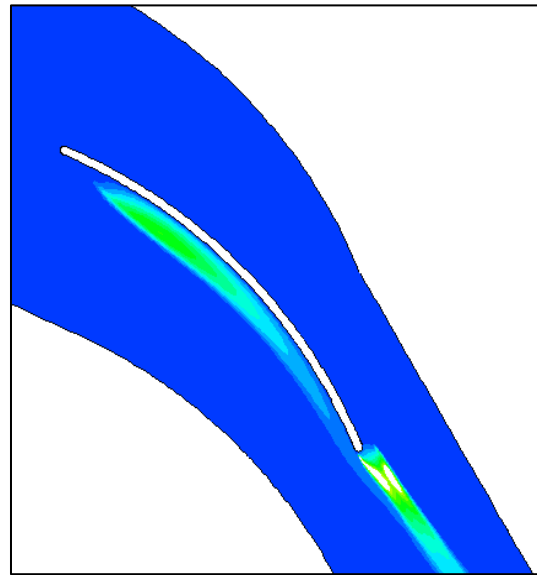


Figure 5.17: Contours of Turbulent Kinetic Energy, (k) (m^2/s^2), $\sigma = 1.2$, for part of the computational domain.

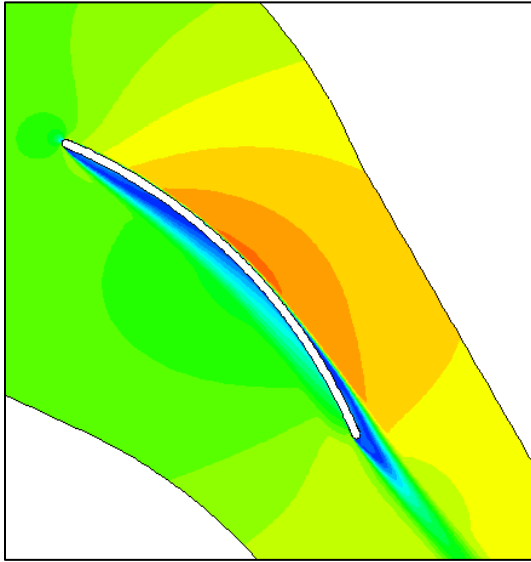


Figure 5.18: Contours of velocity magnitude (m/s), $\sigma = 0.75$, for part of the computational domain

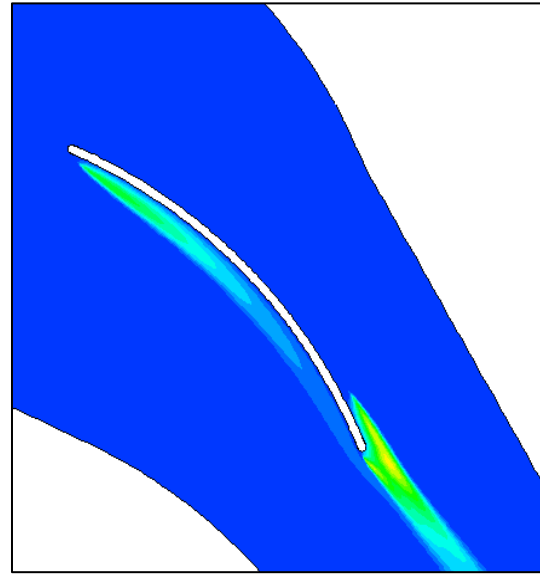


Figure 5.19: Contours of Turbulent Kinetic Energy (k), (m^2/s^2), $\sigma = 0.75$, part of the computational domain

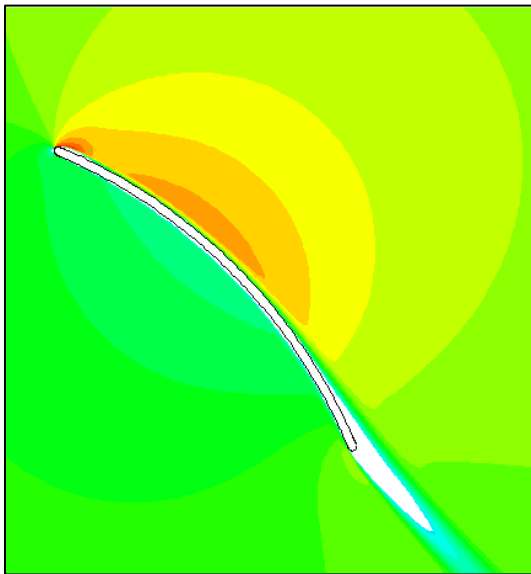


Figure 5.20: Contours of velocity magnitude (m/s), $\sigma = 0.5$, for part of computational the domain

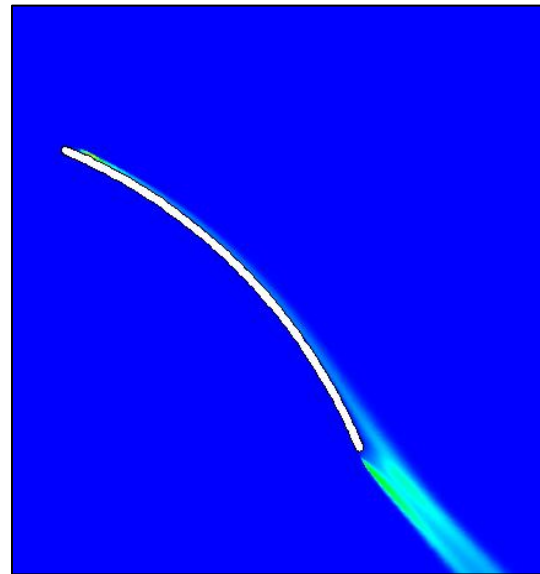


Figure 5.21: Contours of Turbulent Kinetic Energy (k), (m^2/s^2), $\sigma = 0.5$, part of the computational domain



Figure 5.22: Contours of velocity magnitude (m/s), $\sigma = 0.1$, for part of the computational domain

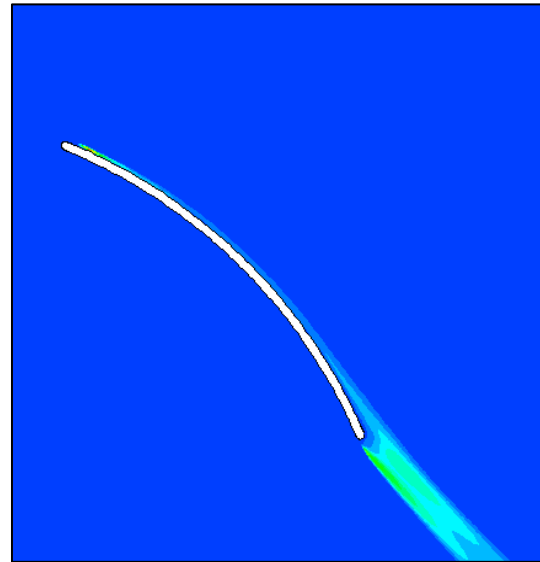


Figure 5.23: Contours of Turbulent Kinetic Energy (k) (m^2/s^2), $\sigma = 0.1$, for part of the computational domain

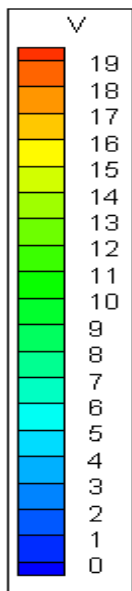


Figure 5.24: Velocity magnitude (m/s), legend for Figures 5.14, 5.16, 5.18, 5.20 & 5.22

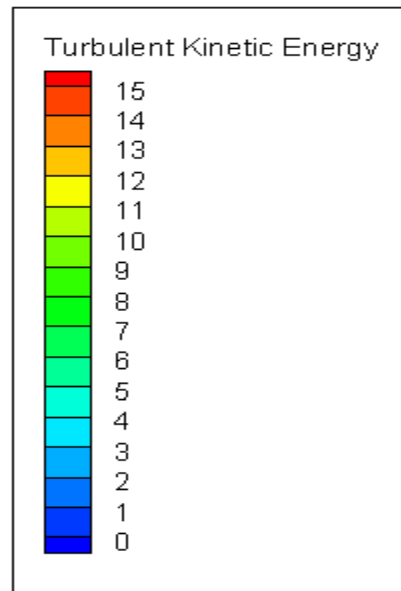


Figure 5.25: Turbulent Kinetic Energy (k) (m^2/s^2), legend for Figures 5.15, 5.17, 5.19, 5.21 & 5.23.

Chapter 6: Conclusion & Recommendations

6.1 Conclusion

The results of Chapter 5 show convincingly that σ has a big impact on the L and D generated on a circular arc airfoil used commonly in water pumping windmills. Like other wind turbines, windmills can be analyzed using blade element theory which requires the L and D as inputs. It has been shown that C_L and C_D as functions of α and σ are needed for BET analysis, and can either be determined by experiment or CFD. CFD was used in this thesis to compute the C_P and the C_L and C_D of two CA airfoils, CA1 and CA2 respectively. The results of the zero solidity calculation were compared with experiment, and then the effects of increasing the solidity were explored computationally.

The SST-transition turbulence model was used and it proved to be capable of predicting the complex flow of a CA where separation occurred at all α considered. This was achieved changing the transition model constants in order to match the experiment on CA1 which was done at Re of 62,000. The changed constants were used throughout the thesis. It can be concluded that result was a reasonable match with the experiment compared to previous work with the SST-transition model of Zierke et al. (1989) as reported in Menter et al. (2006). In Table 4.2, the C_P distribution for the experiment on CA1 and calculation were compared, the results showed a maximum of 6% deviation from the experiment which is a meaningful result for a flow that is difficult to analyse because of the presence of LSB.

The C_L and C_D measured on CA2 were compared with the calculations and a reasonable matching of the C_L was achieved at $Re = 10^5$. However, the C_D was over-predicted. As reported earlier this could be the result of early transition prediction on the airfoil. The accurate prediction of the C_P distribution for CA1 and the C_L and C_D for CA2 respectively was extended to calculate the effect of σ on the C_L and C_D for CA2.

The σ calculation was done for $Re = 10^5$ and $0.1 \leq \sigma \leq 1.5$. A procedure was developed to ascertain the accuracy and mesh independence studies of the results from the cascade calculations, this involved using momentum balances to confirm the accuracy of the results in terms L and D as there was no solidity experiment for this particular case. The momentum balance calculation proved to be a very useful check for all the results. The LSB on the blade was confirmed from the contours of turbulent kinetic energy and the streamlines. It was found the laminar boundary layer on the pressure side separated after the stagnation point as a result of the adverse pressure gradient. The point of separation and reattachment were determined as the points where the wall shear stress was zero. The key to good computational results at low Re lies in the accurate prediction of transition in LSB because, in all cases studied, transition to turbulence occurred only after separation of the boundary layer.

The other major challenge was capturing the wake within the boundary of the computational domain which proved significant in achieving the results. For calculations done without capturing the wake, it was found that the momentum balance was in error for more than 5%. This was achieved by making the boundary of the computational domain follow the blade curvature at

high solidity. This problem did not occur at low solidity since the boundaries were considerably far from the blade. The momentum balance error was less than 1% for all the cascade calculations as shown in Table 5.3.

Furthermore, the cascades calculations show that the flow pattern is strongly affected by the interaction of the blades. This was evident in the study of the velocity and the turbulent kinetic energy contour in chapter 5. The LSB on the pressure surface reduced, whereas there were no bubbles on the suction side. At high solidity C_L/C_D continued to increase significantly with increasing mean angle of attack, while at low solidity C_L/C_D peaked at a value close to 6° . The C_L/C_D curve at low solidity behaved like isolated airfoil. Wind turbines calculations use zero solidity values C_L and C_D whereas the present results show huge changes in C_L and C_D with increasing solidity from Table 5.5. As solidity increased the C_L and C_D reduced significantly. This suggests the need to consider solidity effect in wind turbines of nearly all solidities. The C_L and C_D against α_m shows similar trends to the experimental results of Ikui et al. (1972).

6.2 Recommendations

Based on the findings in this project, the following are recommended;

- (1) The reliability of experiment is expected to be high therefore experiment should be conducted to measure the lift and drag on circular arc cascade considering the complexity of the flow at low Re .
- (2) Spars should be modeled as part of the blade in order to be able to get a result that reflects reality.
- (3) The variable pitch should be considered in future, in order to account for the flow over the length of the windmill blade.
- (4) Focus also should be on analysing the effects of different turbulence models to establish the model that is able to resolve the flow more correctly on the surface of the blade and reduce the discrepancy in the airfoil lift.

References

B.J Abu-Ghannam and R. Shaw. “Natural Transition of Boundary Layers –The Effects of Turbulence, Pressure Gradient, and Flow History,” *Journal of Mechanical Engineering Science*, Vol. 22, No. 5, pp. 213 – 228, 1980.

N. Ahmed, B.S. Yilbas, M.O. Budair. “Computational Study into the Flow Field Developed Around a Cascade of NACA 0012 Airfoils”, *Computational Methods in Applied Mechanics and Engineering*, 167, pp. 17-32, 1998.

Alamy photograph: Wind turbine at Horse Hollow wind farm, North farm Nolan.
<http://www.guardian.co.uk/environment/2012/apr/29/wind-farms-night-temperatures-study>

W. K Anderson, D. L. Bonhaus. An implicit upwind algorithm for computing turbulent flows on unstructured grids. *Computers fluids*. Vol. 23, No. 1, pp. 1-21, 1994

ANSYS. ANSYS academic research, Fluent theory guide. *Technology Dr. Canonsburg, PA* 15317, 2011.

A. Bruining, Aerodynamic Characteristics of a Curved Plate Airfoil Section at Reynolds Numbers 60,000 and 100,000 and angles of attack from -10 to +90 degrees, Delft University of Technology, Report LR-281, 1979. downloaded from:
<http://repository.tudelft.nl/view/ir/uuid:6b92442a-01f7-4b7c-8d53-c4f10720ff3e/>

T. Burton, N. Jenkins, D. Sharpe, E. Bossanyi. Wind energy Hand book, John Wiley & Sons, 2011.

S. A. Deutsch. The measurement of boundary layers on a compressor blade in cascade. I-A unique experimental facility. *32nd International Gas Turbine Conference and Exhibition*.

<http://www.telosnet.com/wind/early.html> 1987.

S. L. Dixon. Fluid mechanics and thermodynamics of turbomachinery. Butterworth-Heinemann, 2005.

R. Eftekhari, R. Taghavi, G. Ghassabi, P. Hooshmand, F. Shirinzadeh, Experimental and numerical study of solidity and incidence effect on aerodynamic performance of axial compressor. *Journal of Basic and Applied Scientific Research*, pp. 1169-1179, 2012.

A. Gareev, P. Cooper, and P. B. Kosasih. CFD analysis of air turbines as power take-off systems in oscillating water column wave energy conversion plant. In *Proceedings of the 8th European wave and tidal energy conference. Uppsala, Sweden*. pp. 777-785, 2009.

M.S Genç, İ Karasu, H. H. Açikel and M. T. Akpolat. Low Reynolds Number Flows and Transition, Low Reynolds Number Aerodynamics and Transition, M.S. Genc (Ed.), ISBN: 978-953-51-0492-6, InTech, 2012. Available from: <http://www.intechopen.com/books/low-reynolds-number-aerodynamics-and-transition/low-reynolds-number-flows-and-transition>.

J. O. Hinze. Turbulence, New York: McGraw Hill, 1975

T. Ikui, M. Inoue and K. Kaneko. On the Cascade Performance of Circular-arc Blades, *International symposium on gas turbines in Tokyo*. 1972.

M. Q. Islam, A.S. Islam. The aerodynamic performance of a horizontal-axis wind turbine calculated by strip theory and cascade theory, *JSME International Journal Series B*, 37; pp. 871-877. 1994.

S. Katzoff, S. Robert, Finn, and James C. Lawrence. Interference method for obtaining the potential flow past an arbitrary cascade of airfoils. "NACA TN 1252." National Advisory Committee for Aeronautics, (1947).

J. A. C. Kentfield. The fundamentals of wind-driven water pumpers. Gordon and Breach Science Publishers. 1996.

J. A. C. Kentfield: Wind energy article. The Canadian encyclopedia article <http://www.thecanadianencyclopedia.com/articles/wind-energy>, accessed April, 2013.

T. Köktürk, Design and Performance Analysis of a Reversible Axial Flow Fan, thesis, Middle East Technical University, 2005. <http://etd.lib.metu.edu.tr/upload/12606116/index.pdf>, accessed 2013.

P. J. Kunz, and I. M. Kroo. Analysis and Design of Airfoils for use at Ultra-Low Reynolds number. In proceedings *AIAA fixed and flapping wing aerodynamics for micro air vehicle applications conference*, Norte Dame, DOI: 10.2514/5.9781600866654.0035.0060, pp. 35-60, 2001.

R. Magdi and A. M. Ragheb. Wind turbines theory - The Betz equation and optimal rotor tip speed ratio, Fundamental and advanced topics in wind power, Carriveau (Ed.), ISBN: 978-953-

307-508-2, InTech, Available from: <http://www.intechopen.com/books/fundamental-and-advanced-topicsin>, 2011.

M. Mecke, and J. Enciso. Using Renewable Energy to Pump Water, 2004. Texas

Agriculture Communications, the Texas A&M University System, report number L5457. Available at Available <http://aces.nmsu.edu/ces/windmill/documents/using-renevable-energy-to-pump-water.pdf>, accessed 2013.

F. R. Menter, R. B. Langtry, S. R. Likki, Y. B. Suzen, P. G. Huang, and S. Völker. "A correlation-based transition model using local variables-Part I: model formulation." *Journal of Turbomachinery* 128, no. 3: pp. 413-422, 2006

F. R. Menter and R. B. Langtry. Transition Modelling for Turbomachinery Flows, Low Reynolds Number Aerodynamics and Transition, M.S. Genc (Ed.), ISBN: 978-953-51-0492-6. In Tech Available from: <http://www.intechopen.com/books/low-reynolds-number-aerodynamics-and-transition/transitionmodelling-for-turbomachinery-flows>, 2012.

T. J Mueller. Aerodynamic measurements at low Reynolds numbers for fixed wing micro-air vehicles. University Norte Dame, Department of Aerospace and Mechanical Engineering, Accession Number : ADP010760, 2000.

E. Muljadi, L. Flowers, J. Green and M. Bergey. Electric Design of Wind-Electric Water Pumping Systems *J. Sol. Energy Eng.* 118(4), pp. 246-252, 1996.

M. O. Okamoto, A. Azuma. Experimental Study on Aerodynamic Characteristics of Unsteady Wings at Low Reynolds Number, *AIAA J*, 43; pp. 2526 – 2536, 2005.

M. O. Okamoto, M. Yasuda, and A. Azuma. Aerodynamic characteristics of the wings and body of a dragonfly, *Journal of Experimental Biology* 199, pp. 281–94, 1996.

M. M. Pandey, K.P. Pandey and T.P. Ojha. Aerodynamic characteristics of cambered steel plates in relation to their use in wind energy conversion systems, *Wind Engineering*, 12; pp. 90 – 103, 1988.

A.E. Pinilla, J.D. Burton, P.D. Dunn. Wind energy to water pumped: conversion efficiency limits using single-acting lift pumps, *Proc. BWEA Conf.* 1984.

S. Raghunathan. The Wells Air Turbine for Wave Energy Conversion. *Prog. Aerospace Sci.*, 31: pp. 335-386, 1995.

R. P. P. Rijs, P. Jacobs, P.T. Smulders. Parameter study of the performance of slow running rotors, *Journal of Wind Engineering and Industrial Aerodynamics*, 39; Issues 1-3, pp. 95-103, 1992.

R. P. P. Rijs, P.T. Smulders, Blade element theory for performance analysis of slow running rotors, *Wind Engineering*, 14; pp. 62 – 79, 1990.

W. Shyy. Y. Lian, J. Tang, D. Viieru. H. Liu. Aerodynamics of low Reynolds number flyers. Vol. 22. Cambridge University Press, 2008.

S. Singh, J. Singh G. Mishra, A. Mishra. Wind Energy and its application in generation of electric power using electromechanical generation drive. *International Journal on Advanced Electrical and Electronics Engineering*, 1, Issue 1, pp. 2278-8948, 2012.

K. Suluksna, J. Ekachai, Assessment of intermittency transport equations for modeling transition in boundary layers subjected to freestream turbulence, *International Journal of Heat and Fluid Flow* 29(1): pp. 48–61, 2008.

S Sunada, T Yasuda, K Yasuda, K Kawachi, Comparison of wing characteristics at an ultralow Reynolds number. *Journal of aircraft*, 39(2), pp. 331-338, 2002.

M. Suzuki, T. Setoguchi and K. Kaneko. Prediction of Cascade Performance of Circular-Arc Blades with CFD. *International Journal of Fluid Machinery and Systems* DOI: <http://dx.doi.org/10.5293/IJFMS.2011.4.4.360> Vol. 4, No. 4, 2011

A. Tezuka, Y. Sunada, K Rinoie. Surface pressure measurements on 4% circular arc airfoil at low Reynolds number, *J. of Aircraft*, 45; pp. 2164-2167, 2008.

UN website: <http://www.un.org/waterforlifedecade/scarcity.shtml> Accessed 2013.

H. K. Versteeg and W. Malalasekera. An introduction to computational fluid dynamics: the finite volume method. Prentice Hall, 2007.

R.A. Wallis. Wind tunnel tests on a series of circular arc plate aerofoils, Aerodynamics Note 74, Divn Aeronautics, CSIRO, Australia, 1946.

E. Wegereef, Scale model of the ITDG 6meter rotor wind tunnel tests for different bade setting angles. Report of Twente University of Technology, Netherlands, windmill group. Report WM 076, 1984.

F. E. Weick, Aircraft Propeller Design, *McGraw-Hill Book Company, Inc.*, p. 59. 1930.

F.S. Weinig. "Theory of two-dimensional flow through cascades." In *high speed aerodynamics and jet propulsion, Vol. X: Aerodynamics of turbines and compressors*, edited by W.R. Hawthorne, Princeton University Press, Princeton, 10: pp. 24-50, 1964.

D. Wilcox. *Turbulence Modeling for CFD (Hardcover)*. DCW Industries, Inc.; 3rd edition, 2006.

D. H. Wood, *Small Wind Turbines: Design, and Application*, Springer, London, 2011a.

D. H. Wood, "Deriving the Kutta-Joukowski Equation and Some of Its Generalizations Using Momentum Balances," *Open Journal of Fluid Dynamics*, Vol. 1 No. 1, pp. 12-16. doi: 10.4236/ojfd.2011.11002, 2011b.

W.C. Zierke, S. Deutsch. The measurement of boundary layers on a compressor blade in cascade - Vols. 1 and 2. *NASA CR 185118*, 1989.

Appendix A

Review of Numerical Methods

A.1 Introduction

This Appendix describes the CFD methodology used in this thesis; detailed description can be found in many standard CFD text books and ANSYS FLUENT - Theory guide, ANSYS (2011). An outline of the key equations is presented in this report on the governing equations.

A.2 The Conservation of Mass and Navier-Stokes Equations

The governing equations of Newtonian fluid follow are derived from the conservation of mass and momentum Versteeg and Malalasekera (2007).

The equation for conservation of mass is known as continuity equation and for incompressible flow is:

$$\frac{\partial u_j}{\partial x_j} = 0 \quad (\text{A.1})$$

The vectors u_j and x_j are velocity and position in the Cartesian system, and repeated indices denote summing over all three component directions. The conservation of momentum known as the Navier- Stokes (N-S) equation is, in Cartesian co-ordinates,

$$\rho \frac{\partial u_j}{\partial t} + \rho u_i \frac{\partial u_j}{\partial x_i} = - \frac{\partial P}{\partial x_j} + \mu \frac{\partial}{\partial x_i} \left(\frac{\partial u_j}{\partial x_i} + \frac{\partial u_i}{\partial x_j} \right) \quad (\text{A.2})$$

where P is the pressure, ρ is the density and μ is the dynamic viscosity of the fluid.

A.3.1 Domain Discretization Methods.

A.3 Computational Fluid Dynamics

As can be seen from Equations (A.1) and (A.2), the governing equations are a set of partial differential equations for the variables P and u_j over a continuous domain that have no known, general solution. To solve the equations numerically requires approximation by discrete forms. There are three different methods used in CFD: finite difference, finite element and finite volume. FLUENT uses finite volume methods to transform the general transport equations into general linear, algebraic relations which can be solved easily by implicit Gauss-Seidel scheme ANSYS, (2011). Detailed information on the finite volume method can be found in Versteeg and Malalasekera (2007).

A.3.1 Discretization Errors

These errors result from the higher order terms that are excluded from the discretized governing equations. Discretization errors lead to differences between the exact solution of the modelled equations and numerical solutions with limited time and space resolution. The localised error can be reduced by increasing the order of accuracy of the discrete approximations and/or by reducing the mesh spacing in regions of rapid changing solution. This is why it is essential to demonstrate grid-independence of any numerically computed flow field.

A.3.2 Finite Volume Method

The derivation of the discrete equations in finite volume methods is based directly on the underlying physical principles. For simplicity consider a general case of a pure diffusion in the streamwise direction. A one dimensional, 1-D flow field with property ϕ transported by advection and diffusion, the steady state governing equation is of the form in:

$$\frac{\partial}{\partial x_j}(\rho u_j \phi) = \frac{\partial}{\partial x_j} \left(\Gamma \frac{\partial \phi}{\partial x_j} \right) \quad (\text{A.3})$$

$$\frac{\partial}{\partial x_j}(\rho u_j) = 0 \quad (\text{A.4})$$

where $j=1$ for One dimensional, 1-D. Equations (A.3) and (A.4) are respectively the transport of ϕ and the continuity equation, where Γ is the diffusion constant. Γ is used for general diffusion problem, it represents dynamic viscosity in N-S equation. Figure A.1 shows a control volume around node Q within a finite volume. The neighbouring nodes are W and E and the control volume faces denoted by w and e .

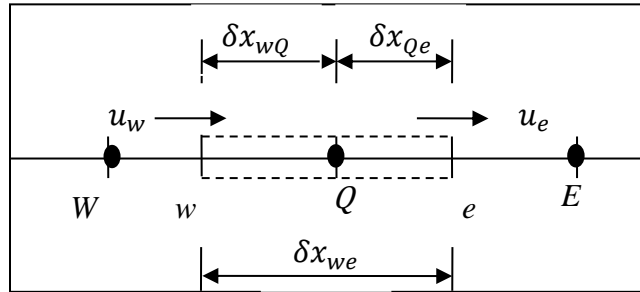


Figure A.1: A control around node Q , adapted from Verstegeeg and Malalasekera (2007)

For the 1-D problem of Figure A.1 integrating the transport equation (A.3) over the control volume and continuity equation (A.4) gives

$$(\rho u A \phi)_e - (\rho u A \phi)_w = \left(\Gamma A \frac{d\phi}{dx} \right)_e - \left(\Gamma A \frac{d\phi}{dx} \right)_w \quad (\text{A.5})$$

$$(\rho u A \phi)_e - (\rho u A \phi)_w = 0 \quad (\text{A.6})$$

where A is the areas of the control volume boundary faces. Discretized equations can be obtained by approximating the terms in equation (A.6) by F and \bar{D} to represent the convective mass flux per unit area and diffusion conductance at cell faces:

$$F = \rho u \text{ and } \bar{D} = \frac{\Gamma}{\delta x} \quad (\text{A.7})$$

Assuming equal areas: $A_w = A_e = A$ Equation (A.6) and (A.7) becomes

$$F_e \phi_e - F_w \phi_w = \bar{D}_e (\phi_E - \phi_Q) - \bar{D}_w (\phi_Q - \phi_W) \quad (\text{A.8})$$

$$F_e - F_w = 0 \quad (\text{A.9})$$

In order to compute the values of F_e and F_w , for simplicity we assume that the velocity field is known. Equation (A.8) can then be solved by calculating the transported property ϕ at the e and w faces. Different schemes can be used to do this, the upwind differencing scheme is discussed in the following section.

A.3.3 Upwind Differencing Scheme

FLUENT allows the user several options of upwind schemes to solve ϕ_w and ϕ_e by using the value of ϕ from the cell upstream. The upwind schemes include First Order Upwind, Second-Order Upwind (SOU), Power Law, and Quadratic Upwind Interpolation for Convective Kinetics (QUICK) etc. SOU differencing was used in this thesis for second order accuracy. As shown in

Figure A.1, the value of ϕ at the cell's centre is stored. The value of ϕ_Q in Figure A.1 is the average value of the two face values of ϕ ; when first order upwind is used, ϕ_Q is set to centre value for the upstream cell, ANSYS, (2011). The SOU method achieves higher order accuracy through a second order Taylor series expansion.

ϕ_E is calculated for the SOU as:

$$\phi_E = \phi_{sc} + \frac{\partial \phi}{\partial x} x + \frac{x^2}{2!} \frac{\partial^2 \phi}{\partial x^2} \quad (\text{A.10})$$

Where ϕ_{sc} and $\partial \phi / \partial x$ is the cell-centred value and its gradient in the upstream cell, respectively. The last term in equation (A.10) is the derivative of the gradient in the upstream cell. x is the displacement vector from the upstream cell centroid to the face centroid. The calculation for gradients is described in the next section ANSYS (2011).

A.3.4 Gradient Calculation in ANSYS FLUENT

ANSYS Fluent uses three methods to compute the gradient of a variable. The three methods are Green-Gauss Cell-Based, Green-Gauss Node-Based and Least Squares Cell-Based (LSCB). The LSCB offers an economic advantage over other methods, most especially on irregular (skewed and distorted) unstructured meshes which are used in this thesis.

The LSCB method assumes the solution to vary linearly across each cell. Figure A.2 shows four connected cells with the individual nodes located at each cell centroid. Assuming that variable ϕ is to be evaluated at point P in the direction \overrightarrow{PQ} , the LSCB computes the difference between ϕ_Q

and ϕ_P and divides the difference by the length between the two nodes ANSYS (2011). The relationship is expressed in equation (A.11)

$$(\nabla\phi_{c0})\Delta r_i = (\phi_{c1} - \phi_{c0}) \quad (\text{A.11})$$

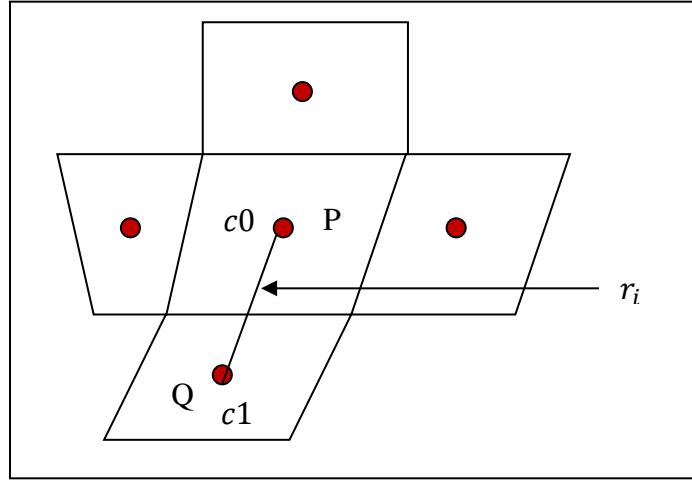


Figure A.2: Evaluation of gradient at the Cell Centroid. Adapted from ANSYS (2011).

where $c0$ and $c1$ are the centroid of the cell of interest and the cell adjacent to it respectively. r_i is the displacement vector. A similar equation can be written for the cell surrounding the cell 0:

$$[J](\nabla\phi_{c0}) = \Delta\phi \quad (\text{A.12})$$

Where $[J]$ is the Jacobian matrix which is purely a function of the geometry, $\Delta\phi$ is the difference vector between node P and Q . The system of linear equations in Equation (A.12) is over-determined and can be solved by decomposing the coefficient matrix using Gram-Schmidt process. Gram-Schmidt process was used because it allows for easy precomputation and storage of weights so that the gradient at each node can be calculated by “looping” over the edges in the

mesh and distributing the contribution of each edge to each of the nodes Anderson and Bonhaus (1994)

A.3.5 Properties of Discretization Schemes

The numerical results can only be accurate or physically realistic when the discretization scheme has certain fundamental properties. The three most important ones discussed in this section, are: conservativeness, boundedness and transportiveness, Versteeg and Malalasekera (2007)

A.3.5.1 Conservativeness

Conservativeness is ensured when conservation of ϕ for the whole solution domain is achieved. This means the flux leaving the control volume (CV) across a certain face is equal to the flux of ϕ entering the adjacent control volume through the same face. This implies that continuity is satisfied. In order to achieve this, the flux through a common face must be represented in a consistent manner by an equivalent expression in the adjacent control volume. Figure A.3 shows a simple case of one dimensional diffusion problem. Q_A and Q_B are the diffusive fluxes entering and leaving a CV made up of four sections. The gradient is computed by central differencing. The overall flux balance may be obtained by summing the net flux through the CV, Versteeg and Malalasekera (2007)

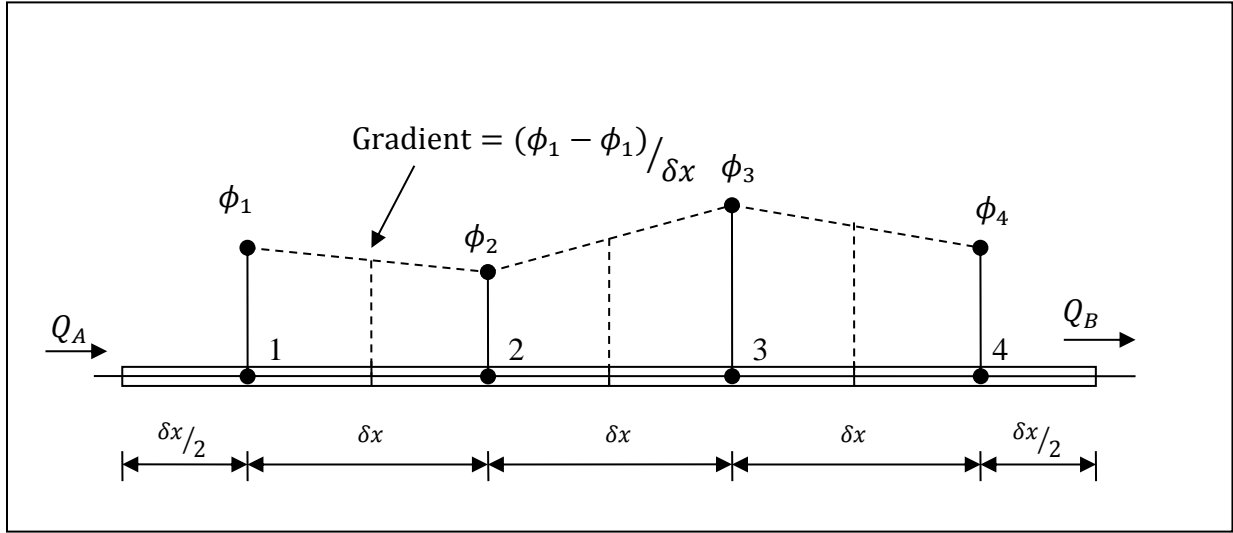


Figure A.3: Discretization of diffusive fluxes Versteeg and Malalasekera (2007).

$$\begin{aligned}
 & \left[\Gamma_{e1} \frac{(\phi_2 - \phi_1)}{\delta x} - Q_A \right] + \left[\Gamma_{e2} \frac{(\phi_3 - \phi_2)}{\delta x} - \Gamma_{w2} \frac{(\phi_2 - \phi_1)}{\delta x} \right] \\
 & + \left[\Gamma_{e3} \frac{(\phi_4 - \phi_3)}{\delta x} - \Gamma_{w3} \frac{(\phi_3 - \phi_2)}{\delta x} \right] + \left[Q_B - \Gamma_{w4} \frac{(\phi_4 - \phi_3)}{\delta x} \right] \\
 & = Q_B - Q_A
 \end{aligned} \tag{A.13}$$

The fluxes across CV faces satisfy: $\Gamma_{e1} = \Gamma_{w2}$, $\Gamma_{e2} = \Gamma_{w3}$, and $\Gamma_{e3} = \Gamma_{w4}$ so that they cancel out in pairs when summed over the entire domain, the conservativeness of ϕ hold in the entire domain. There are other forms of flux interpolation that are not conservative in ϕ , Versteeg and Malalasekera (2007).

A.3.5.2 Boundedness

Boundedness refers to a condition where the internal nodal values of any property should be bounded by its boundary values. This means that the nodal values lie between upper and lower boundary values. This leads to another essential requirement for boundedness which is that all

coefficients of the discretized equation should have the same sign, usually positive. These criteria must be satisfied in order for the solution to be guaranteed of converging. It is related because convergence theorems for most linear equation solvers require diagonal dominance. The boundedness criterion is

$$\frac{\sum |a_{nb}|}{|a'_p|} \begin{cases} \leq 1 \text{ at all nodes} \\ < 1 \text{ at one node at least} \end{cases} \quad (\text{A.14})$$

$$a'_p = a_p - S_p$$

where a'_p the net coefficient of central node P and S_p is the coefficient of the source term. The coefficients are constant for the discretized equation. In order to satisfy diagonal dominance, a'_p should be very large and $S_p < 0$. $\sum |a_{nb}|$ is the sum of all the coefficients of the neighbouring nodes except the diagonal element, Versteeg and Malalasekera (2007).

A.3.5.3 Transportiveness

The transportiveness property of a fluid flow can be illustrated by considering a property ϕ at a point P , and introducing the Peclet number, Pe :-.

$$Pe = F/\bar{D} = \frac{\rho u}{\Gamma/\delta x} \quad (\text{A.15})$$

where Γ is the diffusion constant for property ϕ , $\Gamma/\delta x$ represents the diffusivity at cell faces and the numerator denotes the convective mass flux per unit area. Pe provides an indication of the relative importance of diffusion and convection. Figure A.4 shows the distribution of ϕ in the vicinity of a source at different Peclet numbers. The lines represent contours of constant ϕ , if there is no mass flux the $Pe=0$ form Equation (A.15), this indicates pure diffusion. In the case of

no diffusivity and pure convection, $Pe \rightarrow \infty$ and $\phi_E = \phi_P$ which implies E is influenced only by P . Versteeg and Malalasekera (2007)

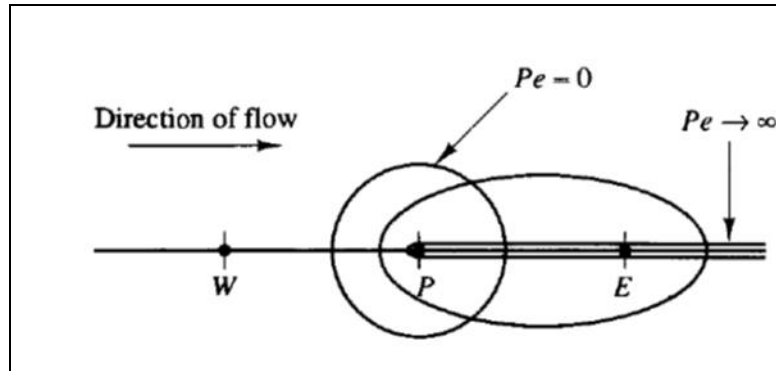


Figure A.4: Distribution of a property in a vicinity of a source at different Peclet numbers from Versteeg and Malalasekera (2007)